Spectroscopic Studies of Arcade Flares with EIS and EVE

Lauren Doyle, B.Sc.(Hons)

Astronomy and Astrophysics Group

SUPA School of Physics and Astronomy

Kelvin Building

University of Glasgow

Glasgow, G12 8QQ

Scotland, U.K.

Presented for the degree of

Master of Science (By Research)

The University of Glasgow

September 2016

This thesis is my own composition except where indicated in the text. No part of this thesis has been submitted elsewhere for any other degree or qualification.

30th September 2016

Abstract

This thesis investigates Doppler velocities in the flares SOL2014-03-29T17:48 and SOL2011-02-16T07:35 through methods of spectral analysis in EUV spectral data from Hinode/EIS and SDO/EVE. This was to understand plasma flows and compare measurements made with both instruments.

Chapter 1 gives detailed background information introducing the Sun and solar atmosphere providing the beginnings to understand the mechanisms behind solar flares. Various spectral lines are also discussed including different properties of the line and appearances in both EIS and EVE data.

In Chapter 2 Hinode/EIS data is introduced discussing the raw data itself, how EIS makes its observations along with spectroscopic analysis carried out. Intensity and Doppler velocity maps are also provided for several emission lines during both flares.

Chapter 3 then discusses EVE data including all of the analysis techniques applied to the raw data and the steps taken to obtain Doppler velocities. Results were then given as velocity-time plots of various emission lines showing the changing Doppler velocity as the flare progresses.

Chapter 4 then brings all of this together and describes the methods used to transform the EIS data into a comparable form to EVE. Direct comparisons of data from both instruments is then made and presented.

Contents

List of Tables

List of Figures

Acknowledgements

Firstly, I would like to extend a massive thank you to my supervisor Professor Lyndsay Fletcher for offering me this Masters project and for her continuous support and guidance throughout. I would also like to thank Dr Hugh Hudson for providing his expertise and knowledge during the course of the year and attending many meetings. I must also thank my parents who without I woud not be submitting this thesis and for their continued help and support. My final thanks goes to everyone in the Astronomy and Astrophyics department for providing advice and support throughout the year.

Chapter 1

Introduction

For centuries the Sun has been observed, studied and even worshiped by many people throughout the ages. It is a constant presence in everyday life, rising in the morning to signify the beginning of the day and setting at night representing the time to rest. Despite this the question still remains: Why should we study the Sun and why is it so important? There are many reasons to answer this question but it depends on what you would consider to be of importance. Firstly, the human race is a very inquisitive species with the first records of the earliest attempts to understand the Sun being made in the sixth century BC (Phillips 1995). Since then vast advances in technology have been made with the Sun now being monitored constantly without any interruptions. Secondly, the Sun has great impacts on the Earth, making it vital to understand the process occurring in the star and how they affect the planet. With this knowledge it is possible to understand other stars in the galaxy, aiding with modeling them and their effects on any orbiting planets. Lastly, as the human race becomes more and more dependent on technology in everyday life, it is important to monitor solar activity and the potential harm it poses to satellites and power grids. With this in mind, space weather caused by solar activity is in fact one of the top eight possible threats to the United Kingdom (UK 2015). These are only three reasons amongst many detailing why studying the Sun is of great importance, however, one of the biggest, and the reason why I enjoy studying the Sun is simply because it is magnificent.

1.1 The Sun

The Sun is a relatively average star in comparison to the billions of others which reside in the universe. However, despite this it is studied in great detail by a vast number of scientists and astronomers, the reason being it is our star and the closest one to us. It is a G2 class star putting it in the middle of the Harvard Spectral Classification with a surface temperature of around 5800 K. It is important to understand the chemical composition of the Sun as it aids in the understanding of the formation, structure and evolution of the Sun and the Solar System. The most abundant element in the Sun is Hydrogen (H) contributing to 71% of the solar mass, which is followed by Helium (He) at 27%. The final 2% is made of heavier metals, compromising of Oxygen (O), Carbon (C) and Nitrogen (N), amongst many others. The Sun formed almost 4.5 billion years ago and is a typical main-sequence star converting hydrogen to helium via the proton-proton chain (Carroll & Ostlie 2006). Figure 1.1 shows the interior and atmospheric structure of the Sun.

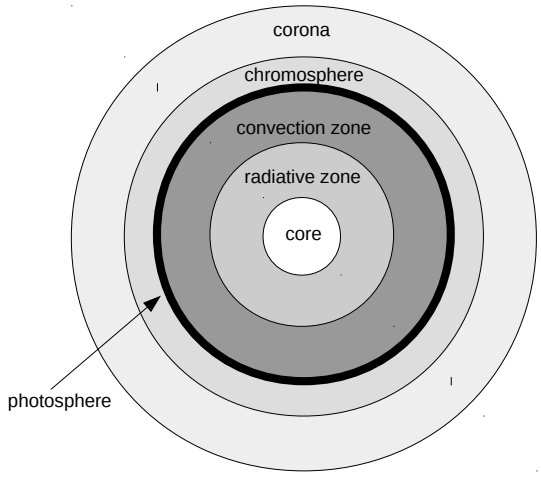

Figure 1.1: A diagram showing the structure of the solar interior and solar atmosphere, this has not been drawn to scale.

The core of the Sun is where thermonuclear reactions take place and is the source of high energy photons and neutrinos (Cox et al. 1991). In fact, the mass fraction of

hydrogen at the center of the Sun has decreased from 0.71 to 0.34, while helium has increased from 0.27 to 0.64. The fusion inside the core generates a temperature of 15 million K and has an incredibly high electron density of 10^{34} cm^{-3} (Carroll & Ostlie 2006).

Above the core is the radiative zone where energy is transported in the form of radiation at a temperature range of 2-7 million K. Once energy has been created inside the core it is transported by photons, interacting with ions and electrons, taking approximately 1 million years to reach the edge. This is because, even though the photons travel at the speed of light they bounce around so many times trapping them within the zone for extremely long periods.

Between the radiative zone and convection zone lies a small interface layer also known as the 'tacholine' which is Greek for 'speed' as it is a region of gradient in rotation speed. It also forms the region where energy transfer transitions from being radiative to convective. It is also a layer posing many questions, as it is believed to central in generating the Sun's magnetic field through a magnetic dynamo (Piddington 1983).

The convection zone is the last layer in the solar interior and extends up to the visible surface. When radiative transport breaks down, convection takes over. It occurs when the gas in the solar interior is displaced and continues to rise upwards to the surface. The most important factors for convection to occur are; (i) there must be a steep temperature gradient and (ii) the adiabatic index of the gas, γ, must be approximately 1. Where the adiabatic index is the ratio of heat capacity at a constant pressure to heat capacity at a constant volume. The temperature drops again to 6,000K along with the plasma density. The convection zone is more turbulent than the radiative zone below it and carries heat rapidly to the surface. The convective motions can be seen on the surface in the form of granulation and it is thought that by twisting up the magnetic field inside the Sun, these motions aid in the phenomena such as solar flares and CME's.

1.1.1 The Solar Atmosphere

There are three different layers to the solar atmosphere; the photosphere, the chromosphere and the corona (Figure 1.2). Each of these have various features and different attributes, however, when studying phenomena on the surface it is impossible to study only one of these layers in isolation. In fact, particular parts of the solar spectrum are absorbed and emitted at different heights in the solar atmosphere and so, it is vital to have an understanding of them all.

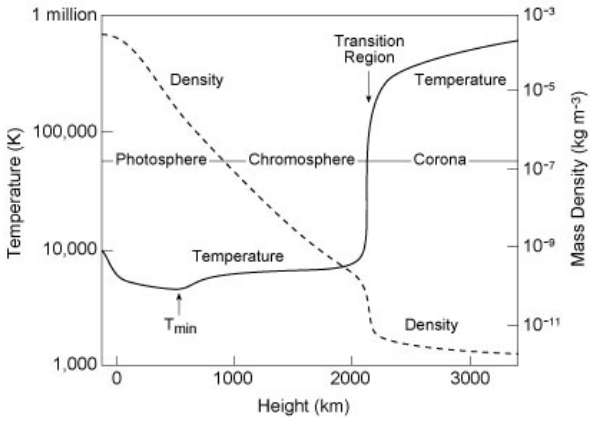

Figure 1.2: This schematic plot shows the changing temperature and density of the solar atmosphere with respect to height from the surface starting at the photosphere, by Eugene Avrett, Smithsonian Astrophysical Observatory.

The photosphere is the effective surface of the Sun as it is defined as the layer where visible light seen at 500 nm is emitted, ie. where the optical depth $\tau_{500} = 1$. It has a temperature range of 4,300K - 6,600K, corresponding to the temperature range of sunspots as they form in the photosphere which, extends to a height of approximately 400km. The magnetic field of the photosphere is strongest at locations containing sunspots (between 1-3kG), however, fields do exist elsewhere and it is likely the whole surface is permeated by a very weak field caused by concentrated strong fields between granules. (Phillips 1995).

The chromosphere is a narrow part of the solar atmosphere with a height of approximately 2500 km. It is an irregular layer where the temperature rises with height

from 5,800K at the photosphere to about 25,000K (Carroll & Ostlie 2006). At these high temperatures hydrogen emits H-alpha (Hα) emission and can be seen as a reddish colour. By using spectrograph filters in Hα many features of the chromosphere can be seen including the highly non-uniform, structure of the region. The main characteristics of the chromosphere include a rise in temperature with height and a complex structure which is always changing (Phillips 1995). When viewing the chromosphere in Hα it is possible to see a phenomena known as supergranulation, which is evident on scales of 30,000km and shows the effects of the underlying convection zone (Figure 1.1). Supergranulation is the cause of a large scale horizontal velocity field, produced in the upper levels of the photosphere. It resembles greatly to ordinary granulation but the spatial and temporal scales are much larger. This velocity field is the cause of a giant system of convective currents and the resulting effects were named supergranulation by Leighton et al. (1962). Observations of granulation show a very clearly defined cellular structure with a narrow distribution of cell sizes (Bray et al. 1984). Another feature present is vertical filaments of gas which extend up from the chromosphere to heights of 10,000km. These are known as spicules and have lifetimes of approximately 15 minutes, however, is is estimated that around 30,000 of these can exist at any given time, covering 2-3 percent of the Sun's surface (Carroll & Ostlie 2006). It is in this layer of the atmosphere that flares radiate most of their energy away.

Above the chromosphere there is a region of one hundred kilometers in thickness which has a rapid increase in temperature (Figure 1.2). It can reach up to 10^6K before the temperature gradient flattens out again, and is known as the transition region. This layer can be observed at various altitudes through the UV and EUV parts of the electromagnetic spectrum due to its very high temperature (Carroll & Ostlie 2006).

During a total solar eclipse (Figure 1.3), the Moon completely obstructs the photosphere, and white-light radiation from the corona is visible. In white-light some features of the corona can be seen, such as streamers, large cap-like coronal structures, and plumes and long thin streamers projecting outwards from the poles (Phillips 1995). The corona extends out to several million kilometers. However, one could say it extends to the edge of the solar system, and has a temperature range of a few million

Kelvin. Due to these high temperatures, hydrogen and most of the other elements become fully ionised. The corona produces X-rays, EUV, radio radiation and much more. Even though emission from the corona is a tiny fraction of the luminosity when compared to that of the photosphere, it covers a far wider wavelength range. The density of the corona is low, typically 10^8 - 10^9 particles cm^{-3} , and so is essentially transparent to most electromagnetic radiation, therefore, making it not in local thermal equilibrium (Carroll & Ostlie 2006). One of the biggest problem or question in solar physics is the high temperature of the corona as it is unknown how energy dissipates in this region to heat the plasma. This is referred to as the coronal heating problem and despite scientists' best efforts, a concrete solution has still not been reached. One of the most striking phenomena associated with the solar corona is the solar wind, a stream of ions and electrons which flow outwards from the Sun. Many observations have been made of the solar wind including during eclipses when the corona can be seen and streams of plasma are observed leaving the poles. The solar wind has an average speed and temperature of 440km/s and 83,000K, traveling across the solar system (Richardson 2010). Once the solar wind reaches Earth it can pose many threats including the disruption of satellites and power grids. However, the Earth's atmosphere and magnetic field protects the planet and its inhabitants from the harmful radiation and charged particles.

1.1.2 Solar Flares

A solar flare is a sudden and localised brightening in the solar atmosphere which is visible across all wavelengths and caused by a rapid reconfiguration of the magnetic field in the solar corona. Flares are an increase in radiation and are almost always accompanied by a mass motion, known as a coronal mass ejection (CME), of fast-moving magnetised plasma out into the corona and heliosphere. Before a solar flare the magnetic field in the corona becomes stressed and twisted, producing magnetic energy in the form of a build up of current. This is converted into kinetic energy, thermal energy and particle acceleration when the magnetic field structure simplifies

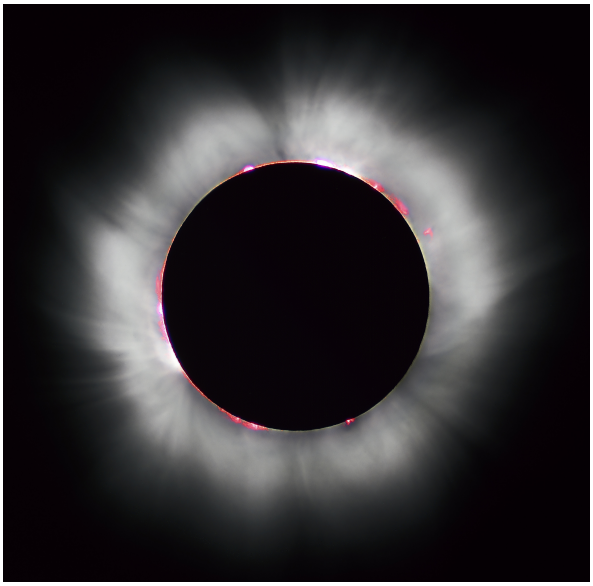

Figure 1.3: An image of a total solar eclipse taken in 1999 by Luc Viatour. This image shows the clear structure of the corona along with some features such as plumes being present. The reddish tinge of the chromopshere can been seen along the edge with a few prominences clearly visible.

through a process described as magnetic reconnection.

Magnetic reconnection is a process by which a magnetic field in an almost ideal plasma changes its topology. An ideal plasma satisfies $E + v \times B = 0$, where v is the velocity, E is the electric field and B is the magnetic field, almost everywhere in the domain under consideration. Imagine the magnetic field twisted and caught. Due to the 'frozen in field' condition, the magnetic field is frozen in the plasma and particles follow the magnetic field with a Lorentz force. If the topology of the magnetic field has to change then the path the particles follow must also change. In the region where magnetic reconnection occurs there is an increase in strength of magnetic field causing the particles to change direction (Figure 1.4). This process results in a relaxed field at a lower energy state, causing energy to be liberated from the system. It is this liberated energy which is responsible for many of the solar phenomena observed on the Sun's surface but also many other events occurring in the solar system.

Something which is of great importance to the work carried out in this thesis is

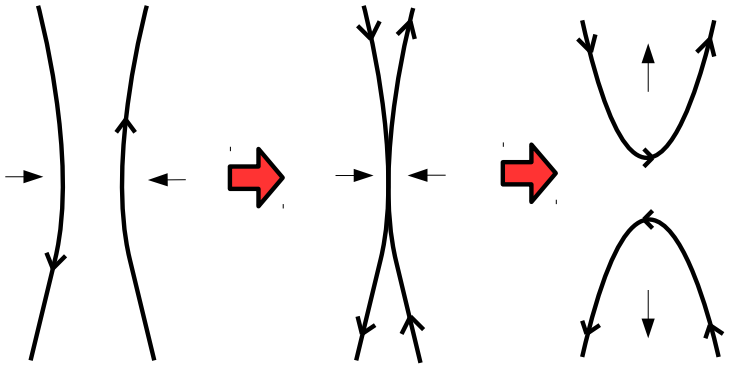

Figure 1.4: A simple schematic diagram showing magnetic reconnection. Two parts of the magnetic field of opposite polarity are forced together causing them to break and snap back to a different configuration.

chromospheric evaporation. When magnetic energy released into the corona by solar flares reaches the chromosphere it drives upflows and downflows known as evaporation and condensation (Longcope 2014). Chromospheric evaporation occurs when material in the chromosphere is heated more quickly than it can cool. This causes the heated material to expand up into the lower corona and downwards into the upper high density chromosphere. These movements of plasma can be seen as blueshifts and redshifts in Doppler velocity calculations and maps. Blueshifts can occur in hot emission lines at temperatures exceeding 10^7 K during the impulsive phase of solar flares. Redshifts can occur when the flare is of X class and chromospheric evaporation is extensive, causing lines formed in the upper chromosphere and transition region to be redshifted (Brosius & Holman 2007). This phenomenon has been studied for over 40 years since it was proposed by Neupert (1968), to explain the delay between peaks of soft X-rays in the gradual phase, and microwave emission in the impulsive phase (Fletcher et al. 2011). Doppler maps in Chapter 2 show blueshifted and redshifted material during flares caused by upflows and downflows as a result of chromospheric evaporation.

There are many physical attributes associated with flares occurring in and around the active region where a flare originates. There are always two or more footpoints

which show where the release is happening and appear as bright patches in the active region. This is because a coronal loop has two ends, one positive and one negative, attaching it to the photosphere. Footpoints are also connected to flare ribbons; usually between 2 and 4 can be observed during an eruptive event. They emit in UV, EUV and visible wavelengths and sometimes even hard X-rays (HXR) occurring at the same time as the release of the flare (Janvier et al. 2016). On observation of flare ribbons they appear after magnetic reconnection has occurred near the footpoints of the flare in the active region forming in the chromosphere. As time progresses the ribbons separate from each other, brightening briefly before dissipating then disappearing. Flares also lead to a brightening in coronal loops around the active region, producing high fluxes of soft X-ray (SXR) emission which cools through EUV temperatures after the main release of the flare energy. Post-flare loops always occur and if the flare is big enough in physical extent then these loops side-by-side produce a post flare arcade.

Large solar flares can be split up into three different stages:

1. **Preflare Phase** - During this stage soft X-ray emission gradually increases and very little hard X-rays or gamma rays are detected above background instrumental level.

2. **Impulsive Phase** - Next, gamma rays and hard X-rays rise impulsively in short intense bursts of emission. These bursts only last between a few to tens of seconds were the soft X-ray flux also rises rapidly.

3. **Gradual Phase** - The last stage results in the rapid decay of the hard X-rays and gamma rays with a time constant of a few minutes. The soft X-rays follow a similar pattern but with a significantly longer decay time of approximately hours.

Flares have been studied for over one hundred years by many people. In 1859 Richard Carrington made the first observation of a solar flare while making drawings of sun spots on the surface. He noticed strong brightenings in the same area as a group of sunspots which we now call a white light flare (Carrington 1859). Following Carrington's observations there were problems with telegraphs, and the aurora was also

observed much further south than usual, marking the first ever space weather event. This paved the way for the study of solar flares, however, you may ask why it is of such importance.

Flares are very powerful, energetic events with the potential to have an energy output exceeding 10^{32} ergs (Fletcher et al. 2011). Scientists are still baffled by the problem of energy conversion during these events. The biggest question flares pose is how can the bulk storage of magnetic energy be converted into thermal and non-thermal particle energies? Putting this question aside there are also practical aspects such as the implications and effects on planets, satellites and Earth itself. Solar flares also provide a link to understanding CME's, exoplanet atmospheres including conditions for life on a planet orbiting an active star, and can lead us to better understanding of stellar physics. All of this aside it still remains that solar flares are extraordinary, beautiful and exciting, providing a great insight into the wonders of the solar system and beyond.

1.2 Spectroscopy

Emission line spectroscopy has been used for decades to observe line profiles of emission lines from solar plasma. Measurements from many satellite missions have been used to calculate line shifts and in turn plasma speeds. Before any data or analysis is looked at it is important to understand the importance and the methods of this well developed technique. Here we will look at the past, present and future of emission line spectroscopy detailing how it has changed throughout the years but also the important discoveries which have been made so far, paving the way for many more to come.

1.2.1 EUV Spectroscopy of Flares Background

Extreme Ultraviolet (EUV) spectroscopy has developed dramatically over the past 50 years or so (Milligan 2015). In the late 1960's and early 1970's, Hall & Hinteregger (1969) and Hall (1971) made the first discoveries of EUV bursts relating to solar flares.

Using data from spectrometers on board rockets and the Orbiting Solar Observatory (OSO) III satellite, they took measurements of solar radiation in the wavelength range 131 to 27nm (Hall & Hinteregger 1970). Since then EUV spectroscopy has taken off, with the first imaging-spectroscopy observation of a flare taking place in 1999 using the Coronal Diagnostic Spectrometer (CDS) on board SOHO (Czaykowska et al. 1999). During these observations Czaykowska & De Pontieu, 1999 determined line-of-sight velocities and their temporal evolution during the gradual phase of an M6.8 flare. They found bright downflowing plasma in regions between ribbons and less bright plasma on the outer side of ribbons showing strong blueshifts. The patterns of upflows and downflows found in EUV wavelengths demonstrated, for the first time, the existence of chromospheric evaporation during the late gradual phase of the flare (Czaykowska et al. 1999). These observations along with many others have begun what is now a very successful field in Solar Physics.

1.2.2 Current Research

Spectroscopy of EUV emission is an extremely useful tool, providing quantitative measurements of many parameters including temperature, density and velocity of plasma in the 10^5 - 10^7 K range. Results obtained from spectroscopy can be compared with theoretical models aiding in the understanding of many solar phenomena (Milligan 2015). Space-based observatories such as the Solar Dynamics Observatory (SDO), Hinode, the Interface Region Imaging Spectrograph (IRIS) and the Solar and Heliospheric Observatory (SOHO), along with many others have been making spectroscopic observations for 20 years. With every new instrument/mission the accuracy and spectral and spatial resolutions have increased. In fact, many of these missions have been so successful that their lifetimes have been extended or re-purposed, often many times in the case of SOHO.

One of the best observed flares in history occurred on 29th March 2014 with a GOES class of X1.0. It was witnessed by many satellites including all instruments on board the Solar Dynamics Observatory (SDO) and Hinode and even ground based

instruments such as the Dunn Solar Telescope (DST) (Milligan 2015). As a result of this, the flare has been looked at extensively by many people including, Li et al. (2015) who used EIS and IRIS data to investigate chromospheric evaporation in flare ribbons by characterising Doppler shifts. The results include evidence of evaporation signatures found at two flare ribbons in the process of separating and dominant blueshifts in the high temperature Fe XXI line. Young et al. (2015) also investigated the SOL2014-03-29T17:48 event with IRIS observations to investigate Fe XXI emission and its movements during the flare. They found blueshifts at the brightest ribbons suggesting upflows into the corona which were present for at least six minutes after the flare peak. This is one of the events which will be studied in this thesis as it provided a wealth of data from many instruments, all with different perspectives on the Sun. It is with observations like this and by combining data sets that great advances, not just in spectroscopy but in solar physics, will be made.

1.2.3 Future Spectroscopy

As mentioned previously, some of the greatest discoveries and revelations will be made using data from coordinated observations, such as this thesis will discuss in detail. However, with so many spectrometers and instruments in space all observing the Sun at the same time you may wonder why there is any need for more. In fact, as technology develops and instruments become more accurate and sensitive there are always opportunities to develop spacecraft to obtain more comprehensive data. Missions such as the Solar Orbiter, due to launch in 2018, will push the boundaries of current technology, putting the space craft in close proximity with Sun at $0.3R\odot$. It will carry 10 different instruments and will address the central question: How does the Sun create and control the heliosphere? As well as this, studies will be made of the solar wind, coronal magnetic field and solar dynamo, with the initial mission to last three years. There are many instruments of interest to spectroscopy including; the Multi Element Telescope for Imaging and Spectroscopy (METIS) which, will perform spectroscopy of the most intense lines of the outer corona, and the Spectrometer/Telescope

for Imaging X-rays (STIX) which, will provide imaging spectroscopy of solar thermal and non-thermal X-ray emission (Müller et al. 2013). This in turn will deliver a very different perspective on what we believe is happening on the surface of our parent star, either agreeing with current models or challenging our understanding. As things develop and technology gets better will more questions of our universe be answered, and more will surely surface.

1.3 Instruments

Throughout this project two main sources of data were used from two very different instruments. These are the Extreme-Ultraviolet Imaging Spectrometer (EIS), on board the Japanese mission Hinode, and the Extreme Ultraviolet Variability Experiment (EVE), a NASA mission on board the Solar Dynamics Observatory.

1.3.1 Extreme-Ultraviolet Imaging Spectrometer (EIS)

The Hinode satellite is a Japanese-US-UK mission, which was launched in September 2006. It consists of three separate instruments; The Solar Optical Telescope (SOT), the X-Ray Telescope (XRT) and the Extreme-Ultraviolet Imaging Spectrometer (EIS). All of these instruments work together studying the same target which the spacecraft is pointed at. Its main purpose is to study the interactions between the Sun's magnetic field and its corona, to increase our understanding of the causes of solar variability and origins of solar activity (Kosugi et al. 2007). In particular, there are three main scientific goals which Hinode hopes to investigate. These include determining the mechanisms responsible for heating the corona in the active region and quiet Sun, establishing mechanisms which cause phenomena such as flares, and investigating processes for energy transfer from the phostosphere to the corona (Culhane et al. 2007). Hinode has a circular, sun-synchronous, polar orbit with an altitude of 680 km and an inclination of 98.1 degrees. This orbit was chosen as it allows continuous observations of the Sun to be made for a duration of nine months each year (Kosugi et al. 2007). For the

purposes of this project only data from the EIS instrument was used from this mission.

EIS is a normal incidence, two-optical-element spectrograph which, observes in two spectral bands, 170-210Å and 250-290Å (Korendyke et al. 2006). There are four slit widths available for EIS: 1″ slit, 2″ slit, 40″ slot and 266″ slot (Kosugi et al. 2007). Slit rasters of selected sections of the solar surface are obtained by mechanically tilting the primary mirror (Korendyke et al. 2006). These rasters only cover small areas of the solar disk and the positions at which EIS will observe are also chosen well in advance, making it difficult to make sure all important events are recorded. EIS has a resolving power of R = 4000 which roughly equates to a spectral resolution of 3.3 pm at a wavelength of 132.9Å (Kosugi et al. 2007). EIS has a significant contribution to the scientific aims of the Hinode mission. This involves the measurements of line intensities, Doppler velocities, line widths, temperatures and densities for plasma in the Sun's atmosphere. The spectral and spatial resolution has been enhanced through many design features, making EIS greater than any other spectrometer operating in similar wavelengths, including EVE (Culhane et al. 2007). The results of the enhanced spectral and spatial resolution can be seen in Chapter 2 through the great detail provided in the EIS rasters.

1.3.2 Extreme Ultraviolet Variability Experiment (EVE)

The Solar Dynamics Observatory (SDO) was launched in February 2010 to kick start the NASA 'Living with a Star' program. This program is a series of missions with the purpose of understanding the Sun's variability, how the Earth and Solar System respond to this and in turn how this affects humanity in space and on Earth (Woods et al. 2012). SDO consists of three separate instruments; the Atmospheric Imaging Assembly (AIA), the Helioseismic and Magnetic Imager (HMI), and the Extreme-Ultraviolet Variability Experiment (EVE). The Solar Dynamics Observatory is positioned in a circular geosynchronous orbit at an altitude of 35,789 km, at 102 degrees West longitude and inclined at 28 degrees (Pesnell et al. 2012). The EVE instrument measures the 'Sun as a Star' as all of the EUV measurements taken by the instrument have no spatial resolution, meaning it is not known where the emission originates from on the

solar disk. This differs greatly from the observation technique used by EIS as the latter only views small sections of the Sun's disk at any given time. For the purposes of this project data from the EVE and AIA instruments were used from the SDO mission. However, EVE was used along with EIS as the main focus. The AIA images were used as a tool to identify what on the disk EIS was pointing at, ie. was the line emission caused by footpoint, ribbons etc, and also how much of the active region was in the EIS field of view. Evidence of this can be found in Section 2.7 in Chapter 2 were comparisons of EIS rasters and AIA images are made.

EVE (Woods et al. 2012) has four scientific objectives which it carries out through Extreme Ultraviolet (EUV) measurements, in conjunction with modelling activities and data gathered from other SDO instruments. These objectives are as follows (Turck-Chièze et al. 2006):

1. Specify the solar EUV irradiance and its variability on multiple time scales from seconds to years.

2. Advance current understanding of how and why the solar EUV spectral irradiance varies.

3. Improve the capability to predict (both nowcast and forecast) the EUV spectral variability.

4. Understand the response of the geospace environment to variations in the solar EUV spectral irradiance and the impact on human endeavours.

EVE measures the Sun's brightness (irradiance) in the EUV part of the spectrum, this ranges in wavelength from 1Å to 1050Å. The high-spectral-resolution irradiance measurements are taken by the Multiple EUV Grating Spectrographs (MEGS) (Woods et al. 2012). MEGS is composed of two spectrographs, MEGS-A and MEGS-B, covering wavelength ranges of 50 to 370Å and 350 to 1050Å, respectively. The full spectral range is measured every ten seconds continuously with a spectral resolution of 1 Å (Woods et al. 2012). However, on May 26th 2014 MEGS-A stopped taking data due to a power

failure and so, has been out of commission since then. Despite this setback, MEGS-B is used to fill the gaps as best as it can and this does not affect any data that will be used throughout this project as it was taken before May 26th 2014.

1.4 Spectral Lines Used

The selection of spectral lines was an important task with many factors to consider. The aim of the project was to make comparisons of Doppler velocities from EVE and EIS data. Two flares were selected SOL2011-02-16T07:35 and SOL2014-03-29T17:48, as both instruments had taken observations of the events. It was also decided that spectral lines would be selected with the aim of having one cool, one coronal and one hot line to cover a wide range of formation temperatures and hence, different aspects of the flare. Many emission lines were investigated throughout the research project, most of which were selected through the review of previous spectroscopy work. Milligan & Dennis (2009) and Young et al. (2007) both give specific details on many lines that can be observed using EIS, while Zanna & Woods (2013) give detailed information on EVE emission lines. It is through these papers, plus trial and error, that particular lines were chosen for comparisons to be made. The chosen emission lines had to be prominent and isolated to allow fits to the line profiles to be made. The majority of the EVE wavelengths differ greatly from the corresponding EIS lines. This is because EIS only observes pre-selected wavelengths whereas EVE measures all across a broad range. Even though the wavelengths differ, the ions and formation temperatures remain the same and great care was taken to make it clear what each wavelength is.

1.4.1 He II

The He II EVE line has a wavelength of 303.783Å and a peak formation temperature of 80,000 K. It is a relatively isolated line in the EVE spectrum and produces a relatively strong light curve during a flaring event. However, it still contains a large amount of blending including a self blend and possible blends with O III, as well as a blend with

a Si XI line in the blue. However, these cannot be seen in EVE due to the low spectral resolution when compared to EIS.

He II 256.317Å is a badly blended line in EIS spectra containing a blend of itself at 256.318Å and other lines including Fe XIII 256.4Å, FeXII 256.41Å and Zn XX, Si X and Fe X lines. This is described in Young et al. (2007) where it states the blends contained in He II λ256.317 include several iron lines and a silicon line. The He II 256 line is a core line of EIS (it will appear in every EIS study), because it is the coolest line observable by EIS and the strongest below 10^6 K (Young et al. 2007).

1.4.2 O VI

O VI 184.11Å was explored as an alternative to the complex He II as it was measured in the EIS studies of the SOL2011-02-16T07:35 event, one of the two flares investigated here. It is another cool line with a temperature of around 0.3 MK and lies very close to another oxygen line at 183.94Å. EIS rasters were obtained for this line throughout the flare and can be seen in Section 2.4.1.1.

Many O VI lines were investigated in the EVE data to be compared to the corresponding EIS line. However, this proved to be a difficult task as the 184.11Å line was very noisy and had line profiles containing a great number of blends. It was then decided to investigate an O VI line from the MEGS-B spectrometer with a wavelength of 1032 Å. The results of this can be seen in Section 3.7.3.1.

1.4.3 Fe XII

There are two Fe XII lines available for both flares in EIS. These are; 186.85Å for the SOL2014-03-29T17:48 event and 195.12Å fot the SOL2011-02-16T07:35 event. Fe XII 195.12Å lies at the peak of the EIS sensitivity curve meaning it is the strongest emission line observed by EIS in most conditions and because of this it was chosen as one of the EIS core lines (Young et al. 2007). The other Fe XII line at a wavelength of 186.85Å was the better of the two available for the 2014 flare as it contained the least amount of blends and was the least noisy.

Finding a corresponding EVE line proved to be slightly more challenging. Fe XII has a peak formation temperature of 1.5 million K The Sun emits strongly at this temperature across the whole disk, therefore making it difficult to pin point the flare in EVE spectra. In such extreme cases when no apparent flare can be seen in the light curve, lines of slightly different temperatures must be looked at as an alternative, as they might show detectable flare variations.

1.4.4 Fe XVII

In the SOL2014-03-29T17:48 event, EIS took measurements of an Fe XVII line with a wavelength of 254.87Å. This line has a peak formation temperature of 4 million K. It is the strongest of all the Fe XVII lines and other Fe XVII lines can be found at X-ray wavelengths, although there are some weaker transitions in the long wavelength band (Young et al. 2007). This line does not suffer from any blending problems meaning it is a good candidate for Gaussian fitting.

In EVE spectra there is a corresponding Fe XVII line with a wavelength of 98.25Å, however, its light curve proves to be rather noisy. This is due to the lack of clearly resolved Fe XVII lines in EVE spectra causing difficulties fitting the intensity of this line (Del Zanna & Woods 2013). As a result, the Fe XVIII line was used as a comparison to the EIS Fe XVII line. This line has a wavelength of 93.9322Å and a peak temperature of 6 $\times 10^6$K, close to the Fe XVII temperature. It is also a very isolated line and its light curve is not too noisy. More information on this comparison can be see in Chapters 3 and 4.

1.4.5 Fe XXIII

Fe XXIII 263.76Å is a line formed at very high temperatures with a peak formation temperature of around 15 million K, meaning it is only visible during flares and so, is often commonly referred to as a flare line. This particular wavelength was measured in EIS rasters of both the SOL2014-03-29T17:48 and SOL2011-02-16T07:35 events. The Fe XXIII 263.76Å line is predicted to be the strongest line during flares, after Fe XXIV

lines, and is completely unblended (Young et al. 2007).

A comparison line of the strong EIS Fe XXIII line is the EVE Fe XXIII line at 132.9Å. This is also a very strong emission line in the EVE spectra, which is particularly prominent in flares, making it a very good line for analysing Doppler velocities. However, this line contains a strong blend with a Fe XX line at a wavelength of 132.84Å, the strongest of the Fe XX lines, and has a significant contribution during the gradual phase decline of the flare (Del Zanna & Woods 2013). Despite this it does not affect the Gaussian fitting and calculations of Doppler velocities of the flare, because during the impulsive phase Fe XXIII dominates dimming towards the end of the gradual phase when Fe XX becomes more dominant (Section 3.4 and Figure 3.4). Evidence of this can be seen in Figure 3.4 where this blend is discussed in greater detail. All of the work carried out using this line can be seen in Section 3.

Chapter 2

EIS Data

2.1 Introduction

One of the biggest challenges faced during this project was finding data for flares where EIS had observed the active region. This was of particular difficulty with regards to the EIS data due to the nature of its observations, as it only views a small portion of the Sun. A team of Scientific Schedule Coordinators (SSC) meets every three months to decide and plan out the types of observations EIS will make and what measurements will be taken, with reviews occurring on a monthly basis. It is then the responsibility of the EIS team to develop the daily observing plan using the guidance supplied by the SSCs. The SSCs are also responsible for dealing with scientific requests for observations. The simple fact also remains that the Sun is unpredictable and if a particular active region is not being observed then events can be missed by the EIS instrument. From the view point of EVE, strong flares are needed to achieve a signal suitable for spectral line fitting, especially in the lower temperature lines. Bearing all of this in mind it is no wonder that it is difficult to observe flares with EIS and EVE together. However, despite this, one particular event was captured by many instruments and labeled as one of the best observed flares in history. This was an X1.0 class flare which occurred on the 29th March 2014 and was witnessed by SDO, Hinode, RHESSI and IRIS (Milligan 2015).

The event SOL2014-03-29T17:48 occurred in the NOAA active region 12017 at a heliographic position of N11W32 (Aschwanden 2015). EIS took measurements of this active region for many hours, however, only data between 17:41:46 and 17:55:09 were used during the analysis. A second flare captured by EIS and EVE together was on the SOL2011-02-16T07:35 event, which occurred in the NOAA active region 11161 at a heliographic location of N11E45. This flare happened during a point of high solar activity from a group of active regions after an X class flare occurred on the previous day. This chapter details all of the work carried out with the EIS data from both of these events including, the steps taken to analyse and extract the necessary information and all intensity and velocity maps obtained as a result.

2.2 Raw Data

EIS data was downloaded from the ESA Hinode Archive online (`http://www.sdc.uio.no/search/form`), which was very efficient and easy to use providing thumbnails of Doppler velocity and intensity rasters along with detailed images of the slit width used and area of disk covered. This made it much easier to identify which rasters would be useful and which ones actually observed any of the flare. The data was downloaded as a flexible image transport system (FITS) file. Peter Young of George Mason University and a part of the Hinode/EIS team has written many programs for the manipulation of EIS data in IDL that are available to the public to use. These programs, plus some self-written ones were used in the spectral analysis of the EIS data.

The first step to accessing the data is to split the Level 0 data file downloaded from the archive into the Level 1 data file containing the spectral information and the corresponding error file. This is done through the use of the IDL program eis_prep which converts the measured CCD signal into a calibrated intensity and flags bad data points unusable for scientific purposes. These bad pixels can arise from a number of reason such as pixel saturation, cosmic ray hits and possibly defective pixels on the CCD. Bad pixels are referred to as 'missing pixels' and are assigned a value of -100 in

the error file. In the intensity file they are replaced with the median of the neighbouring pixels. However, the main job of eis_prep is to convert the FITS file intensities from 'digital numbers' (DN), pixel values not yet calibrated to physical units, to calibrated intensities with associated 1σ errors (Young 2010). The next step is to select the emission line for analysis and this is done by selecting a fitting window, by using the program eis_getwindata. On execution this command will generate a list of emission lines which were observed by EIS during the raster. From this list a line is selected for investigation and all of the relevant information such as time, intensity and wavelength, will be placed into one structure.

2.3 Gaussian Fitting

EIS data is very different from EVE data in that EVE produces a spectrum from the entire disk of the Sun, while EIS is a slit rastering spectrometer. This means that EIS rasters across a select small area of the Sun's disk using a slit moving from right to left taking spectra at each raster position. Every pixel of the EIS raster contains individual line profiles of the selected emission line within a larger wavelength window. An example of one of these windows and line profiles for one pixel can be seen in Figure 2.1.

Now all of the raw data has been accessed and calibrated it is possible to begin Gaussian fitting in order to calculate centroid wavelengths of the data. This is achieved using another pre-written program called eis_auto_fit. This program requires the structure of the previous program eis_getwindata as an input. From this a Gaussian curve and background can be fitted to the emission line of the selected ion in every pixel of the EIS raster. Once completed eis_auto_fit returns a structure containing properties including; the Gaussian fit parameters and associated error values, the intensity of emission line corresponding to the peak of the Gaussian fit, date of observation, amongst many more.

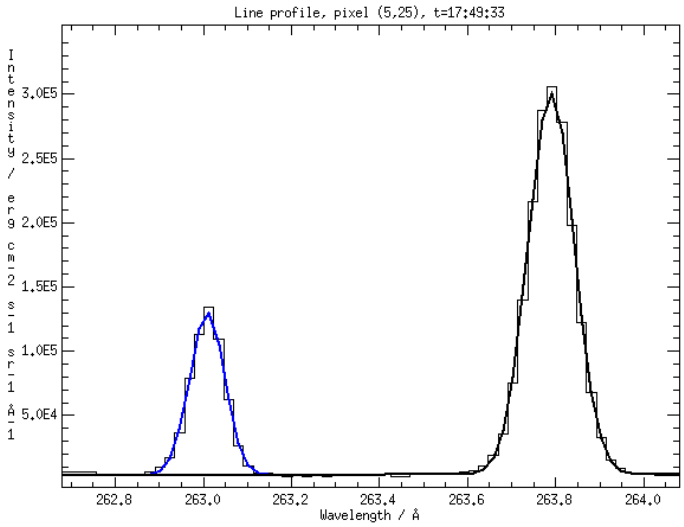

Figure 2.1: A screenshot showing the line profiles of the Fe XXIII wavelength window as seen in the fit viewer window. Two emission lines can be seen at wavelengths of 262.97 Å and 263.76 Å representing Fe XVI and Fe XXIII, respectively. The histogram represents the data ans the solid lines are the Gaussian fits.

2.4 Intensity maps

Now the Gaussian curves have been fitted to every pixel it is possible to obtain intensity maps of the selected ion showing the area of the Sun's disk which EIS has rastered. The peak intensity of the Gaussian fit represents the intensity of the ion's emission in a particular pixel; this can then be mapped out showing a section of the flaring region. These intensity maps can then be compared to AIA images of the same area at the same time, giving a fuller picture of where EIS is observing and how much of the flaring region it is capturing. Examples of this can be seen in Section 2.7.

2.4.1 SOL2011-02-16T07:35

The rasters taken for the SOL2011-02-16T07:35 event have a field-of-view (FOV) of 180 $\times$ 160 arcsec^2 and a slit width of 2 arcseconds. The slit takes steps every 5 arcseconds in the x-direction making a total of 36 measurements in every raster. The data in every measurement is then spread across 5 arcseconds in x to make a complete picture of the

region in the FOV. This process takes approximately 5 minutes and 49 seconds meaning the slit spends around 9.69 seconds at every x position gathering EUV spectral data. Figure 2.2 shows the GOES lightcurve of the flare and the times when the EIS rasters were taken, detailing how much of the flare was observed.

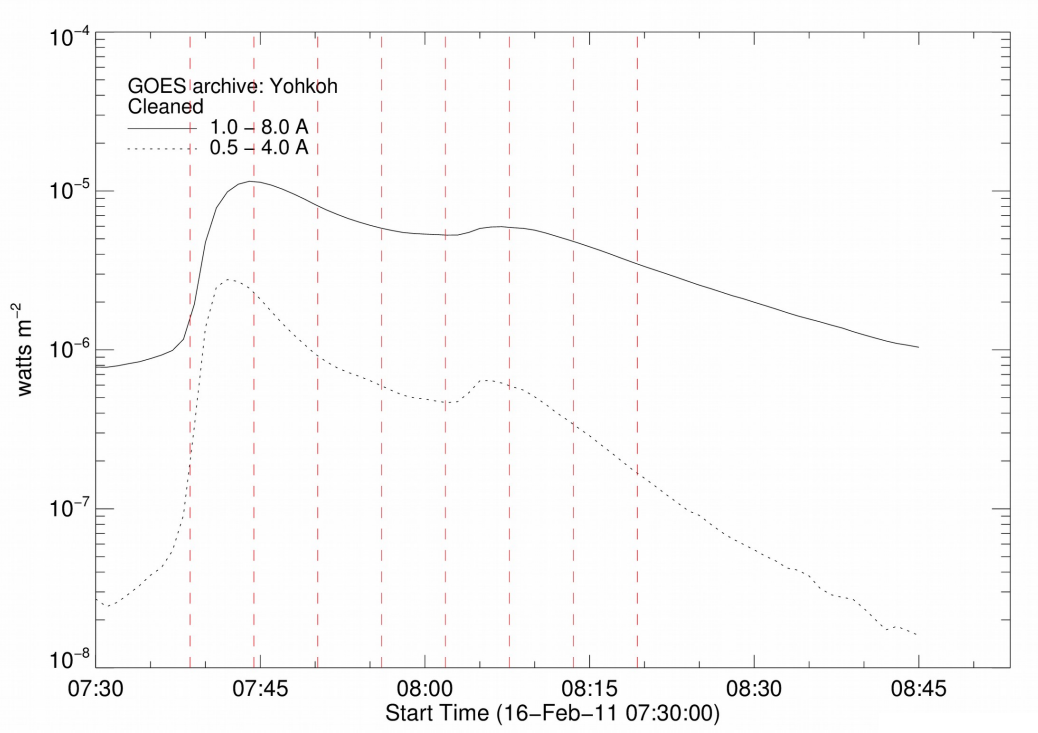

Figure 2.2: The GOES light curve of the SOL2011-02-16T07:35 event and the EIS raster start times overplotted as dashed red vertical lines.

2.4.1.1 O VI 184.117Å

This particular O VI line had an EIS wavelength window of 183.96Å to 184.29Å. O VI 184.117Å is joined by various other emission lines including another O VI line at 183.9372Å, Ni XXII 184.213Å and Fe XXII 184.2988Å. Parts of these other lines appear in the same wavelength window, however, not enough of their line profile is visible to allow for a multiple Gaussian fit. Instead, these lines are removed from consideration by eis_auto_fit by using wvl_select. This process allows the isolation of the OVI 184.117Å

line meaning a single Gaussian can be fitted to the line profile. An example of the line profile can be seen in Figure 2.3.

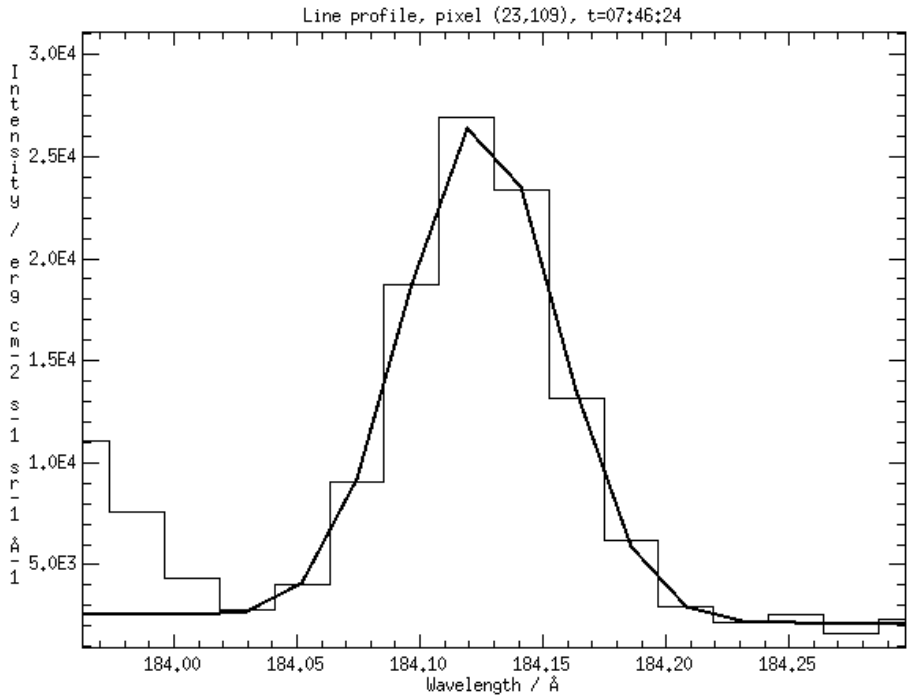

Figure 2.3: A screenshot showing the line profile and Gaussian fitting of the O VI line in one pixel. Another small section of the other O VI line can be seen at a wavelength of 183.93Å which, was removed from consideration by wvl_select.

This was repeated for all EIS rasters covering the SOL2011-02-16T07:35 event and intensity maps were produced. The intensity maps represent the peak of the line profile as determined by the Gaussian fit, and can be seen in Figure 2.4. The intensity maps show O VI reaching a peak intensity at 07:50:14 and again at 08:07:42. Ribbon-like structures can also be seen in all rasters but particularly in the 07:50:14 raster. This is the most prominent and long lived feature in all of the O VI rasters and is caused by a group of a few coronal loops (Section 2.7). The changing intensity of the coronal loops is in relation to the movement of plasma flow from the footpoints and through the loops. The emission is also sparsely and randomly placed next to the loop in the raster suggesting there is also emission originating around footpoints. The white pixels in the

raster represent bad Gaussian fits made by eis_auto_fit to very little O VI emission.

2.4.1.2 Fe XII 195.119Å

Fe XII 195.119Å is the strongest emission line in the EIS range as it is at the peak of the sensitivity curve for the instrument. It provides a very clear and strong emission line which contains only one self-blend but no surrounding lines are present in the wavelength window. A self-blend is when a particular emission line is blended with another line from the same ion but at a different wavelength in extremely close proximity to the original line so that it is not distinguishable. In the case of this Fe XII line it has a self blend with another Fe XII line at 195.179Å, only 0.06Å separating each line. Only a single Gaussian was fitted to the line and the wavelength window had a range of 194.86 Å to 195.37 Å. Gaussian fits can be made to the line profile for Fe XII very easily, and the corresponding line intensity maps can be seen below in Figure 2.5. By observing the intensity maps many features can be seen in the active region. Fe XII is strong at certain points in the first raster before decreasing dramatically during the peak of the flare at 07:44:25. It then increases again at 07:50:14 before dimming very gradually. In comparison to the O VI rasters, Fe XII gives a more detailed insight into the structure of the area observed by EIS. The main noticeable feature is yet again the coronal loop in the center of the raster, which sees an increase in brightness before the flare. Other loops and possible flare ribbons can also be seen in later in later rasters as the active region relaxes.

2.4.1.3 Fe XXIII 263.76Å

The EIS wavelength window for this Fe XXIII line has a range of 263.25Å to 264.12Å and only contains the Fe XXIII line at 263.76Å. Therefore, for this case a single Gaussian was used to fit to the line profile of the emission line which proved to be fairly straightforward. The intensity maps of the emission lines can be seen in Figure 2.6. The intensity maps for Fe XXIII show a very concentrated source of emission beginning as a point and spreading out as the flare progresses. Fe XXIII emission is particularly

strong in rasters 07:44:25 and 08:01:52 as these are the peak times of the flare. By 08:19:21 all evidence of Fe XXIII emission has disappeared with small traces being picked up in individual pixels. As previously mentioned the area observed by EIS is dominated by a few coronal loops causing the majority of the emission seen in O VI, Fe XII and Fe XXIII. In this case the only source of Fe XXIII emission originates from one or possibly two coronal loops as seen in AIA images (Section 2.7). As the flare progresses the emission spreads on the raster showing what is believed to be two distinct coronal loops.

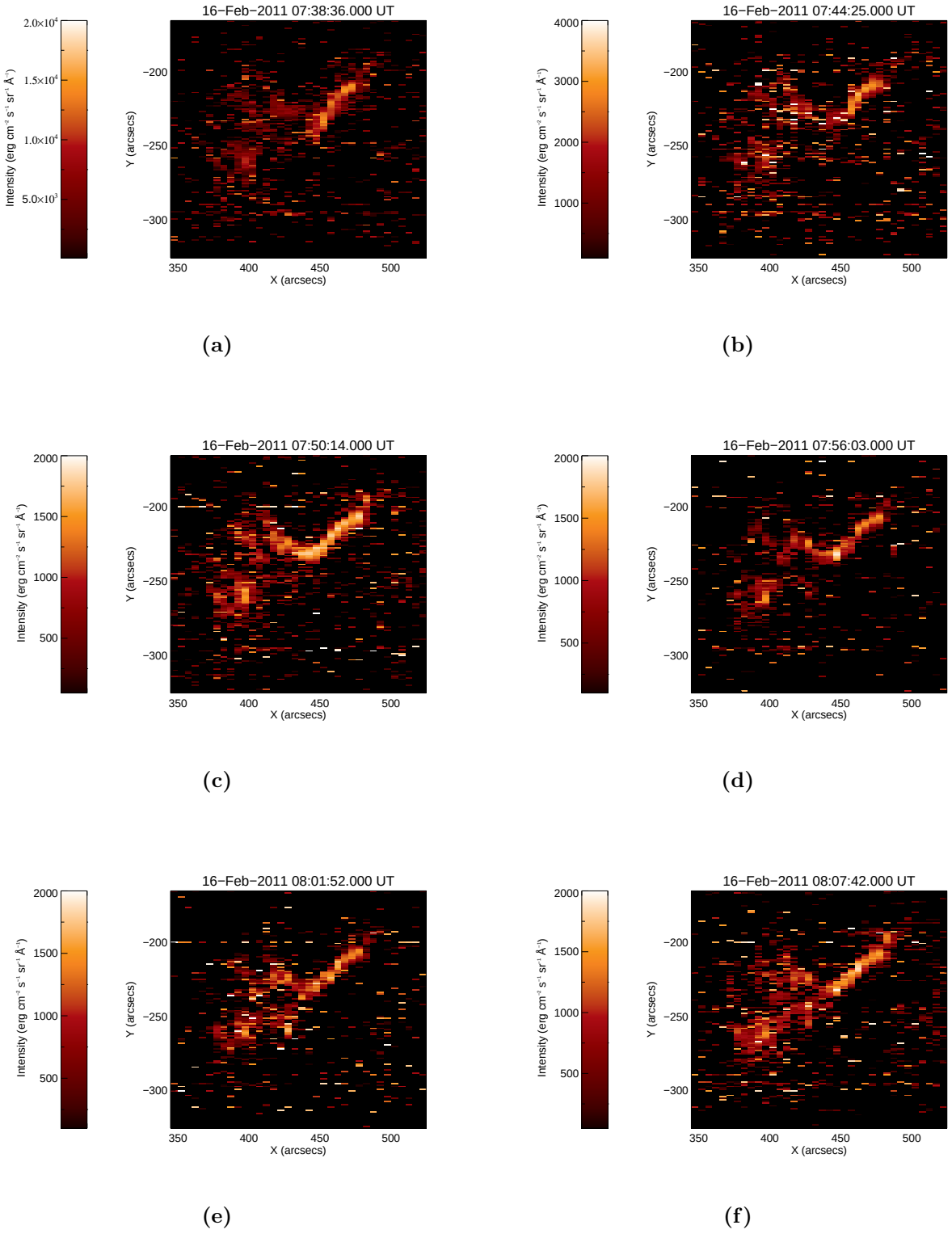

Figure 2.4: Intensity Maps (a) - (h) show the changing intensity of O VI 184.119Å at the observed active region during the SOL2011-02-16T07:35 event, as seen by EIS with respect to time.

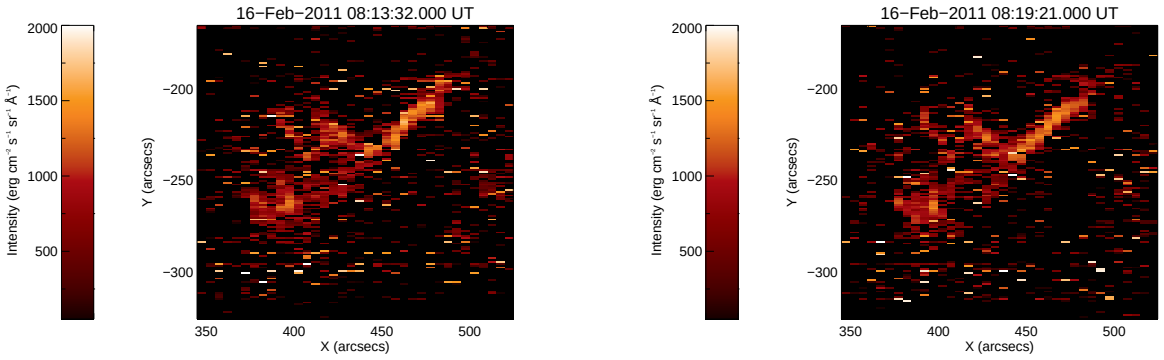

(g) **(h)**

Figure 2.4: Cont. Intensity Maps (a) - (h) show the changing intensity of O VI 184.119Å at the observed active region during the SOL2011-02-16T07:35 event, as seen by EIS with respect to time.

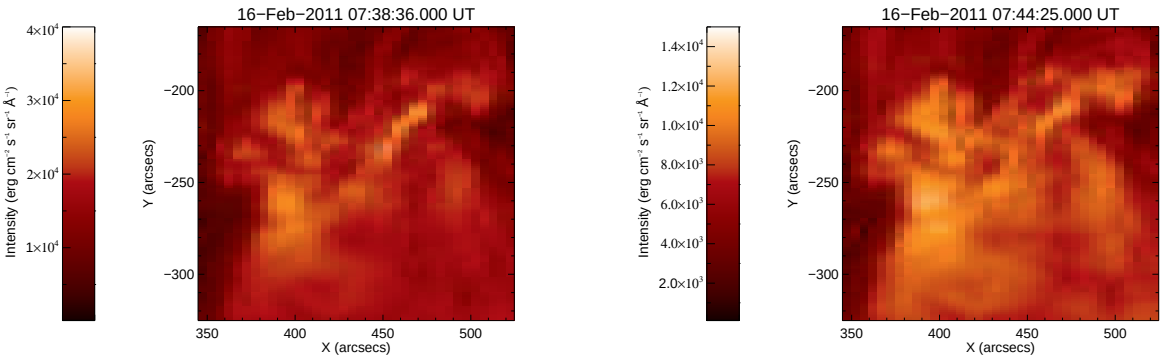

(a) **(b)**

Figure 2.5: Intensity Maps (a) - (h) show the changing intensity of Fe XII 195.119Å at the observed active region during the SOL2011-02-16T07:35 event, as seen by EIS with respect to time.

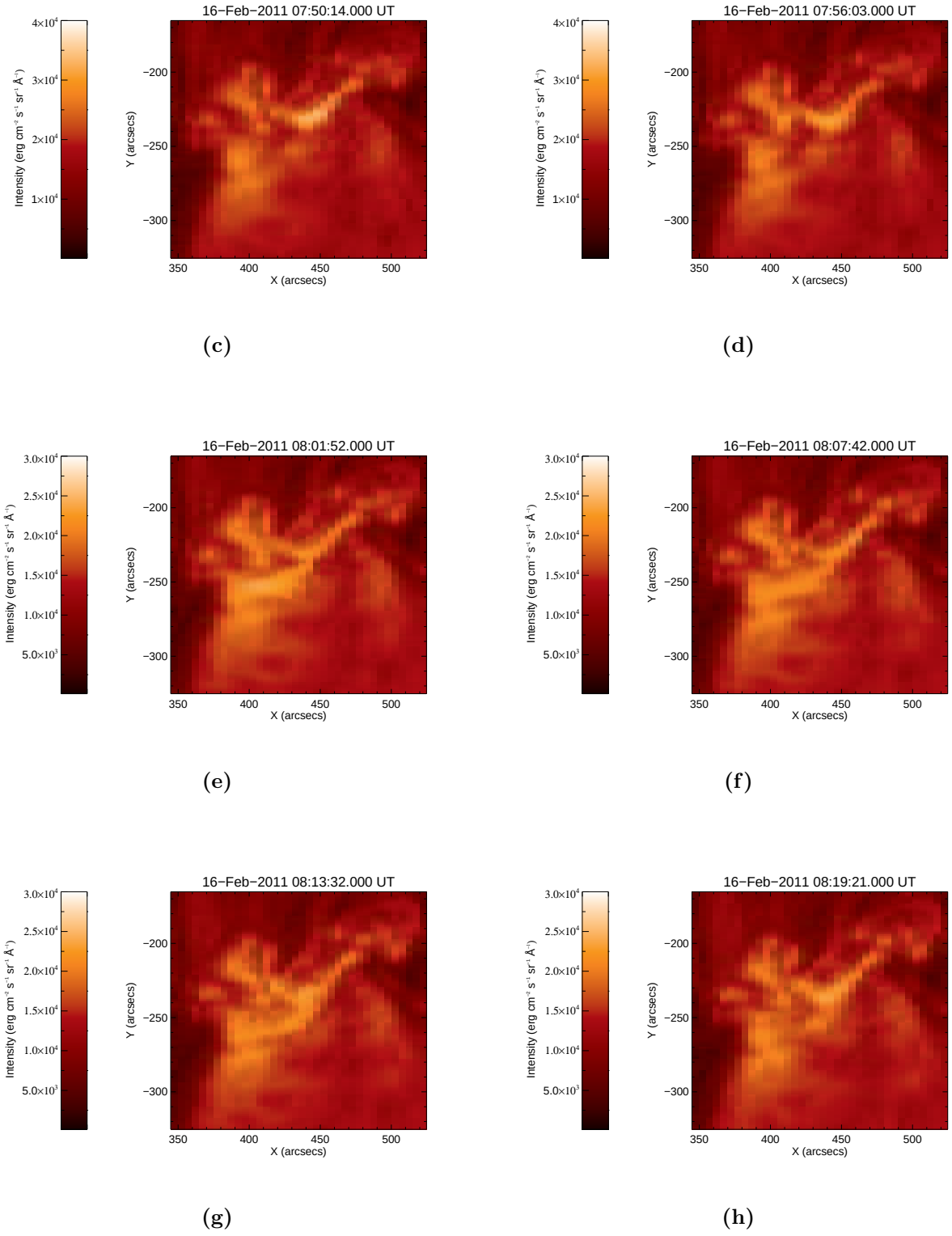

Figure 2.5: Cont. Intensity Maps (a) - (h) show the changing intensity of Fe XII 195.119Å at the observed active region during the SOL2011-02-16T07:35 event, as seen by EIS with respect to time.

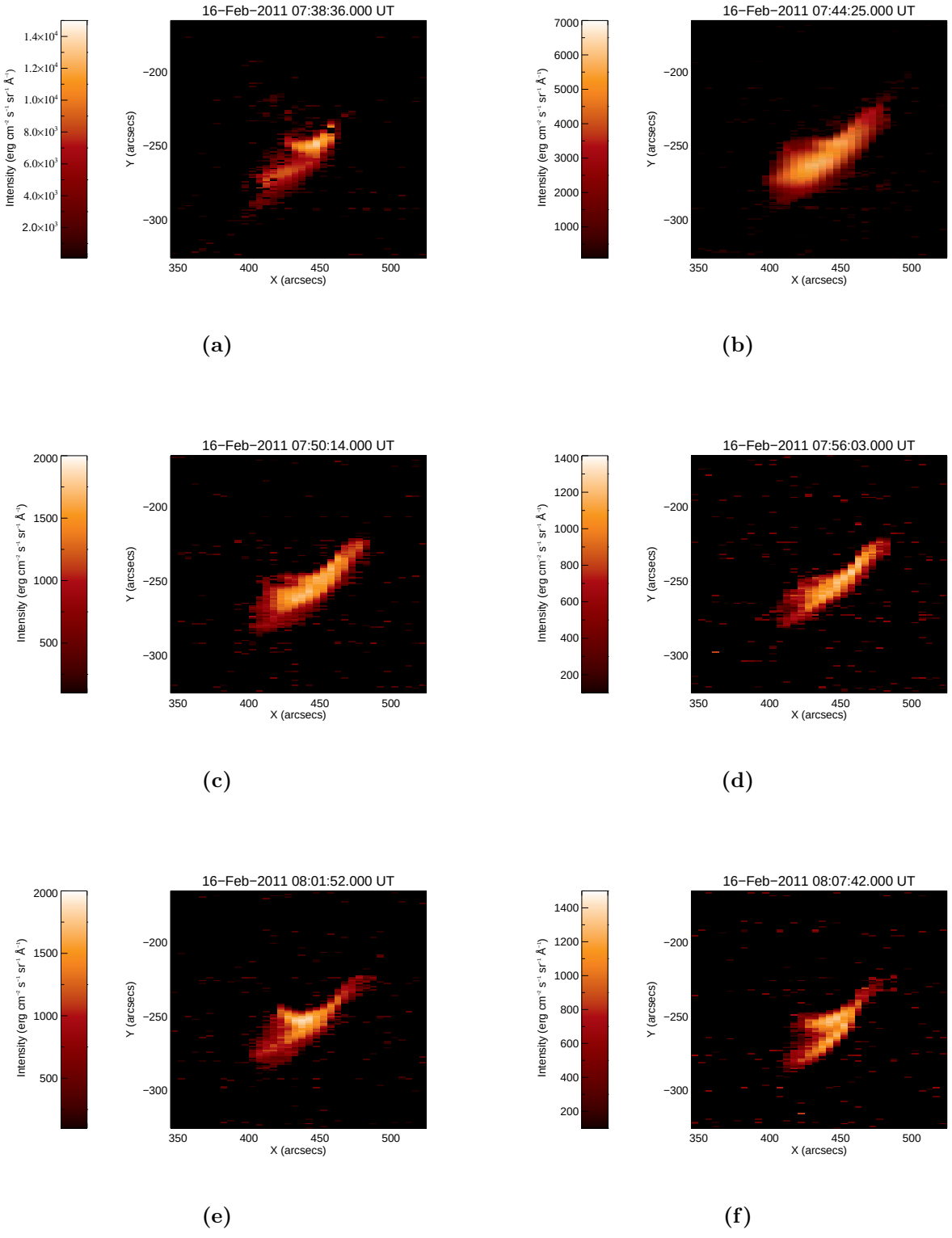

Figure 2.6: Intensity Maps (a) - (h) show the changing intensity of Fe XXIII 263.76Å at the observed active region during the SOL2011-02-16T07:35 event, as seen by EIS with respect to time.

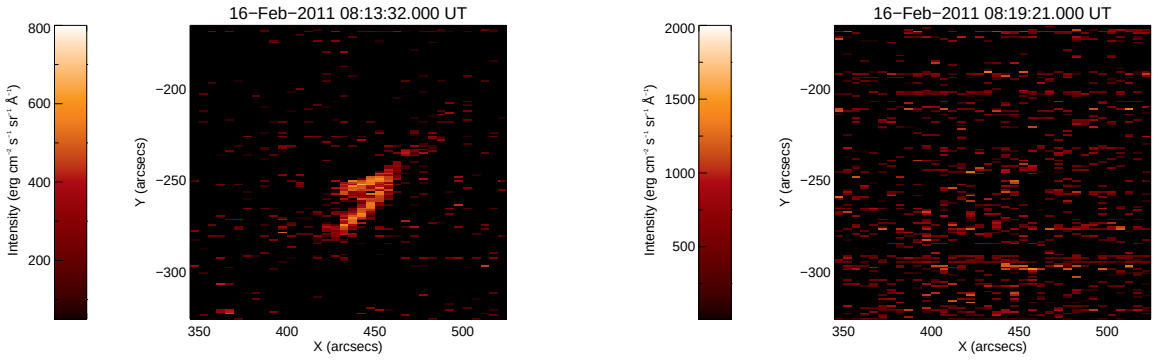

(g) **(h)**

Figure 2.6: Cont. Intensity Maps (a) - (h) show the changing intensity of Fe XXIII 263.76Å at the observed active region during the SOL2011-02-16T07:35 event, as seen by EIS with respect to time.

2.4.2 SOL2014-03-29T17:48

The rasters taken for the SOL2014-03-29T17:48 event have a field-of-view (FOV) of 120 $\times$ 44 arcsec^2 and a slit width of 2 arcseconds. The slit takes steps every 4 arcseconds in the x-direction making a total of 11 measurements in every raster. The data in every measurement is then spread across 4 arcseconds in x to make a complete picture of the region in the FOV. This process takes approximately 2 minutes and 14 seconds meaning the slit spends around 12.18 seconds at every x position gathering EUV spectral data. This is calculated by taking the total observing time of 2 minutes and 14 seconds (134 seconds) and dividing it by the number of slit positions in the x direction which, is 11 in this case. Figure 2.7 shows the GOES lightcurve of the flare and the times when the EIS rasters were taken, detailing how much of the flare was observed.

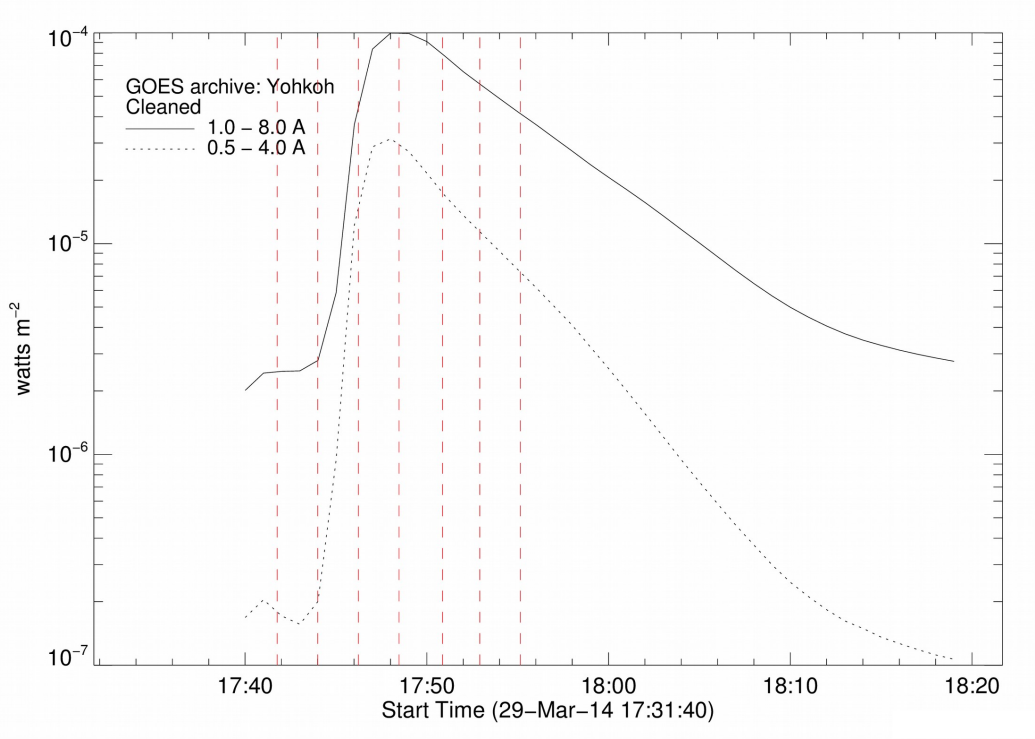

Figure 2.7: The GOES light curve of the SOL2014-03-29T17:48 event and the EIS raster start times overplotted as dashed red vertical lines.

2.4.2.1 Fe XII 186.85Å

For the SOL2014-03-29T17:48 event there were two Fe XII lines observed and recorded using the EIS spectrometer. These had wavelengths of 186.85Å and 192.39Å. The 186.85Å line was chosen because it contained the least blending and other lines present in the wavelength window. The 192.39Å line lies amongst many other lines including two Fe XI lines and three O V lines. This meant it was very difficult to fit the Gaussian to the Fe XII lines. Even though multiple Gaussians can be used it was still unreliable at fitting to the Fe XXII line due to the degree of blending involved.

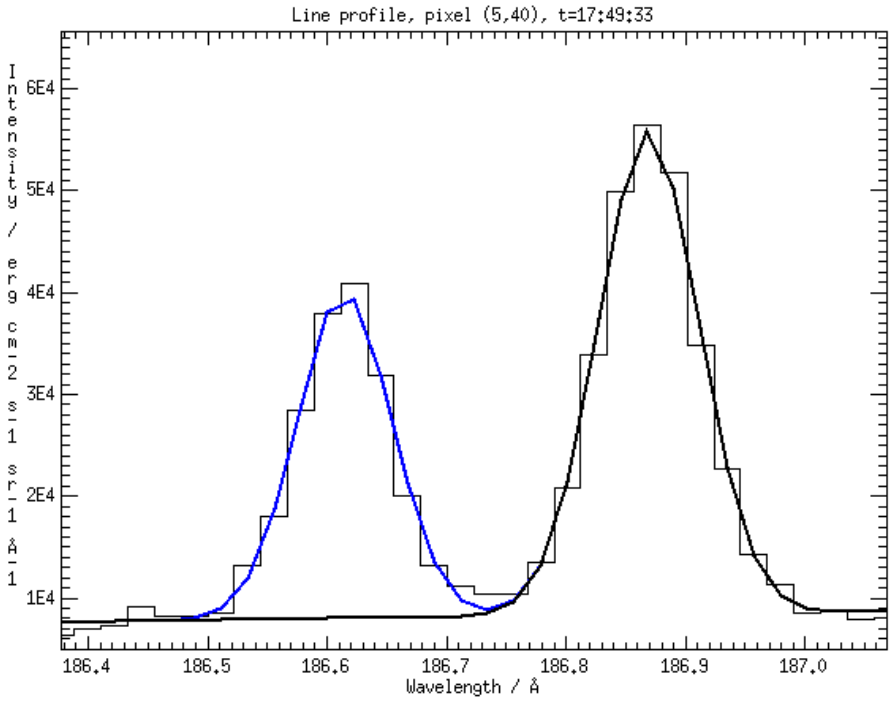

Figure 2.8: A screenshot showing the line profile and Gaussian fitting of the Fe XII line at 186.85Å, in black, and the neighbouring Fe VIII and Ca XIV blend at 186.61Å, in blue. Again the histogram represents the data and the solid lines are Gaussian fits.

The decision was then made to use the other Fe XII line 186.85Å instead, as it had no blends but did have one other emission feature present in the wavelength window. Therefore, a double Gaussian was used for this line, fitting to the Fe XII line and the neighbouring feature which is a Fe VIII and Ca XIV blend. The plot in Figure 2.1 shows the fitting used and the position of the emission lines in the wavelength window, and the intensity maps can be found in Figure 2.9. The Fe XII emission is very strong in the first raster before the impulsive phase, however, this drops rapidly at 17:44:00 during this phase of the flare. After this Fe XII emission picks up during the peak and gradual phase returning to a steady level at a fraction of what it was previously. The emission is a source of footpoints as it is very concentrated in certain places and matches with what is seen in corresponding AIA images (Section 2.7). The reason for

the sudden decrease during the impulsive phase and peak is due to the large increase in temperature of the plasma causing hotter lines to be produced.

2.4.2.2 Fe XVII 269.42Å

Fe XVII was investigated as a potential comparison to EVE data as it is also a hot emission line with a counterpart in EVE Fe XXIII at 132.906Å. The EIS wavelength window had a range of 268.81 Å to 269.48Å and two lines were present requiring a double Gaussian fit. These two lines were Mg VI 268.99Å and Fe XVII 269.42Å. By extracting the peak value of the Gaussian profile in Fe XVII the intensity map could be plotted for this line. These rasters can be seen in Figure 2.10. Before the impulsive phase of the flare there is very little Fe XVII emission in the first couple of rasters. This is because the surrounding plasma is not at a high enough temperature to produce the emission, however, Fe XII emission can be and is seen in the corresponding rasters. From the rasters it can be observed that Fe XVII reaches a peak intensity just after the peak of the flare before it gradually dims. The source of the Fe XVII emission is again from the footpoints and ribbons within the EIS raster. The timing of the peak is due to the line not being a flaring line like Fe XXIII and hence has a lower temperature. After the peak of the flare the emission dims gradually as the plasma relaxes some flowing back to the surface and cooling.

2.4.2.3 Fe XXIII 263.76Å

This is exactly the same line that was investigated in the 2011 flare in Section 2.4.1.3, however, there is a slight difference in the EIS wavelength window. For this flare the wavelength window has a range of 262.69Å to 264.09Å meaning part of a Fe XVI line is now present at 262.97Å. This meant a double Gaussian had to be used, though this did not prove to be of any difficulty as both lines were considerably isolated from each other. The intensity maps in Figure 2.11 show an increase in Fe XXIII emission as the flare progresses. In rasters 17:41:46 and 17:44:00 there is very little Fe XXIII emission which is spread unevenly across the active region. This is because the plasma in the

region is not hot enough to produce the Fe XXIII emission. At 17:48:28 the Fe XIII emission becomes very intense in one particular spot as all of the Fe XXIII emission originates from a group of coronal loops and footpoints on the disk of the Sun. As the flare progresses the Fe XXIII emission dims gradually as the active region cools and relaxes. This is typical behaviour expected from a hot flaring line such as Fe XXIII, where the emission will continue to dim until the active region returns to its original state seen in the first couple of rasters.

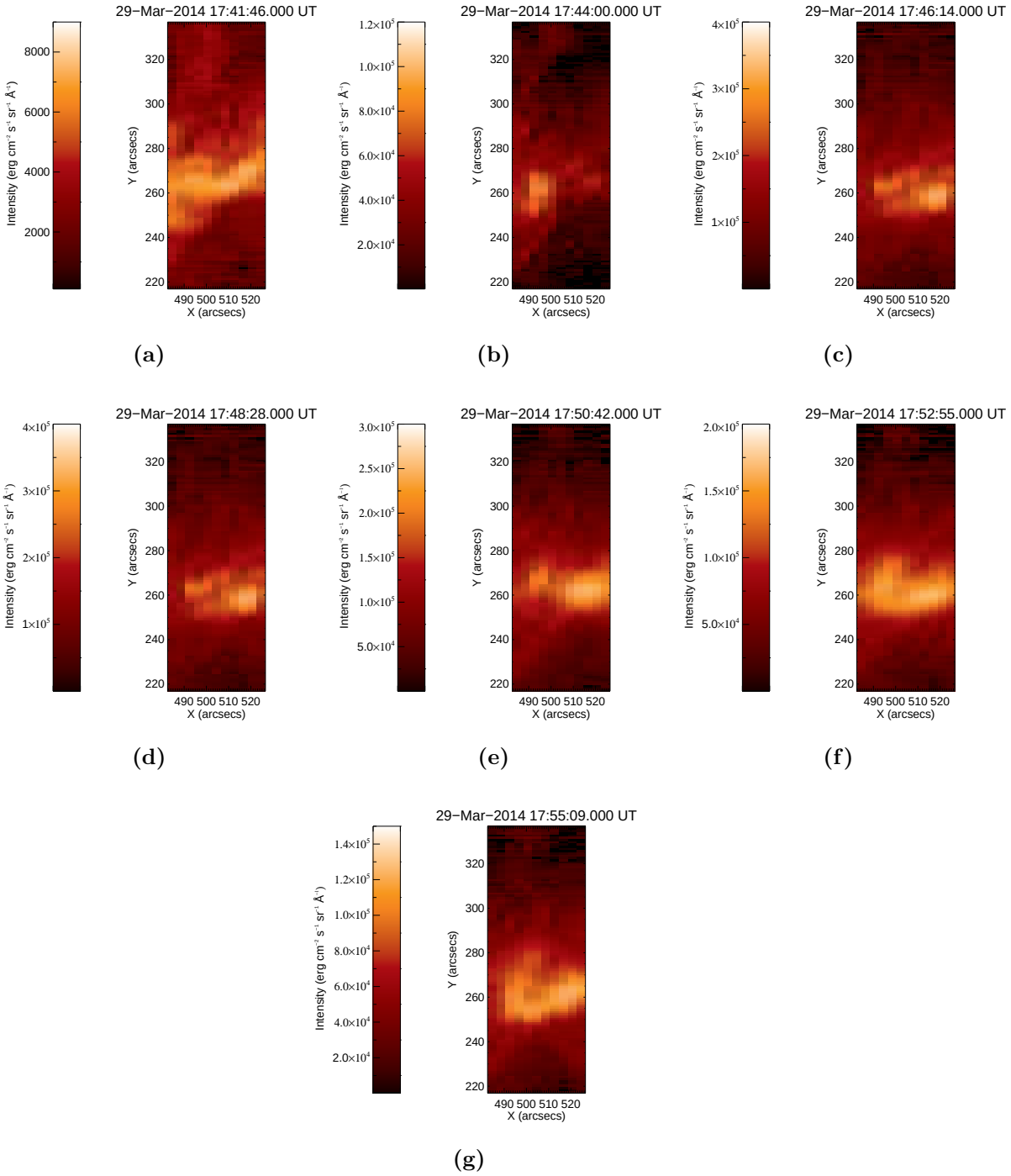

Figure 2.9: Intensity Maps (a) - (g) show the changing intensity of Fe XII 186.85Å at the observed active region during the SOL2014-03-29T17:48 event, as seen by EIS with respect to time.

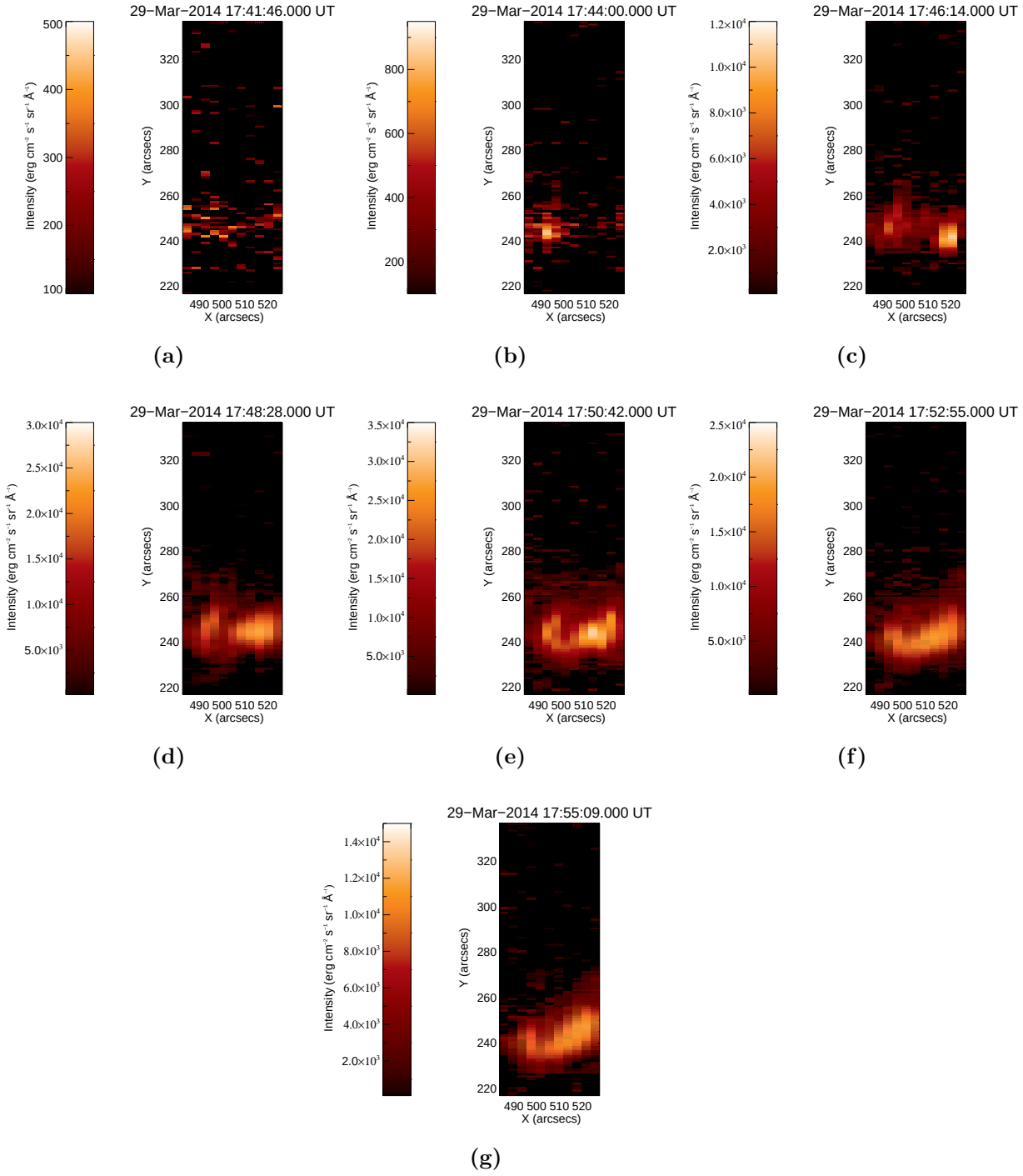

Figure 2.10: Intensity Maps (a) - (g) show the changing intensity of Fe XVII 269.42Å at the observed active region during the SOL2014-03-29T17:48 event, as seen by EIS with respect to time.

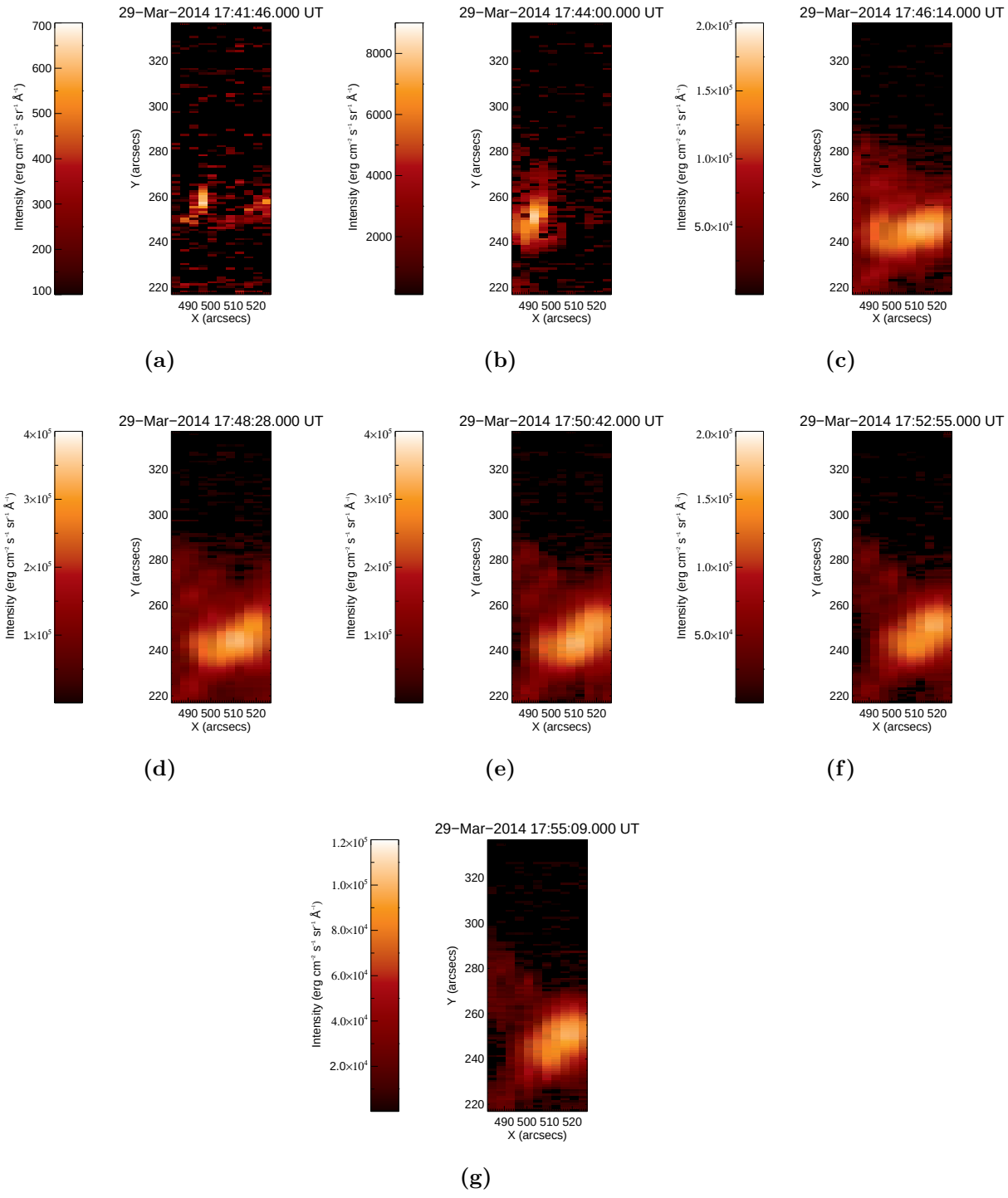

Figure 2.11: Intensity Maps (a) - (g) show the changing intensity of Fe XXIII 263.76Å at the observed active region during the SOL2014-03-29T17:48 event, as seen by EIS with respect to time.

2.5 Doppler Velocities

Another parameter which is obtained from the Gaussian fit is the centroid wavelength. It can be used to calculate corresponding Doppler velocities of the line profiles. The centroid wavelength can be used in the following equations to calculate the Doppler velocity of each pixel.

$$v = \Delta\lambda \frac{c}{\lambda_{rest}} \tag{2.1}$$

$$\Delta\lambda = \lambda_{observed} - \lambda_{rest} \tag{2.2}$$

Where $\lambda_{observed}$ is the centroid wavelength value obtained for the Gaussian fitting, λ_{rest} is the rest wavelength for the emission line, c is the speed of light and v is the Doppler velocity. Where possible the rest wavelength was obtained as the observed rest wavelength of quiet Sun emission in the EIS rasters before the flare begins. This proved to be easy for for cooler lines such as O VI and Fe XII, however, it was more complicated for hotter lines such as Fe XVII and Fe XXIII. This is because there is no quiet Sun emission of these lines as they only appear during the flare when they are no longer at rest. This poses a great difficulty in calculating a rest wavelength and so, the CHIANTI wavelengths were used instead as the rest wavelengths for these lines. From these values velocity maps of the EIS raster can be obtained showing the plasma flow of the flaring region at a particular instant in time.

2.6 Velocity Maps

These velocity maps are of particular importance as the information from each pixel will be compared to EVE velocity values. This will be described in greater detail in Chapter 4.

2.6.1 SOL2011-02-16T07:35

2.6.1.1 O VI 184.117Å

Before Doppler velocities can be calculated, a rest wavelength for O VI has to be established. To establish a rest wavelength measurements of centroid wavelengths from quiet Sun emission measurements were averaged over a small area on the EIS raster. This emission was typically taken from the bottom corner of the EIS raster, where the first raster was used, so the 07:38:36 raster was used in this case. The result of this was a rest wavelength of 184.13 Å which was used throughout all Doppler velocity calculations of O VI using Equations 2.1 and 2.2 and had a difference from the CHIANTI wavelength of 0.013Å corresponding to 21km/s. These Doppler velocities were then viewed as velocity maps and can be seen in Figure 2.13.

By observing the velocity maps of O VI in Figure 2.13 the plasma flow speeds and directions can be seen. A clear blueshift can be seen from all rasters with velocities between -20 km/s and -50 km/s. There is also an element of stationary velocities before the peak of the flare in rasters 07:38:36 and 07:56:03, indicating a build up of plasma before the event. However, all rasters lean very heavily towards an overall blueshift with small components of redshift scattered in the surrounding area. As the Doppler velocities seen are emanating from a coronal loop it is expected to have blueshifts over the loop and redshifts near the footpoints. This is what would be expected during a smaller flare as O VI is a transition region line and so this will be chromospheric evaporation at work causing upflows.

2.6.1.2 Fe XII 195.12Å

The same process discussed in Section 2.6.1.1 was used for calculating the rest wavelength of Fe XII. Quiet Sun emission was taken from the bottom left hand corner of the EIS raster at 07:38:36 and averaged to calculate a rest wavelength of 195.13Å. This value was applied to the Doppler velocity Equations 2.1 and 2.2 and the results were plotted in velocity maps which can be seen in Figure 2.14.

The velocity maps of Fe XII show very strong redshifts at the footpoint of the

flaring region with velocities in the range of 20 - 30 km/s. Background emission shows strong blueshifts of around -10 to -20 km/s. During the flare peaks at 07:44:25 and 08:01:52 there is a lot of stationary components surrounding the strong redshift at the footpoints. This is what is expected, suggesting a build up of plasma in the coronal loop. Redshifted emission suggests the Fe XII emission is from plasma flowing down to the surface of the Sun, occurring after the flare and moving across the observed region of coronal loops.

2.6.1.3 Fe XXIII 263.76Å

Calculating a rest wavelength for the flaring emission line Fe XXIII cannot be done in the same way as for the other lines. This is because this line does not appear in quiet Sun emission due to its very high peak formation temperature, but only appears during the impulsive and gradual phase of the flare. By this point the line already has the potential to be shifted and so will not be at a rest wavelength. Due to this, an alternate method must be used to determine the rest wavelength of the hot-temperature Fe XXIII line. The most commonly accepted method is to determine centroid wavelength values during the gradual phase of the flare, once the flare flows have decreased. However, this provides additional problems in EIS data due to the sensitive change in temperature of the EIS detectors in Hinode's orbit (Milligan & Dennis 2009). This would need to be considered if using emission during the gradual phase and can prove to be more complex. As a result of this the decision was made to use the CHIANTI wavelength of FE XXIII as the rest wavelength. The value of 263.76Å was used in Equations 2.1 and 2.2 in the calculation of Doppler velocities. The corresponding velocity maps for Fe XXIII can be seen in Figure 2.15.

The velocity maps of Fe XXIII show a very unusual structure of blue and redshifted plasma during the flare. It is known from AIA images (section 2.7) that the area consists of a few coronal loops. It would appear from the velocity maps that the plasma is rotating, flowing out from the surface before falling back down again. This phenomenon is partially caused by an instrumental effect and is due to an elliptical,

tilted point spread function (PSF), illustrated in Figure 2.12 (Haugan 1999).

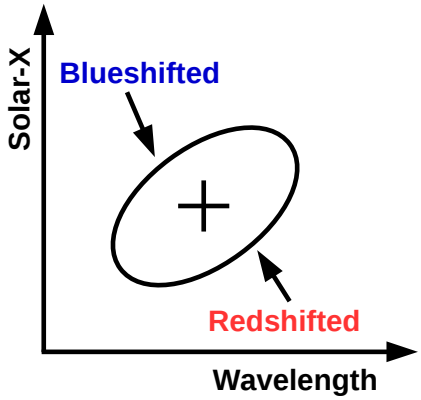

Figure 2.12: This diagram shows the point spread function (PSF) expected to be present in the EIS detector as a result of an instrumental error. It was hypothesised by Haugan (1999) as present in the SOHO/CDS mission.

A PSF similar to the one in Figure 2.12 will provide an elliptical spot on the EIS detector with an axis at an angle to that of the detectors. This will then spread across a number of pixels on the detector and if Gaussian fits are applied to the data of each pixel a blushift will appear on the north side and a redshift on the south side. Young et al. (2012) stated the effect simply as "Whenever there is a decreasing intensity gradient from north to south, the centroid of the the emission line will be artificially shifted to longer wavelengths (redshift); and whenever there is an increasing intensity gradient from north to south, the centroid of the emission line will be artificially shifted to shorter wavelengths (blueshift)" (Young et al. 2011).

This has not been proven yet for EIS data, however, velocity patterns obtained during many events suggest it is similar to the SOHO/CDS phenomena discussed and presented by Haugan (1999). At the moment there is no software for IDL to correct this instrumental effect, however, an observation has been made providing rough estimates of the velocities of this effect. If a velocity is measured at the intensity peak (along y-direction) then a velocity of up to 5km/s will be measured to the south of the brightening. Similarly, a velocity of up to -5km/s will be measured to the north

of the brightening (Young et al. 2011). However, the values found in the Fe XXIII line for this flare are much larger than 5km/s and -5km/s suggesting that real plasma flows are actually present in the active region. I do not believe the pattern is caused by rotational plasma but is the effect of multiple coronal loops - with predominantly upflows on one side and downflows on the other. It is clear that the large blueshifts of around -50km/s and redshifts of around 75km/s, are the cause of plasma flows in the coronal loops moving between the footpoints and other surrounding loops.

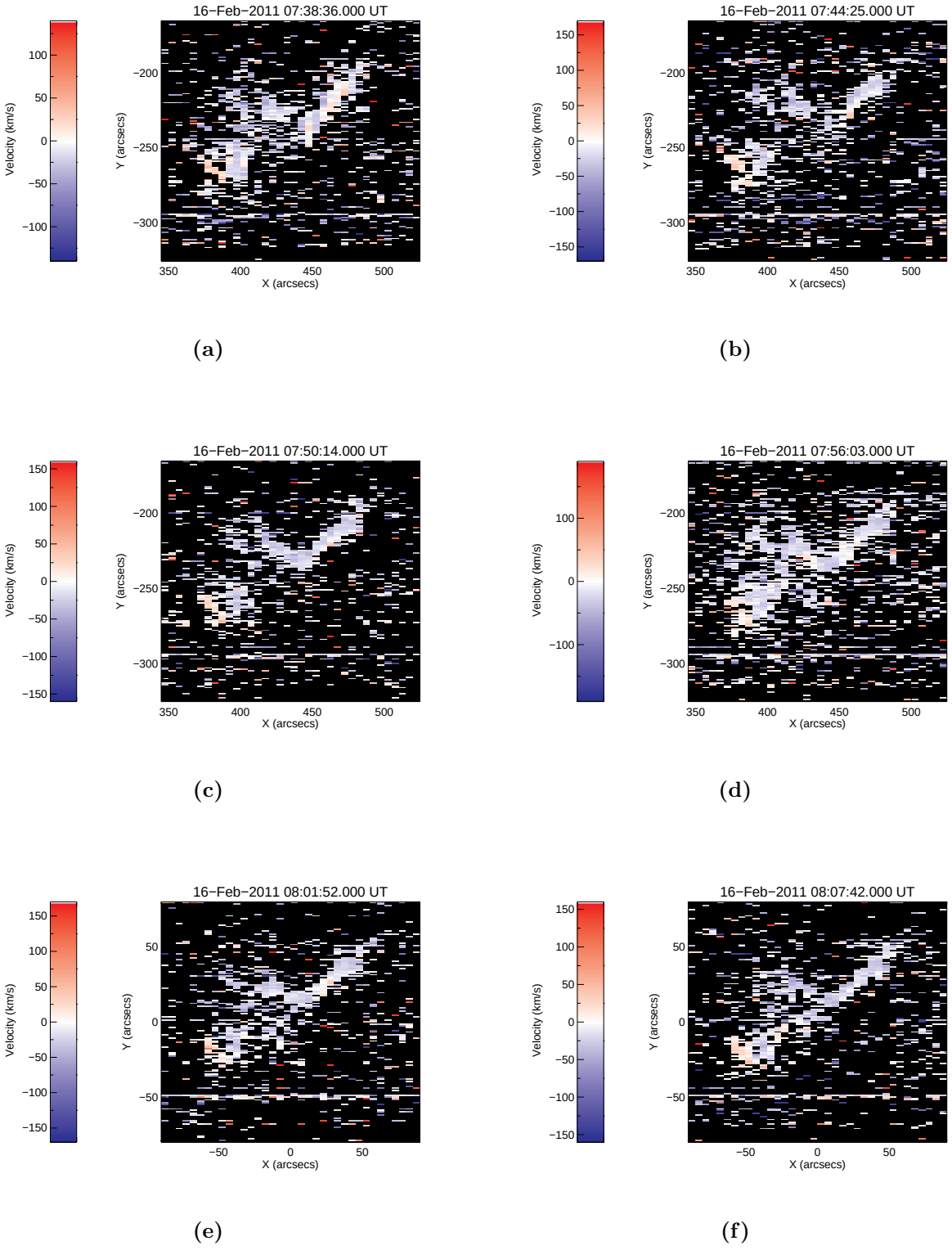

Figure 2.13: Velocity Maps (a) - (h) show the changing Doppler velocity of O VI 184.119Å at the observed active region during the SOL2011-02-16T07:35 event, as seen by EIS with respect to time. Black pixels are due to no line emission being present at that location, hence no fitting was made.

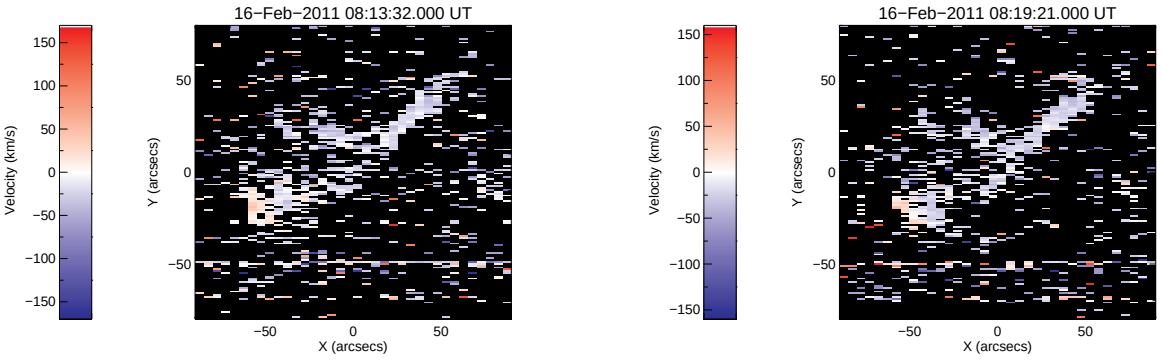

(g) **(h)**

Figure 2.13: Cont. Velocity Maps (a) - (h) show the changing Doppler velocity of O VI 184.119Å at the observed active region during the SOL2011-02-16T07:35 event, as seen by EIS with respect to time. Black pixels are due to no line emission being present at that location, hence no fitting was made.

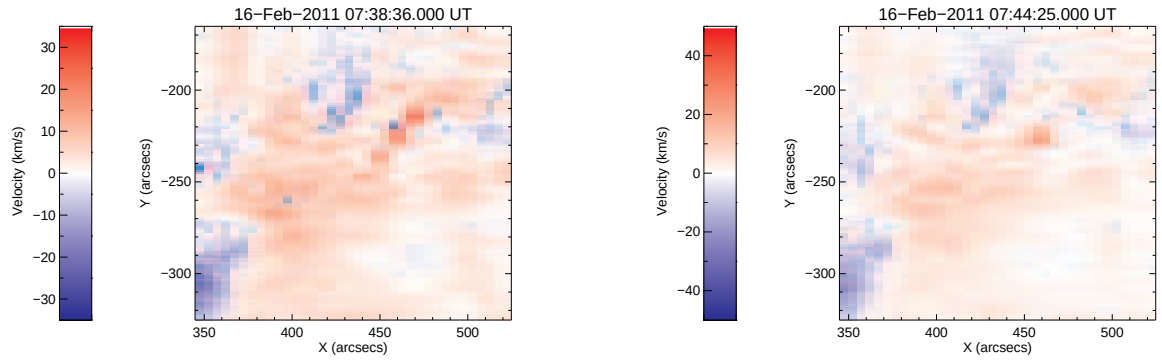

(a) **(b)**

Figure 2.14: Velocity Maps (a) - (h) show the changing Doppler velocity of Fe XII 195.12Å at the observed active region during the SOL2011-02-16T07:35 event, as seen by EIS with respect to time.

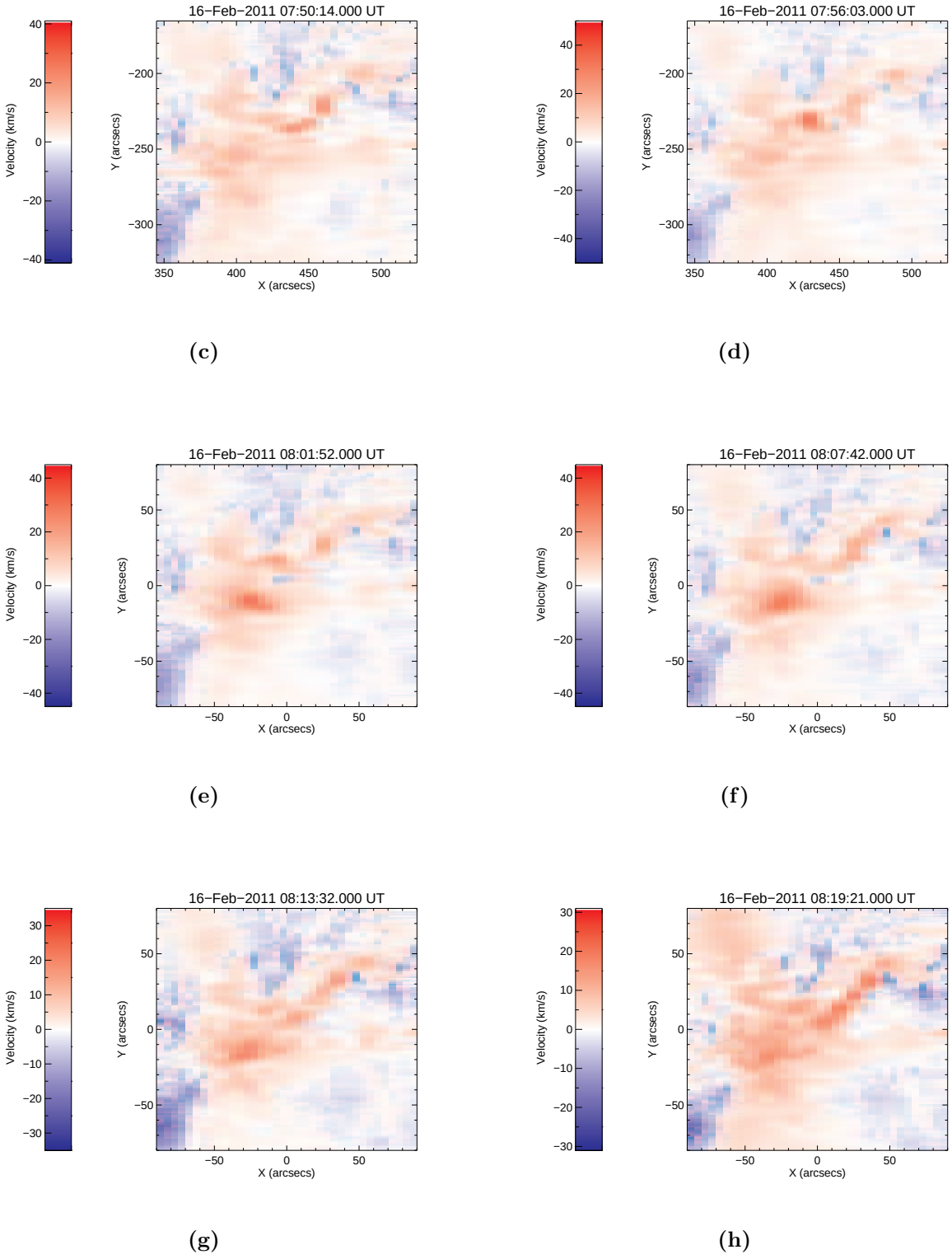

(c) **(d)**

(e) **(f)**

(g) **(h)**

Figure 2.14: Cont. Velocity Maps (a) - (h) show the changing Doppler velocity of Fe XII 195.12Å at the observed active region during the SOL2011-02-16T07:35 event, as seen by EIS with respect to time.

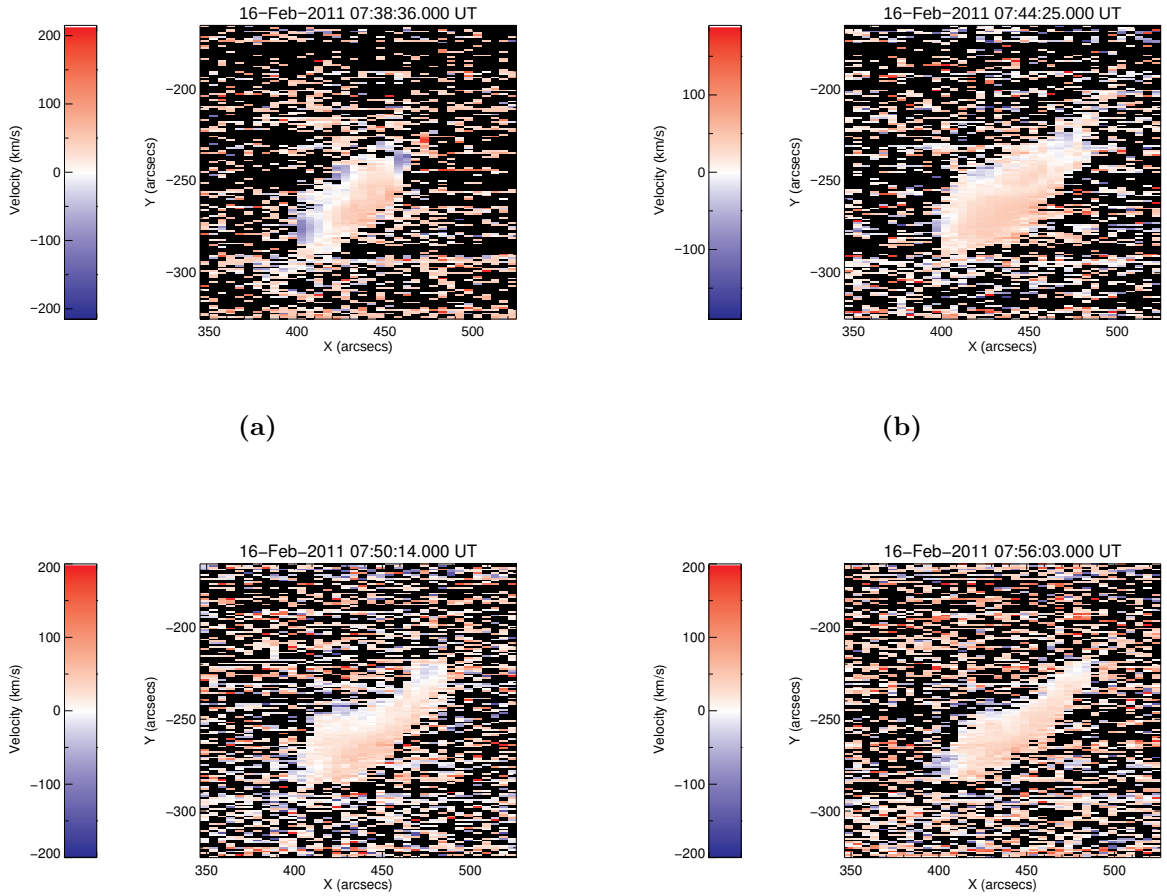

Figure 2.15: Velocity Maps (a) - (g) show the changing Doppler velocity of Fe XXIII 263.76Å at the observed active region during the SOL2011-02-16T07:35 event, as seen by EIS with respect to time. Black pixels are due to no line emission being present at that location, hence no fitting was made.

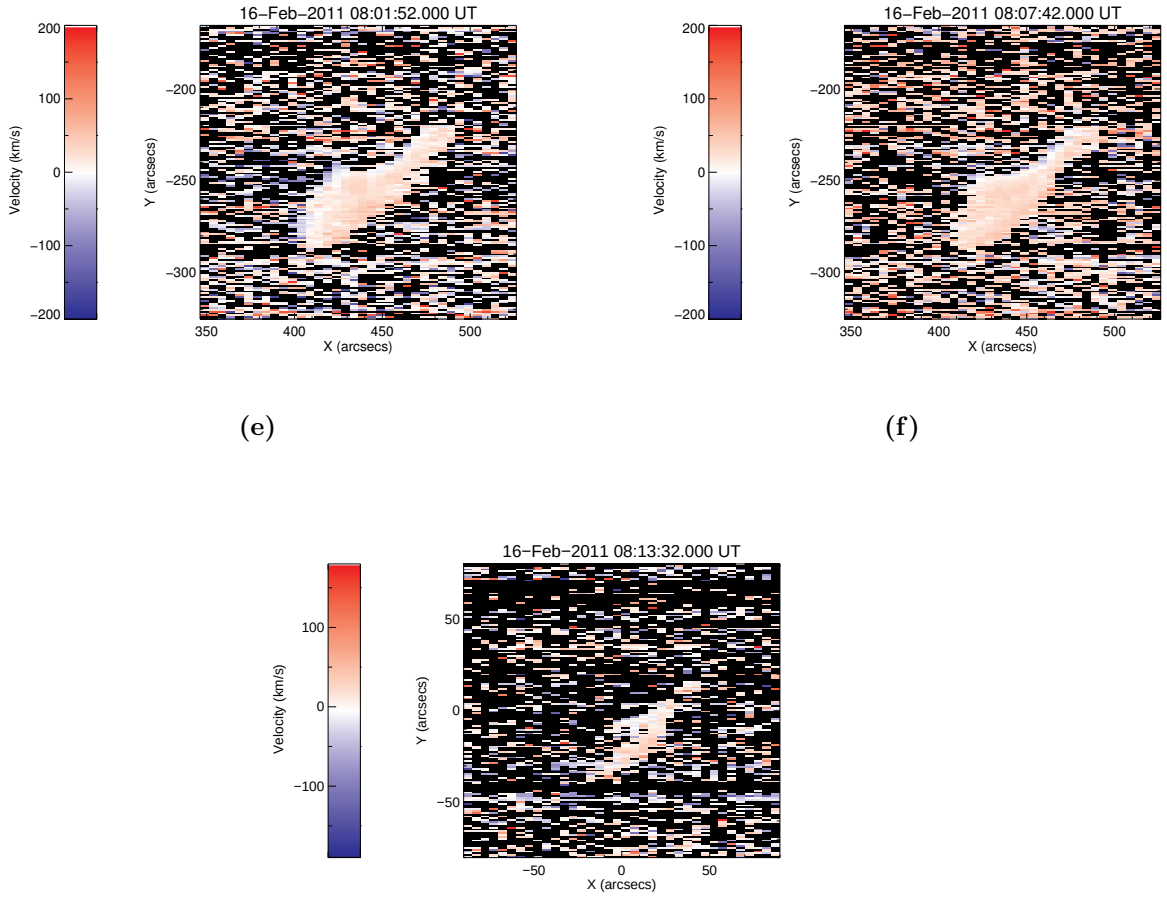

Figure 2.15: Cont. Velocity Maps (q) - (w) show the changing Doppler velocity of Fe XXIII 263.76Å at the observed active region during the SOL2011-02-16T07:35 event, as seen by EIS with respect to time. Black pixels are due to no line emission being present at that location, hence no fitting was made.

2.6.2 SOL2014-03-29T17:48

2.6.2.1 Fe XII 186.85Å

Again, the same method as discussed in Section 2.6.1.1 was used to calculate the rest wavelength of Fe XII, however, this is a different emission line compared to the Fe XII line used in the previous flare. Emission of the quiet Sun was taken from the bottom of the EIS raster at 17:41:46 and averaged to calculate a rest wavelength. This gave a value of 186.87Å and was used in Equations 2.1 and 2.2 to determine Doppler velocities. These Doppler velocities were then plotted as velocity maps and can be seen in Figure 2.16.

Velocity maps of Fe XII show the plasma flows during the flare in the active region and surrounding areas within the EIS raster. A strong blueshifted component is present in rasters 17:41:46 and 17:44:00 with a value in the range of -75km/s - -100km/s. It is at this time, during the impulsive phase of the flare, where there is a build up of plasma occurring in the corona as a result of the twisting magnetic field before the flare. This is when Fe XII emission is at its strongest and is represented and seen clearly in the rasters. After this strong blueshift, there is very little blueshifted components and a redshift between 25km/s - 50km/s is dominant. This redshift progressively gets stronger as the surrounding active region cools after the event. In this case the Fe XII emission becomes more redshifted as it falls back down to the surface of the Sun during the cooling. In addition, as the plasma cools more Fe XII emission is produced and so there is more movement of Fe XII dominating the raster. This suggests a downwards flow of plasma back to the surface of the Sun as the flare progresses and then becomes quiet again.

2.6.2.2 Fe XVII

Velocity maps were calculated from the wavelength centroid Gaussian fit values retrieved from fitting to the Fe XVII emission line. These values were then used to calculate Doppler velocities using a rest wavelength of 269.42Å and Equations 2.1 and 2.2, the resulting velocity maps can be seen in Figure 2.17. The rest wavelength was

taken from the CHIANTI line list due to there being no background emission of this line. This is due to it being a hot line and hence only present when the flare has begun, when flows will already be present.

From the velocity maps it can be seen that there is a strong blueshifted component around -100km/s and possible higher in the 17:44:00 and 17:46:14 rasters. The blueshift is the cause of building plasma in the corona and then a subsequent release during the flaring event itself. This is swiftly followed by an overall redshift of between 25 - 50km/s which appears during the peak and gradual phase of the flare. This can be described as the Fe XVII emission cooling and the active region settling down in the aftermath of the flare. Also, during the peak of the flare the plasma becomes hotter producing flare lines such as Fe XXIII which, dominate leaving other Fe lines to settle and their flows to reduce.

2.6.2.3 Fe XXIII 263.76Å

Again the CHIANTI wavelength of 263.76Å was used as the rest wavelength for this emission line. Once more, Equations 2.1 and 2.2 were used to calculate the Doppler velocities of Fe XXIII and can be viewed as velocity maps in Figure 2.18.

EIS Doppler velocity maps provide valuable information regarding the movement of plasma flows during the flare. The first two rasters of Fe XXIII display little relevant Doppler velocities due to no emission of the line being present. However, there is a small amount of emission in raster 17:44:00 at a location of $x = 490$ and $y = 240$ displaying a clear blueshift of around -50km/s. This dies down as the flare progresses further and more blueshifted components can be seen, possibly representing footpoints in the active region. During the peak of the flare at 17:48:28 there are a few strong points of blueshifted pixels present with velocities in the region of -50km/s and a large amount of pixels with almost zero velocity. During the gradual phase of the flare blueshifts at the footpoints remain constant with background emission appearing redshifted. This is typical behaviour of a flare as the blueshifted footpoints represent the plasma evaporating into the corona, and the redshifts representing a relaxation

phase as the plasma flows back down to the surface.

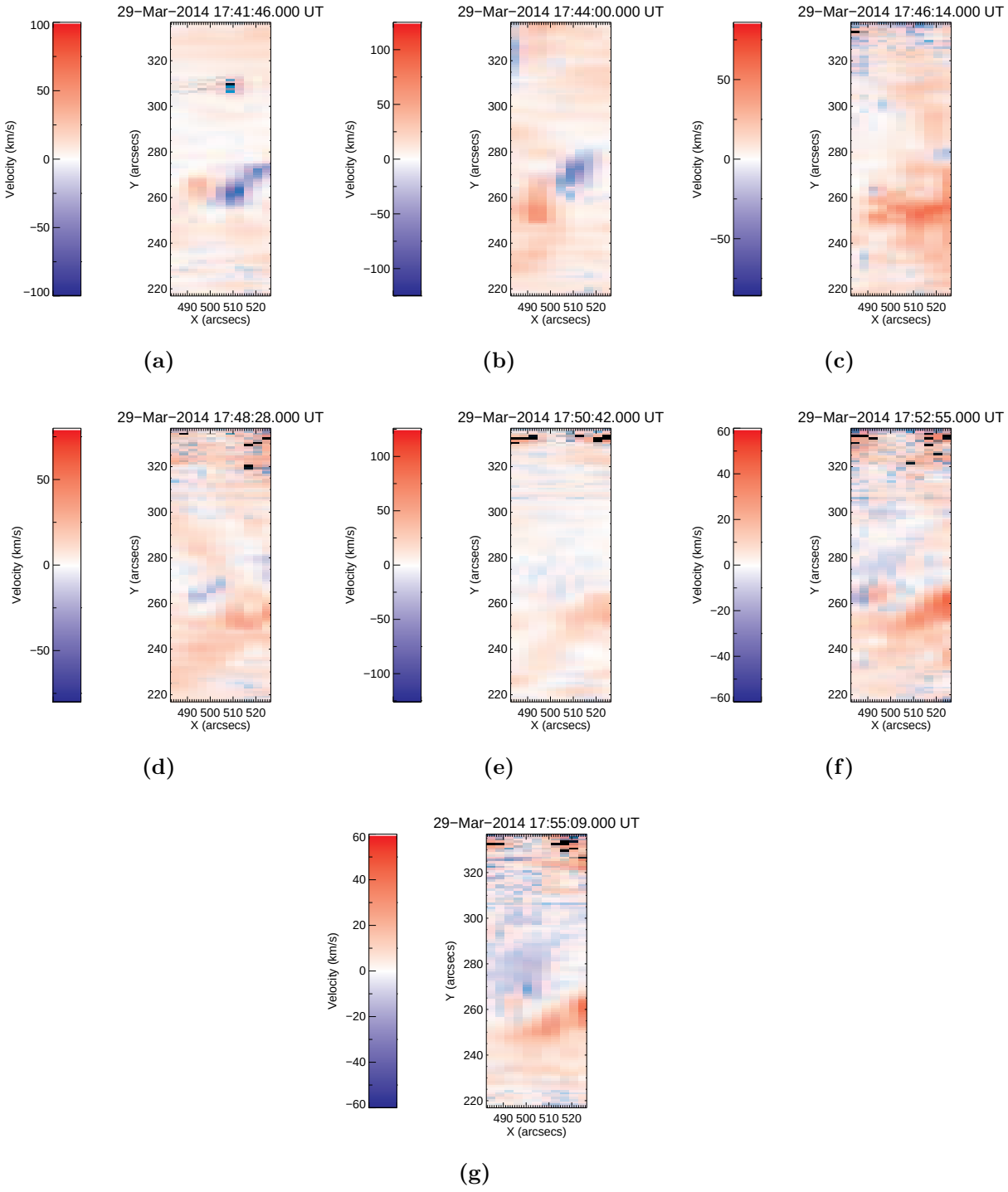

Figure 2.16: Velocity Maps (a) - (g) show the changing Doppler velocity of Fe XII 186.85Å at the observed active region during the SOL2014-03-29T17:48 event, as seen by EIS with respect to time.

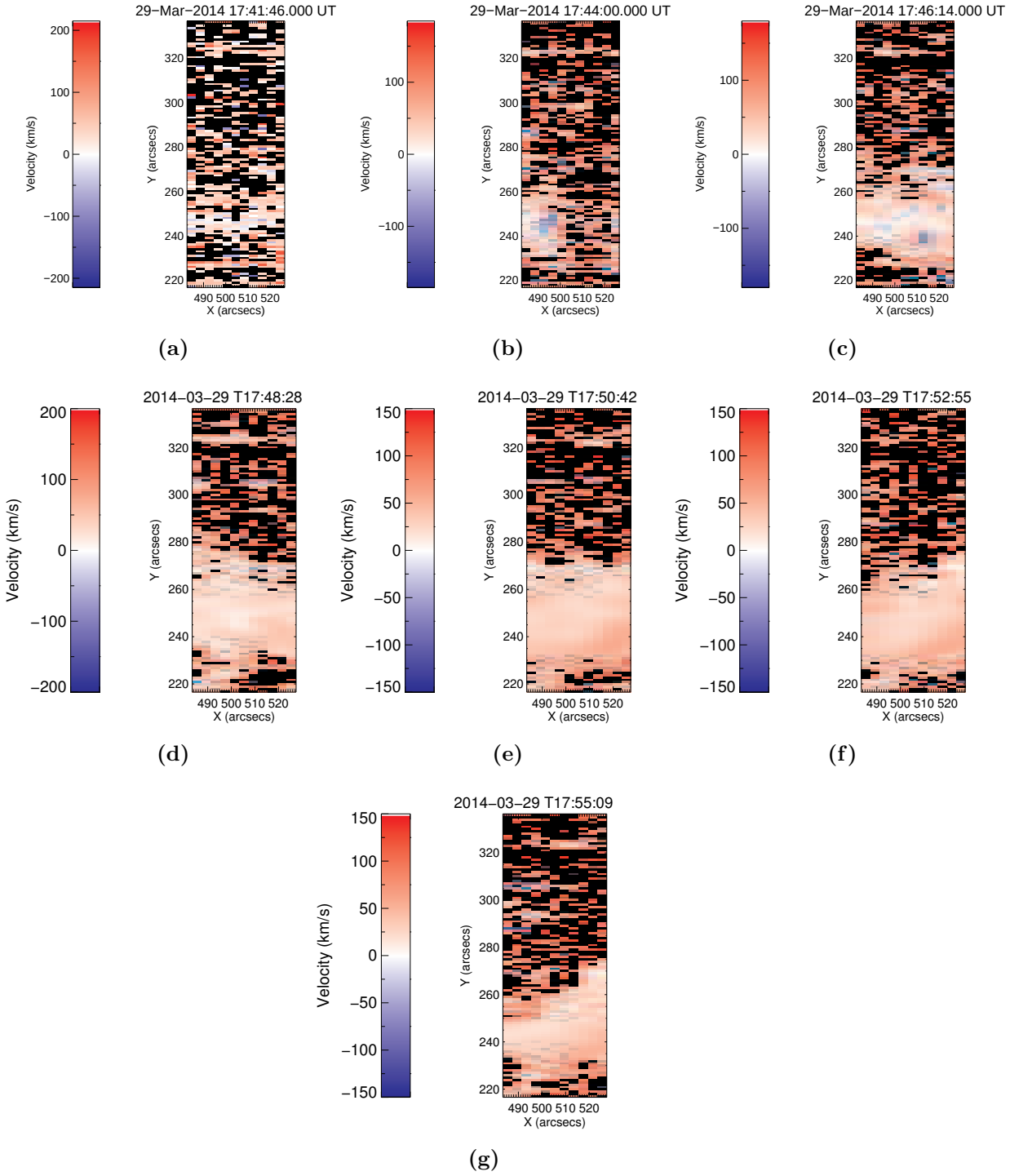

Figure 2.17: Velocity Maps (a) - (g) show the changing Doppler velocity of Fe XVII 269.42Å at the observed active region during the SOL2014-03-29T17:48 event, as seen by EIS with respect to time. Black pixels are the cause of no line emission being present at that location, hence no fitting was made.

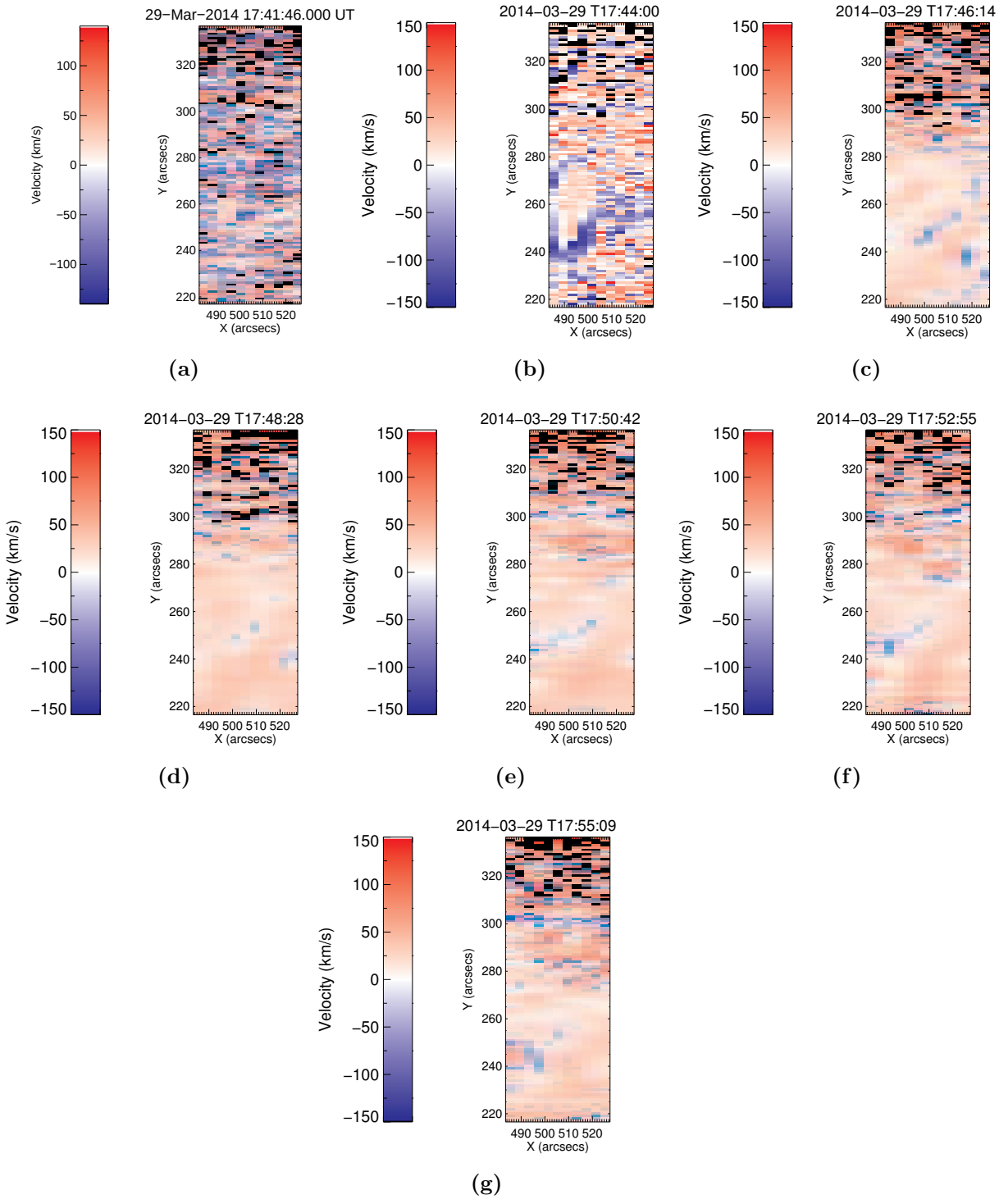

Figure 2.18: Velocity Maps (a) - (g) show the changing Doppler velocity of Fe XXIII 263.76Å at the observed active region during the SOL2014-03-29T17:48 event, as seen by EIS with respect to time. Black pixels are the cause of no line emission being present at that location, hence no fitting was made.

2.7 Comparing AIA images and EIS Rasters

When looking at the EIS intensity rasters it can be difficult to pinpoint exactly where the EIS field-of-view is observing in the active region and also what exactly is happening. To shed some light on these questions and to provide some aid in answering them, AIA images were looked at in comparison to the EIS rasters. By comparing the EIS field of view with the same region in an AIA image it became clearer what was being observed. A few examples of these can be seen in the following figures.

2.7.1 SOL2011-02-16T07:35

2.7.1.1 O VI

In Figure 2.19 maps of intensity, Doppler velocity and an AIA image of 1600Å at T07:50:17 are given. The 1600Å wavelength was chosen because it shows emission in the chromosphere and transition region which will allow the source of O VI to be established. From the AIA image sunspots can be clearly seen in the background along with a prominent ribbon or bright filament leaving one of the sunspots. A footpoint can also be seen near another sunspot on the left hand side. These features are believed to be the sources of O VI emission seen in the EIS intensity rasters.

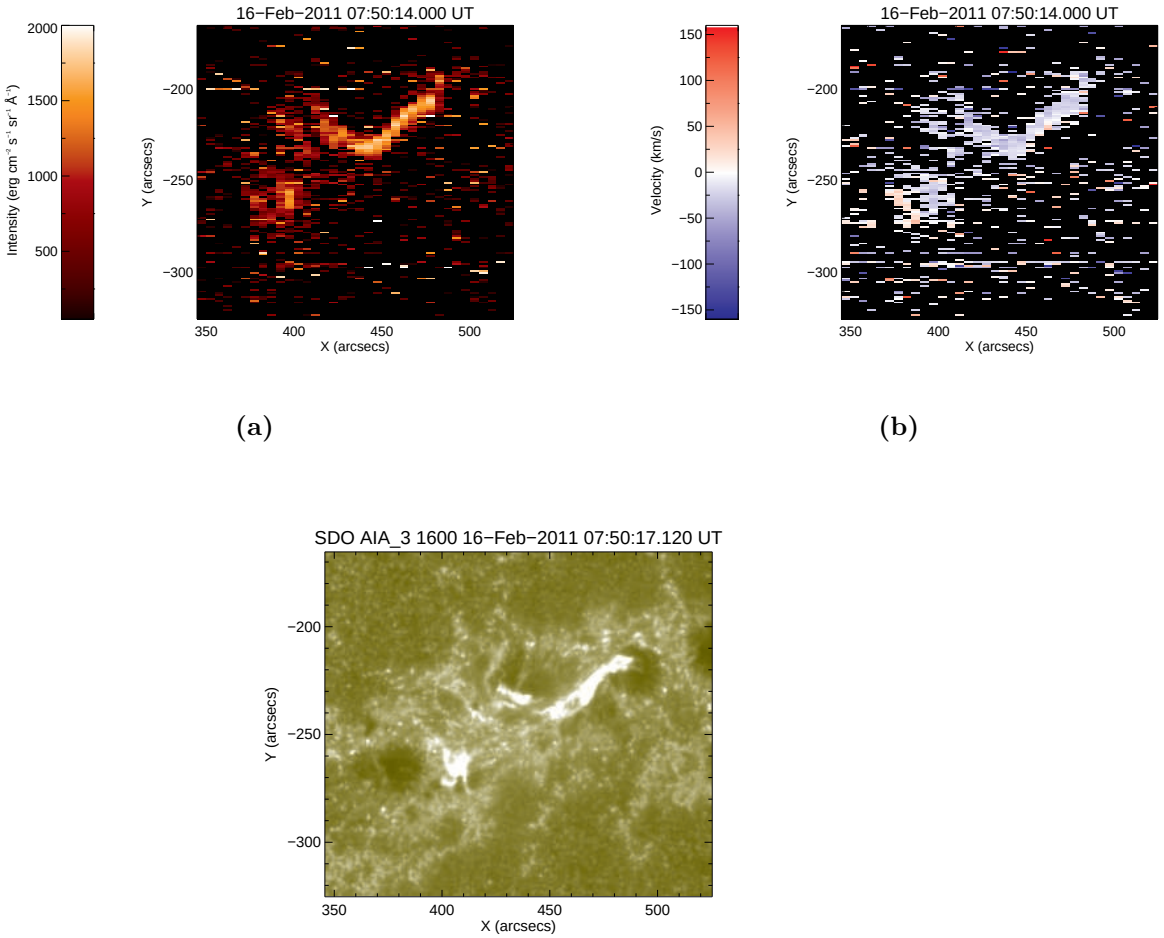

Figure 2.19: Three separate maps showing (a) the intensity of O VI, (b) the Doppler velocity of O VI and (c) the AIA image in 1600Å taken of the EIS field-of-view, all at a time of around 07:50

2.7.1.2 Fe XII

In Figure 2.20 maps of intensity, Doppler velocity and an AIA image of 171Å at T07:44:25 are given. The AIA image in 171Å shows detailed emission of the transition region and corona and by comparing it to the intensity and velocity maps the source of Fe XII emission can be determined. There are many features in the AIA

image including a clear and prominent brightening resembling a ribbon. Surrounding the ribbon are a network of coronal loops connecting the sources together. There is also a second brightening near the bottom left hand corner, which is also the source of many coronal loops, suggesting a footpoint is present. These are the main sources of Fe XII emission which can be seen in the intensity rasters during the flare.

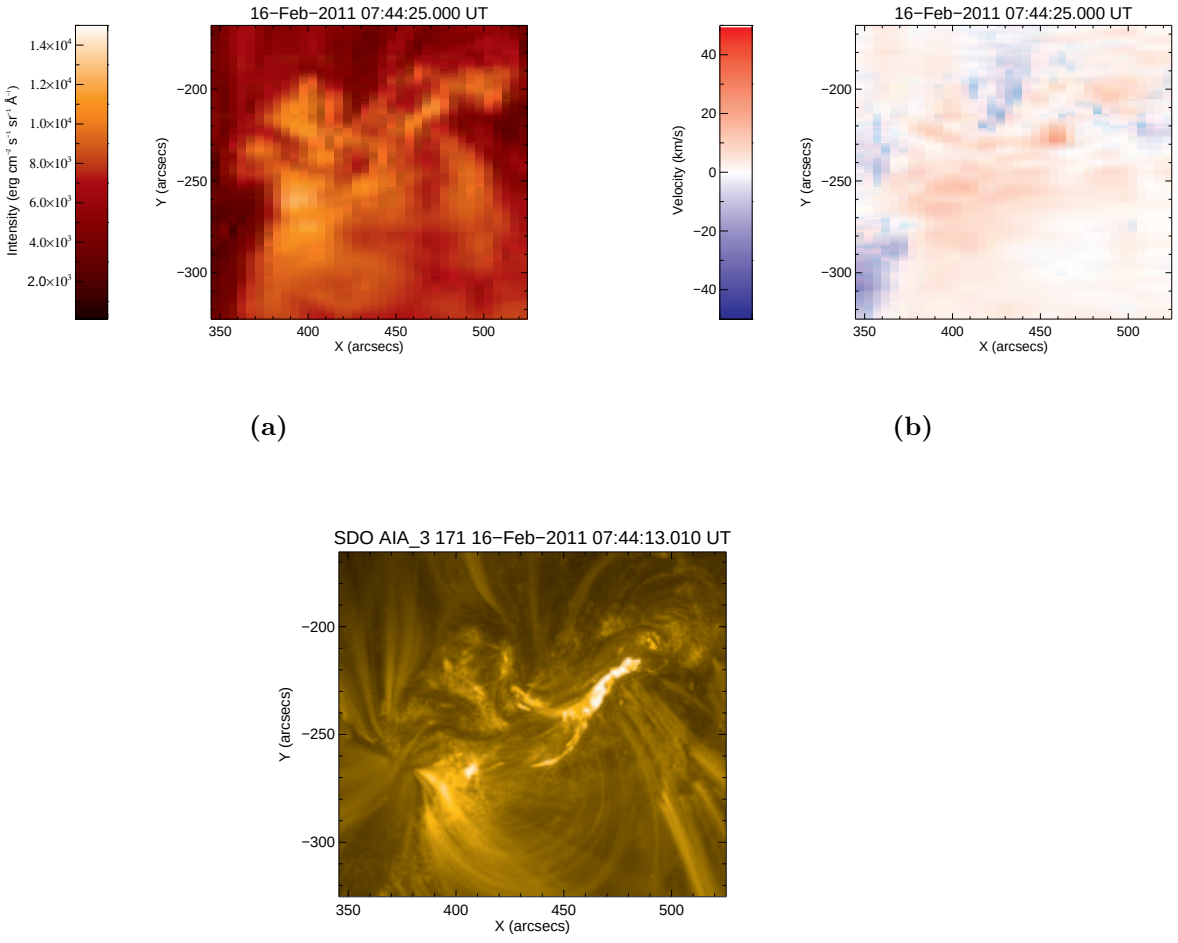

Figure 2.20: Three separate maps showing (a) the intensity of Fe XII, (b) the Doppler velocity of Fe XII and (c) the AIA image in 171Å taken of the EIS field-of-view, all at a time of around 07:44

2.7.1.3 Fe XXIII

In Figure 2.21 maps of intensity, Doppler velocity and an AIA image in 131Å at T07:38:21 can be seen. The AIA image at a wavelength of 131Å predominantly shows emission from flaring regions in the solar atmosphere at approximately 10MK. It is through the comparison of these that the sources of Fe XXIII emission and their evolution can be established. From the AIA image a clear and very bright coronal loop can be seen, dominating the image. It connects to a footpoint higher up near the middle on the image, however, there are other loops connecting to another footpoint further down. This array of footpoints and coronal loops is what produces the Doppler velocity pattern which appear to be moving from one side of the loop to the other. The Fe XXIII emission originates from the coronal loops appearing in intensity rasters to be concentrated in one position.

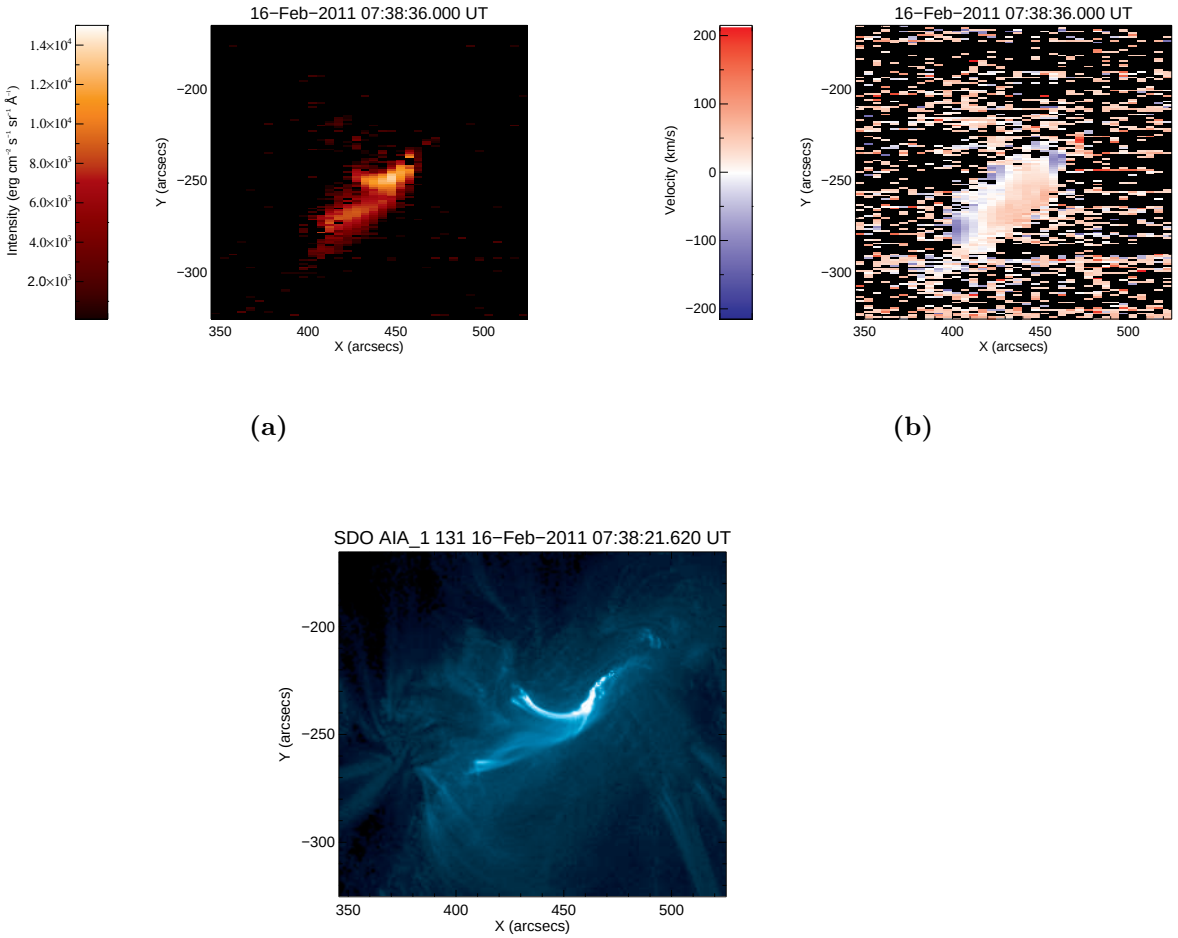

Figure 2.21: Three separate maps showing (a) the intensity of Fe XXIII, (b) the Doppler velocity of Fe XXIII and (c) the AIA image in 131Å taken of the EIS field-of-view, all at a time of around 07:38

2.7.2 SOL2014-03-29T17:48

2.7.2.1 Fe XII

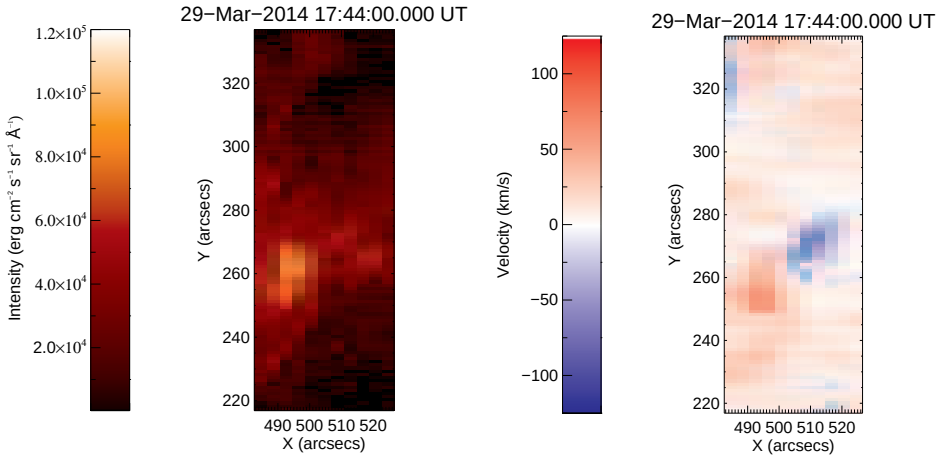

(a) **(b)**

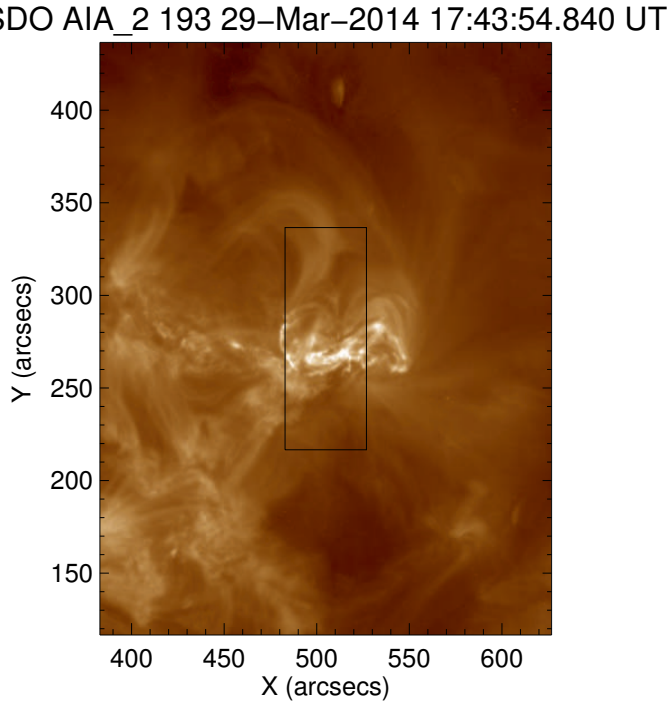

(c)

Figure 2.22: Three separate maps showing (a) the intensity of Fe XII, (b) the Doppler velocity of Fe XII and (c) the AIA image in 193Å taken of the EIS field-of-view, all at a time of around 17:44 and showing a broader FOV.

Figure 2.22 provides intensity and Doppler velocity maps along with an AIA image in 193Å at T17:43:54 to enable a comparison to be made. The AIA wavelength of 171Å shows emission in the transition region and corona allowing for the source of Fe XII emission during the flare to be determined. From the AIA image there appears to be a few ribbons surrounding a brighter spot which could be a footpoint. There are also large coronal loops appearing at the edges potentially from another footpoint outwidth the EIS FOV. To make a clearer judgement of what is occurring in this area a larger area of the disk was observed with the EIS FOV marked on top (Figure 2.22). It is now clear the Fe XII emission is originating from a set of ribbons potentially around two or more footpoints.

2.7.2.2 Fe XVII

Figure 2.23 shows the intensity and Doppler velocity maps along with an AIA image in 94Å at T17:44:01 showing emission in the flaring regions. It is clear from the AIA image that the Fe XVII emission originates from the footpoints and ribbons in the early stages and the coronal loops in the later stages of the flare.

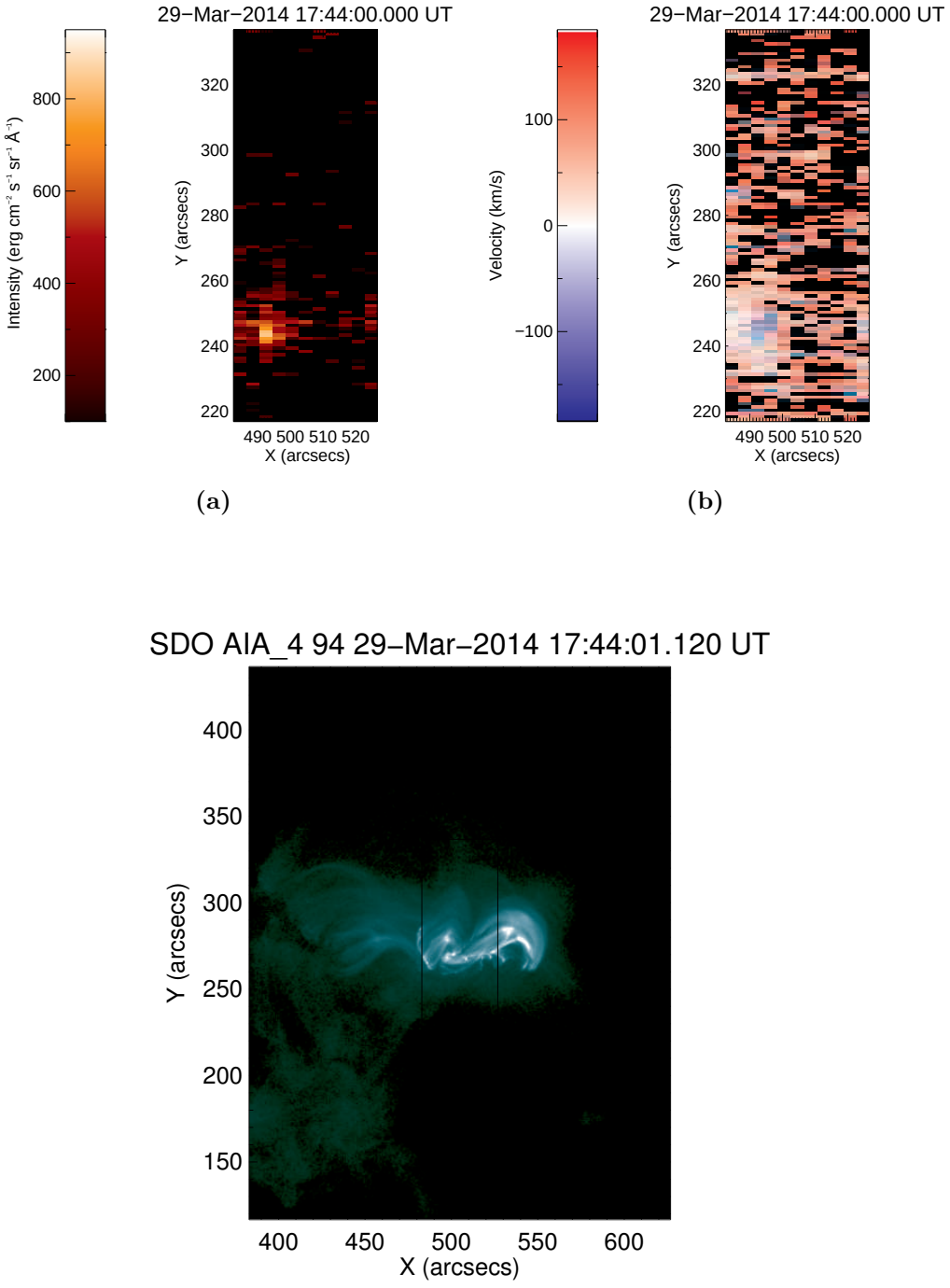

Figure 2.23: Three separate maps showing (a) the intensity of Fe XVII, (b) the Doppler velocity of Fe XVII and (c) the AIA image in 94Å taken of the EIS field-of-view, all at a time of around 17:44 and showing a broader FOV.

2.7.2.3 Fe XXIII

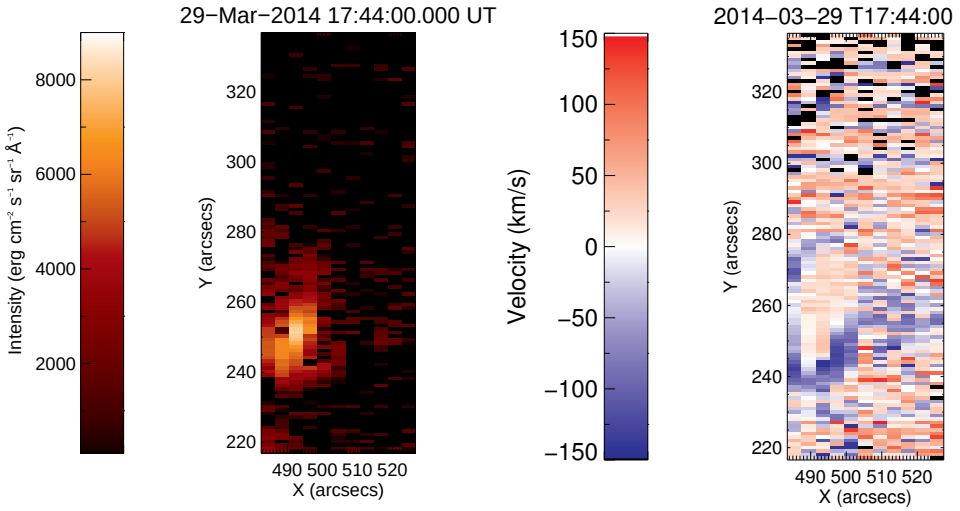

(a) **(b)**

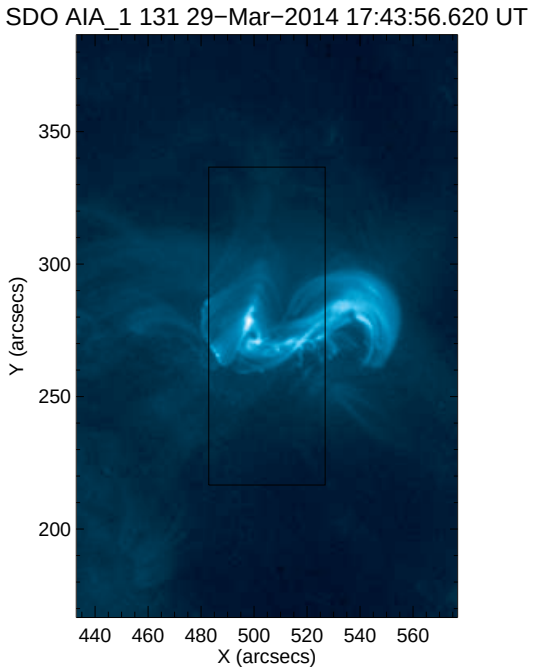

(c)

Figure 2.24: Three separate maps showing (a) the intensity of Fe XXIII, (b) the Doppler velocity of Fe XXIII and (c) the AIA image in 131Å taken of the EIS field-of-view, all at a time of around 17:44 and showing a broader FOV.

Figure 2.24 provides intensity and Doppler velocity maps along with an AIA image in 131Å at T17:43:56 showing detailed features of emission in the flaring regions. It is clear from the AIA image that many coronal loops are present, surrounding the ribbons and footpoints seen in previous AIA images. However, and extended view of the disk surrounding the EIS FOV was investigated to give a fuller picture of what was going on. From Figure 2.24, image (c), it is clear there are many coronal loops originating from footpoints and ribbons. There also appears to be an arcade of loops on the left hand side. It would seem this along with other coronal loops are the source of Fe XXIII emission.

It would appear from the AIA images in Sections 2.7.2.2 and 2.7.2.3 there is a misalignment in both the x and y axis of the EIS rasters. This is the cause of the EIS pointing which has been corrected for using the AIA offset, however, another cause could be the pointing offset between the long and short wavelength CCD's. There are also other factors to consider such as temperature fluctuations which can cause pointing issues. These have not been accounted for in the EIS rasters as it was not needed for the comparison being made here.

2.8 Conclusion

In this chapter EIS data has been successfully analysed for two large arcade flare events. Detailed descriptions of data analysis techniques used for extracting wavelength information were provided including programs used and methods applied. Intensity and Doppler velocity maps were produced and displayed for several emission different lines. These included various lines of varying temperature such as O VI, Fe XII, Fe XVII and Fe XXIII. Doppler velocity maps provided observations of plasma flows before, during and after the flare. The maps will be used in further analysis described in Chapter 4, when all data is combined and a comparison of both instruments can be made.

Chapter 3

EVE Data

3.1 Introduction

As we have now analysed data obtained for two flares SOL-2014-03-29T17:48 and SOL2011-02-16T07:35 using the EIS instrument on-board Hinode it is time to investigate the corresponding EVE data for the same events. EVE is onboard the Solar Dynamics Observatory (SDO), positioned in a circular geosynchronous orbit inclined by 28 degrees about the longitude of the SDO-dedicated ground station in New Mexico (Pesnell et al. 2012). Due to the nature of this orbit full disk observations of the Sun can be made 24 hours a day and this was intended as it is part of NASA's Living With A Star programme. However, EVE data poses some difficulties as flaring regions are not isolated as is done with EIS, and cooler lines tend to be difficult to discern in flares due to the disk also emitting brightly in these wavelengths. Despite these initial concerns many of the EVE lines were investigated and a few were used in comparison to the EIS lines.

As mentioned previously, EVE takes full-Sun spectral irradiance measurements every 10 seconds in wavelengths from 5 nm to 105nm, through the use of two separate spectrographs. Most of the lines investigated were measured by the MEGS-A spectrometer operating in a wavelength band of 5nm to 37nm, however, a few of the cooler oxygen lines were measured by MEGS-B. The Gaussian fitting and Doppler velocity

calculations used to analyse EVE lines are very similar to those of EIS, but, whereas EIS has many programs written in IDL for the extraction of spectral information, EVE does not. It was therefore, necessary to write many programs and commands in order to manipulate the EVE data. This chapter details all of the work carried out with the EVE data, including all of the steps taken to manipulate and extract all necessary information. All plots of light curves and any other relevant information will be displayed.

3.2 Spectral Lines Investigated

EVE takes measurements of approximately 5200 different and identifiable spectral lines all with a spectral resolution of 0.1 nm (Woods et al. 2012). However, there is a large problem with line blends in the spectral data partially due to EVE not being a high-resolution spectrometer like Hinode/EIS. Moreover line blends can appear and disappear due to transient sources of various temperatures, especially during flares and in active regions. With this in mind, it is imperative that great care is taken when selecting lines and creating fits in EVE spectra.

Previous work done by Del Zanna & Woods (2013) and Young et al. (2007) provided a starting point for lines which were good for the purpose of this project. Dr Hugh Hudson also provided a line list of many Fe lines (Hudson 2016) compiled over many years working with EVE spectra. Hudson's line list was created using other peoples' published work and by cross-comparison of observed spectra and Chianti line lists.

Table 3.1: The EVE spectral line list of selected ions and their corresponding wavelengths, where Tmax is the maximum formation temperature and Gmax is the maximum of the G(T) function from CHIANTI.

Wavelength (Å)	Ion	logT	EVE pixel location	Tmax	Gmax
131.24	Fe VIII	5.7	505	5.01×10^5	1.20×10^{-24}
171.073	Fe IX	5.9	705	7.29×10^5	5.30×10^{-23}
174.5310	Fe X	6.1	722	1.00×10^6	1.84×10^{-23}
177.23	Fe X	6.1	735	1.04×10^6	1.02×10^{-23}
184.536	Fe X	6.0	772	1.05×10^6	4.57×10^{-24}
188.216	Fe XI	6.1	790	1.20×10^6	5.74×10^{-24}
180.401	Fe XI	6.2	751	1.22×10^6	1.13×10^{-23}
195.120	Fe XII	6.2	825	1.38×10^6	1.11×10^{-23}
202.044	Fe XIII	6.2	860	1.66×10^6	3.55×10^{-24}
203.8280	Fe XIII	6.3	868	1.65×10^6	9.61×10^{-24}
211.331	Fe XIV	6.3	906	1.91×10^6	6.03×10^{-24}
264.7900	Fe XIV	6.3	1173	1.91×10^6	6.18×10^{-24}
270.519	Fe XIV	6.3	1202	1.91×10^6	2.23×10^{-24}
274.20	Fe XIV	6.3	1221	1.90×10^6	3.14×10^{-24}
284.1630	Fe XV	6.4	1270	2.25×10^6	2.64×10^{-23}
69.682	Fe XV	6.4	197	2.00×10^6	8.60×10^{-21}
335.410	Fe XVI	6.5	1526	3.07×10^6	1.21×10^{-23}
360.759	Fe XVI	6.5	1653	3.07×10^6	5.80×10^{-24}
98.249	Fe XVII	6.7	341	5.01×10^6	3.64×10^{-22}
093.9322	Fe XVIII	6.9	319	6.91×10^6	1.32×10^{-24}
103.95	Fe XVIII	6.8	370	7.58×10^6	4.18×10^{-25}
108.355	Fe XIX	6.9	392	8.28×10^6	9.62×10^{-25}

Wavelength (Å)	Ion	logT	EVE pixel location	Tmax	Gmax
121.845	Fe XX	7.0	459	1.00×10^7	7.03×10^{-21}
128.75	Fe XXI	7.0	493	1.10×10^7	1.94×10^{-24}
117.15	Fe XXII	7.1	435	1.20×10^7	1.61×10^{-24}
135.79	Fe XXII	7.1	528	1.27×10^7	1.34×10^{-24}
132.9065	Fe XXIII	7.2	514	1.58×10^7	2.49×10^{-20}
192.0285	Fe XXIV	7.3	809	2.00×10^7	1.03×10^{-20}
255.114	Fe XXIV	7.3	1126	2.00×10^7	$4,11 \times 10^{-21}$
97.7156	C III	4.2	4736	4.95×10^4	2.03×10^{-19}
303.783	He II	4.9	1368	8.86×10^4	4.61×10^{-22}
465.220	Ne VII	5.7	2176	5.0×10^5	1.93×10^{-19}
186.790	Ni XI	6.1	784	1.32×10^6	9.53×10^{-26}
157.784	Ca XVI	6.5	638	4.94×10^6	1.61×10^{-26}
164.172	Ca XVI	6.5	670	4.91×10^6	6.63×10^{-26}
434.92	Mg VII	5.8	2024	6.3×10^5	2.12×10^{-20}
436.73	Mg VIII	5.9	2033	7.9×10^5	3.12×10^{-20}
439.18	Mg IX	6.0	2045	1.0×10^6	1.81×10^{-21}
368.0713	Mg IX	6.0	1689	1.0×10^6	1.23×10^{-19}
624.9426	Mg X	6.8	2974	6.3×10^6	1.88×10^{-20}
465.220	Ne VII	5.7	2175	5.0×10^5	1.93×10^{-19}

3.3 Raw Data

The Laboratory for Atmospheric and Space Physics (LASP), based at the University of Colarado Boulder, is responsible for creating data files containing raw EVE data from both MEGS-A and MEGS-B. Their website dedicated to the EVE instrument is the source of all the raw data gathered by EVE and also any documentation concerning the files themselves `http://lasp.colorado.edu/home/eve/data/data-access/`. Level 2 data is used throughout this project and they are labeled accordingly:

$$EVS\_L2\_YYYYDDD\_HH\_vvv\_rr.fit$$

where EV designates it is an EVE product and S denotes it is spectrum data, $YYYYDDD$ and HH display the year, Julian date and time of the observation and vvv and rr detail the version and revision numbers, respectively. The FITS files come in hourly blocks and so every hour of data must be downloaded separately. Once the desired files are downloaded the raw data from EVE must be extracted which can be done using pre-written programs in IDL. Dr Paulo J.A. Simões from the University of Glasgow has written a script that includes the recommended, by LASP, eve_read_whole_fits function and kindly provided a copy (Simoes 2015). This script extracts all of the relevant information such as wavelength, time and irradiance all into one easily accessible structure. From this point each of the desired variables mentioned earlier can be extracted from the structure for further analysis. The result of this process is 3 separate arrays of irradiance, time and wavelength the dimensions of which are [5200,360], [360] and [5200], respectively. The first array corresponds to a matrix containing the intensity measurements taken at each of the 5200 wavelengths every 10 seconds in one hour, hence the y dimension of 360. The other two arrays are separate matrices of the time each irradiance measurement is taken and the wavelengths in EUV measured.

Before any spectral analysis can begin the pre-flare has to be subtracted from the data first. In this context the pre-flare is referring to any non-flare spectra which is part of the background emission. The pre-flare is calculated as the average irradiance value over the first 100 EVE measurements before the impulsive phase of the flare. This is calculated for all wavelengths and subtracted from the raw spectra measured by EVE and allows only the flaring irradiance to be seen.

Using the line list in Table 3.1 the evolution of many of the spectral lines can be plotted as their irradiance with respect to time, effectively plotting a light curve. This is done by looking at the intensity values at the pixel location of the line and plotting them with respect to time. This shows how intense particular lines are during the flare and can help pinpoint strong lines to use for analysis. Examples of 18 of these light curves can be seen in Figure 3.1.

One of the first lines chosen for spectral analysis was the Fe XXIII line with a wavelength of 132.9 Å. It was hoped this line could be used as a comparison with the

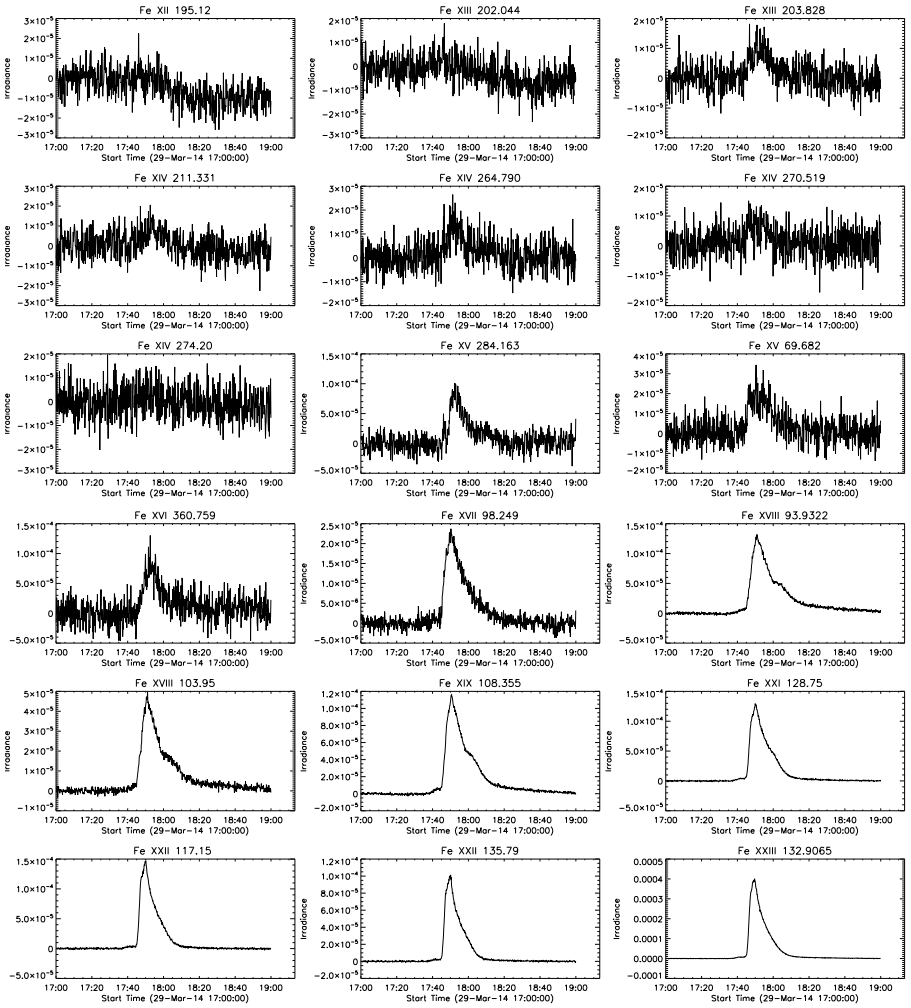

Figure 3.1: "Iron cascade" showing light curves for selected lines from Fe XII to Fe XXIII, covering a temperature from 1.5 million K to 15 million K, during the X1 flare SOL2014-03-29T17:48.

EIS data of an emission line from the same ion but at a wavelength of 263.7 Å. This line was investigated in both flares, however, the flare of SOL2014-03-29T17:48 will be explained in great detail as an example of the processes and steps taken to achieve the results desired.

3.4 Gaussian Fitting

The Fe XXIII 132.9065Å line was chosen as it is a very hot flaring line with a peak formation temperature of approximately 15 million K. It is also very strong during flares and can be seen very easily with EVE. It contains a blend with Fe XX 132.84Å which only shows its contribution during the gradual phase of the flare, this can be seen in Figure 3.4. It is not visible in individual line profiles as Fe XXIII dominates. The light curve of this particular line can be seen in figure below.

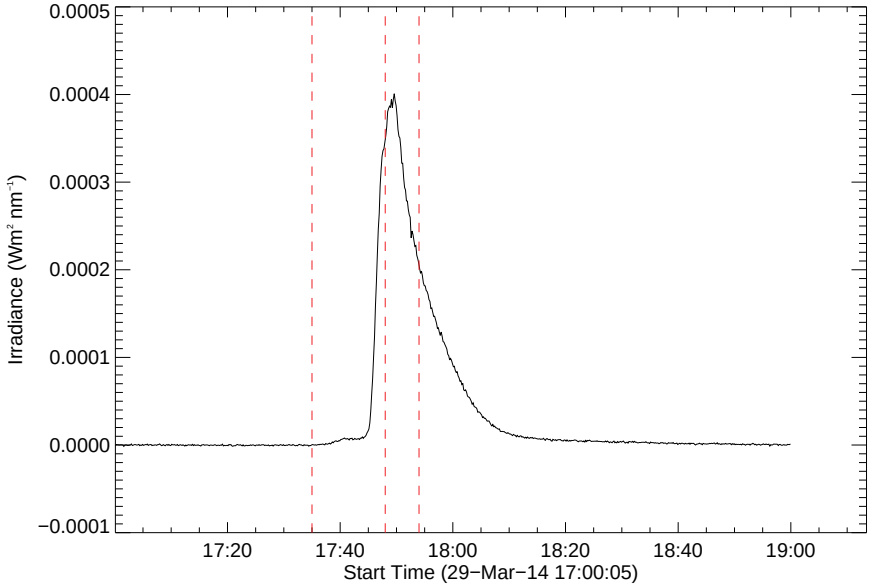

Figure 3.2: The light curve of Fe XXIII 132.9Å, and the GOES start, peak and end times shown as dashed red vertical lines.

A range of 131.3Å and 134.9Å was chosen as the window for the spectral fit, enclosing the Fe XXIII line at 132.9Å. This is a particularly good range as there are no other strong lines within the vicinity of the Fe XXIII/FeXX blend as it dominates during the flare. Using this window a single Gaussian can be fitted to the line profile at every 10 second measurement. The mpfitexpr function in IDL was used to fit the Gaussian with an equation of:

$$G(x) = P_0 + P_1 x + P_2 exp\left(\frac{-(x-a)^2}{2\sigma^2}\right) \tag{3.1}$$

$$P_2 = \frac{1}{\sqrt{2\pi\sigma^2}} \tag{3.2}$$

where σ and a are the standard deviation and centroid wavelength of the data respectively, P_0 and P_1 are the background parameters and P_2 is the peak irradiance. The mpfitexpr function requires 5 inputs in order to provide the fit that is required. These include the x and y data points, starting parameters, error values and the Gaussian function itself, see Equations 3.1 and 3.2 . The starting parameters include approximate values for the background parameters, standard deviation, centroid wavelength and peak intensity to give the function a starting point, allowing it to make the best fit to the data possible.

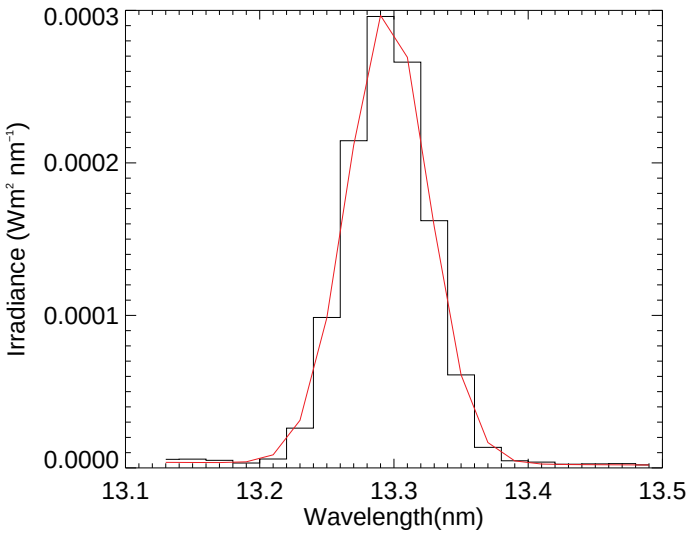

Figure 3.3: An example of the Gaussian fit applied to the line profile of Fe XXIII at a time of 17:47:05, near the peak irradiance of the flare at this wavelength.

Once these values are know the output is given as the best fit Gaussian parameters to the data for every EVE observation along with error estimates for each one. In some cases a double or even triple Gaussian may need to be fitted due to the wavelength

window as there are many lines present. This is very straight forward and easy to do with the mpfitexpr function, however, it is not possible for the Fe XXIII as the Fe XX blend is too close. The main purpose behind this method is to monitor the changing centroid wavelength with respect to time, looking for Doppler shifts in the line centroid as the flare progresses. Once all of the centroid values have been obtained, a position-dependent wavelength correction to the EVE data needs to be applied. This correction is generated due to MEGS-A being off the Rowland circle to increase the spectral resolution (Crotser et al. 2007). In turn a relationship between the spatial position of the source and the measured spectral parameters, such as centroid wavelength, arises. Using this knowledge and data from pre-flight calibrations an expression for this wavelength correction can be described as (Hudson et al. 2011):

$$\Delta\lambda = 0.5\sin\theta + 24.3\sin^2\theta - 1.9\sin\phi + 4.59\sin^2\phi \tag{3.3}$$

where (θ, ϕ) are the heliographic angles of the source and the units are in pm. The location of SOL-2014-03-29T17:48 in arcseconds in the x and y is $510''$ and $260''$, respectively. This can be converted into heliographic angles by using the arcmin2hel function in IDL and then into radians using a simple $\pi/180$ multiplication. By inserting these values into Equation 3.3 we get a correction of 6.23pm which needs to be subtracted from the calculated centroid wavelengths. This correction makes a rather large difference in the stationary component bringing its wavelength equal to that of the CHIANTI rest wavelength. This applied correction can be seen in Figure 3.4.

Figure 3.4 shows the result of the Gaussian fitting and the changing centroid wavelength of the Fe XXIII line profile with respect to time. There are a few key observations to be made with this plot. Firstly, there is a large scatter of points before the impulsive phase at 17:45. This is due to weak Fe XXIII emission before the impulsive phase, and there is little to none during the pre-flare stage. This in turn means that the Gaussian is fitting very noisy data, and the centroid values have large errors. Secondly, during the impulsive phase there is a clear blueshifted component which is what is expected during a flare, occurring as the plasma is thrown out into the corona by the release

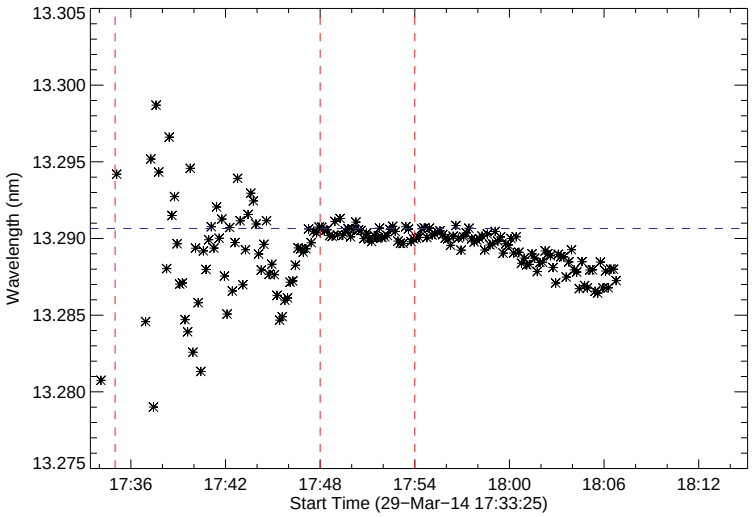

Figure 3.4: The changing centroid wavelength of the Fe XXIII 132.9Å line fit with respect to time as the flare SOL-2014-03-29T17:48 progresses. The dashed blue horizontal line represents the CHIANTI wavelength for Fe XXIII at 132.9065Å, and in this case is the effective rest wavelength. The dashed red vertical lines represent the GOES start, peak and end times for the flare.

of magnetic energy in the form of kinetic and thermal energy. After the impulsive phase and during the beginning of the gradual phase there is a stationary component observed. This stationary component arises from the build up of plasma flowing into the corona from the chromosphere and collecting at coronal heights in the atmosphere and is present throughout the flare (Kane 1983). Finally, towards the end of the gradual phase a secondary blueshift appears due to the previously mentioned strong blend with the Fe XX 132.84Å line.Del Zanna & Woods (2013) discuss this blend in more detail as during the gradual phase decline of the flare the contribution of Fe XX to the blend increases when Fe XXIII decreases and in so produces this apparent secondary blueshift. However, another explanation for this secondary blueshift is that due to EVE being a full Sun spectrometer there is a possibility of other flares on the Sun's disk causing this effect.

3.5 Doppler Velocities

Now that the centroid wavelengths have been obtained we can use them to calculate the corresponding Doppler velocities. This is achieved using the same method described in Chapter 2 using Equations 2.1 and 2.2. By calculating these Doppler velocities for every EVE measurement a plot similar to Figure 3.4 is produced but with reference to velocity instead of wavelength.

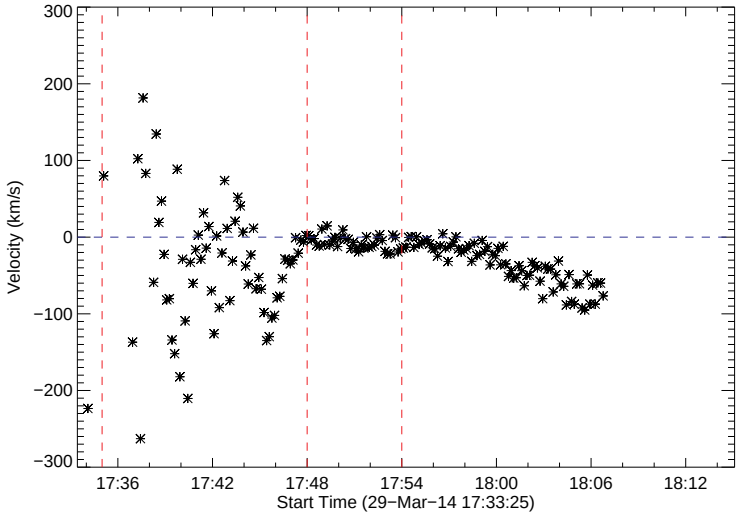

Figure 3.5: A plot showing the corresponding Doppler velocities of the obtained Doppler shifts in centroid wavelength from the Gaussian fits. The dashed blue horizontal line represents zero velocity signifying a stationary component and the dashed red vertical lines represent the GOES start, peak and end times for the flare.

3.6 Error Analysis

As mentioned in Section 3.4 the IDL function mpfitexpr requires error values on the irradiance of individual points. These were calculated as the standard deviation of the first 20 EVE measurements before the impulsive phase of the flare. They were

then input into mpfitexpr and used by the function to generate error values on the parameters of the Gaussian fit. The errors of particular interest are the values on the centroid wavelengths as these can be used to calculate a corresponding error on the Doppler velocity. The propagation of errors is calculated using partial derivatives in the usual fashion.

$$\sigma_y = \sigma_x . \frac{\partial x}{\partial y} \tag{3.4}$$

where σ_y and σ_x is the error on the x and y data respectively. When the above is applied to Equation 2.1 an expression to describe the error on velocity with respect to the error on the observed wavelength is derived.

$$\sigma_v = \sigma_{\Delta\lambda} . \frac{c}{\lambda_{rest}} \tag{3.5}$$

where σ_v is the error on the velocity and $\sigma_{\Delta\lambda}$ is the error on the observed wavelength and the rest wavelength combined. However, we assume the error on the rest wavelength, which was obtained from the CHIANTI database, is negligible and so does not contribute to the error on $\Delta\lambda$. With this now in place error values can be calculated for all Doppler velocities measured with EVE.

As can be seen from Figure 3.6 the errors dramatically decrease in size during the impulsive phase. During the pre-flare there is little Fe XXIII or Fe XX emission and so no Gaussian for the function to fit. This in turn produces large errors on velocity values making them unreliable. In the course of the impulsive phase, however, the error bars are significantly smaller and in the range of approximately 1-5 km/s as the line profile displays a very strong and pronounced Gaussian peak. As the flare progresses further into the gradual phase the errors begin to grow again as the Fe XXIII emission weakens causing the fits to decrease in reliability.

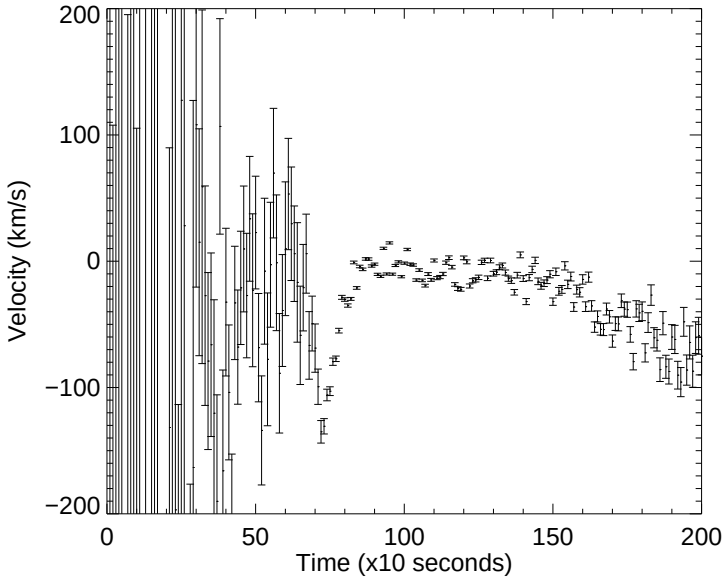

Figure 3.6: The error values on the Doppler velocities are shown as error bars on each measurement. These were calculated using Equation 3.5 with wavelength error values obtained from the Gaussian fit.

3.7 Results

3.7.1 SOL2014-03-29T17:48

The event of SOL2014-03-29T17:48 was an X1.0 class flare which occurred near the western limb of the Sun at a location of x = 510″, y = 260″. The GOES start, peak and end times for this flare are 17:35, 17:48 and 17:54 respectively. It was a well observed and bright event and due to this many EVE lines were investigated for this particular flare.

3.7.1.1 O VI 184.12Å

This particular line was investigated with the hopes of being used as a comparison for cooler lines in EIS data. However, the line profile of this line was very noisy and cluttered with other emission lines. These blends include another O VI line at 183.9372Å and two iron lines Fe XI 184.793Å and Fe VIII 185.2133Å. Figure 3.7 shows

the 4 lines at one instance during the solar flare where each line is relatively clear and can be extracted easily. However, this is not the case for every EVE measurement as some of the time, the lines are very blended and cannot be de-blended easily: an example of this case can be seen in Figure 3.8. This is primarily due to the low spectral resolution of EVE as it is only able to resolve spectral lines at 0.1 nm. Unfortunately, due to the blends in this particular O VI line it was deemed unusable for the purposes of this project. However, other O VI lines were investigated and can be seen in more detail further on in this section.

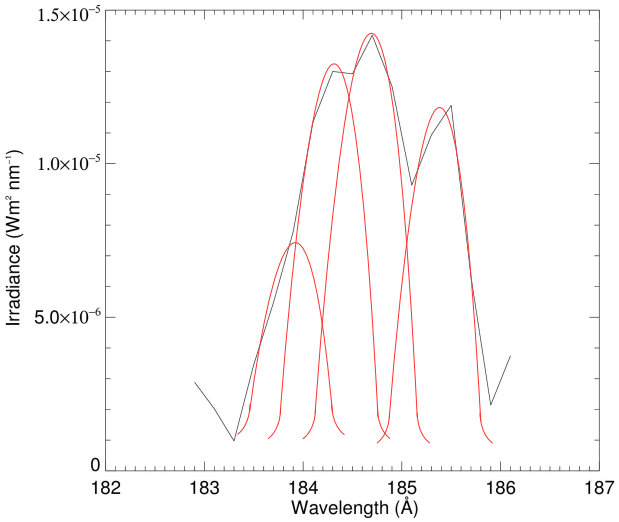

Figure 3.7: An example of a good line profile for the wavelength window containing the O VI line. This complex profile includes O VI 183.94Å, O VI 184.12Å, Fe XI 184.79Å and Fe VIII 185.21Å from left to right.

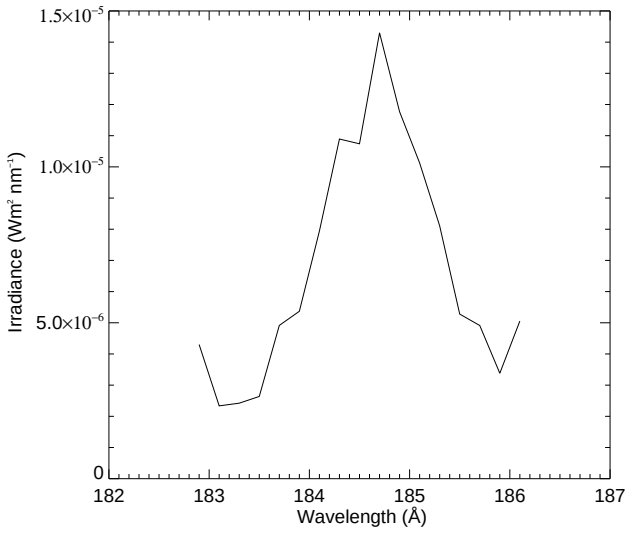

Figure 3.8: An example of the wavelength window containing O VI 184.12Å showing how badly blended the surrounding lines becoming as the flare progresses, making it impossible to distinguish and isolate the O VI line.

3.7.1.2 He II 303.783Å

He II 303.78Å is a very strong emission line in the EVE spectrum with a peak temperature of around 90,000 Kelvin. It has a relatively strong light curve with some noise appearing throughout. This can be seen below in Figure 3.9. This particular He II line is also a self-blend with another He II line 303.786Å. There are also many O III lines and a few Fe lines contained within the fitting window of 301.7Å and 305.7Å, however, theoretically they have a considerably lower intensity in comparison to the He II lines which dominate.

Using the same process as described in Section 3.4 the centroid wavelength of the emission line was measured during the course of the flare. These measurements could then be used to calculate Doppler velocities corresponding to the change in wavelength with respect to the CHIANTI rest wavelength of the emission line. These velocities were calculated using Equations 2.1 and 2.2 with the same method as described in Section 3.5. The results of this were a similar plot to Figure 3.5 and this can be seen

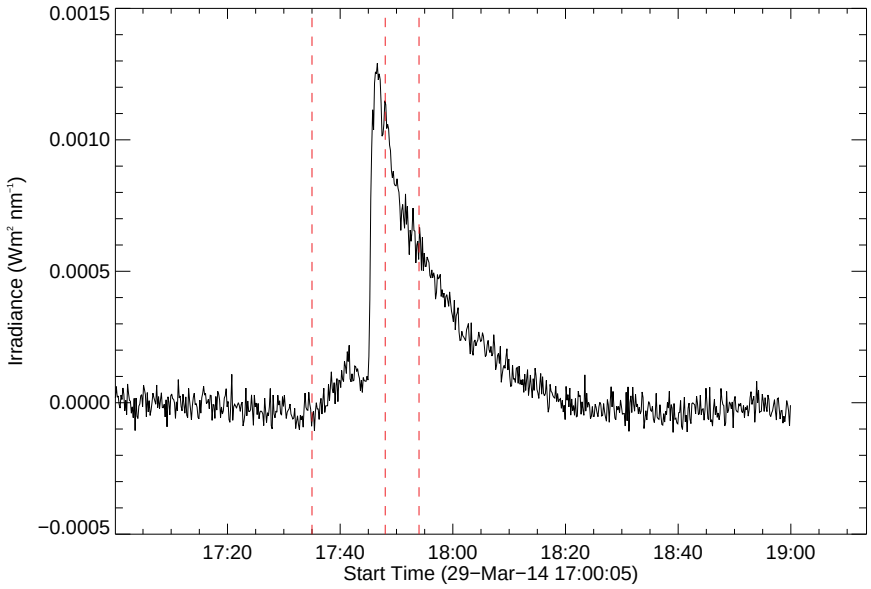

Figure 3.9: This plot shows the changing irradiance of He II 303.783Å with respect to time during the SOL-2014-03-29T17:48 event. The dashed red vertical lines represent the GOES start, peak and end times for the flare.

below in Figure 3.10. Errors were also calculated for these Doppler velocities using the method described in Section 3.6 and can also be seen in Figure 3.10.

From Figure 3.10 a small blueshift can be observed at 17:45:30 which corresponds to a maximum Doppler velocity of approximately -62km/s ± 5km/s.

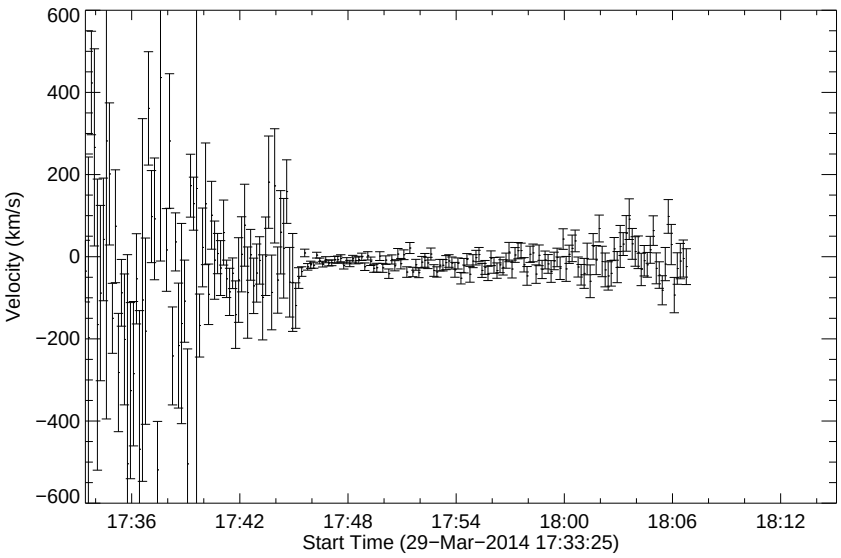

Figure 3.10: The Doppler velocity of He II 303.783Å plotted with respect to time. Error values have also been represented as error bars on the plot showing the goodness of the Gaussain fit during the flare.

3.7.1.3 Fe XIII 203.83Å

Due to one of the EIS core lines being Fe XII 195.12Å a comparable EVE line had to be identified with a similar peak temperature, to allow a feasible comparison. Many options were investigated including Fe XII 195.12Å itself and Fe XIII. Fe XII 195.12Å showed little-to-no peak in the light curve during the flare. This was attributed to the way EVE takes the spectrum data and how it observes the Sun. Fe XII is a very common line that is emitted through the whole of the Sun's atmosphere and so, as EVE observes the Sun as a star the emission originates from across the whole disk. This could potentially 'wash out' the flare emission of Fe XII causing the flaring emission to be indistinguishable. Pre-flare subtractions were carried out on all data and a cascade of iron lines at similar temperatures to Fe XII can be seen in Figure 3.1. From these plots you can see the light curve of Fe XII shows no increased irradiance during the flare, however, a small dimming is noticed after the flare. This is likely the result of

coronal dimming which happens when part of the corona is ejected in a CME (Mason et al. 2014). Therefore, Fe XIII 203.83Å was selected as an alternative to Fe XII as it has a similar peak formation temperature and its light curve showed a significant increase in irradiance during the flare (Figure 3.11).

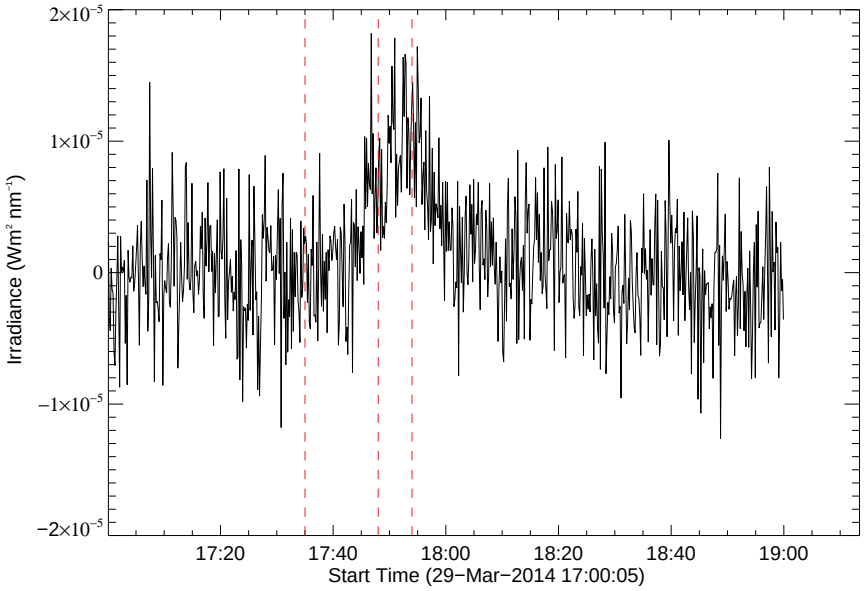

Figure 3.11: A plot of changing irradiance of Fe XIII 203.83Å with respect to time during the flare SOL-2014-03-29T17:48. The dashed red vertical lines represent the GOES start, peak and end times for the flare.

However, despite the promise showed by the light curve of this line the line profiles were inadequate for Gaussian fitting as they were very noisy and extremely blended. In fact, the wavelength window used to attempt the Gaussian fitting contained approximately five other iron emission lines with similar intensities to Fe XIII. Due to this the Fe XIII had to be abandoned as a potential replacement for Fe XII as it was impossible to attempt to de-blend this window due to the low spectral resolution of EVE. After this realisation an attempt was made to use Fe X 184.54Å as a replacement for Fe XII, however, similar problems arose with the line profiles of this line also. Unfortunately, therefore, there is no EVE line for which velocities can be success fully compared to

EIS Fe XII.

3.7.1.4 Fe XXIII 132.9Å

This particular line was used throughout this chapter to detail the steps taken in the analysis of the EVE spectral data. From the plot in Figure 3.5 you can see a clear blueshifted component during the impulsive phase of the flare with a maximum Doppler velocity of approximately 135km/s ± 1km/s.

3.7.2 SOL2011-02-16T07:35

The event of SOL2011-02-16T07:35 was a C5.4 class flare which occurred on the western hemisphere of the Sun at a location of x = 432″, y = -250″. This flare was selected due to there being EIS and EVE data available during the flare. EVE also measured this flare using both MEGS-A and MEGS-B spectrometers providing a much fuller EVE spectrum for analysis. The GOES start, peak and end times for this flare are 07:35, 07:44 and 07:55 respectively.

3.7.2.1 Fe XXIII 132.9Å

One of the first lines to be looked at was the Fe XXIII line which appears often due to its strong irradiance during flares and well-isolated emission line in the wavelength window during Gaussian fitting. On this occasion the line is not as intense as the March 2014 line as this is a much smaller flare being in the C class range, however, it still provided similar results that were expected. Following through the same processes as discussed in Sections 3.4 and 3.5, centroid wavelengths were taken from Gaussian parameters of fits to every 10 second measurement. Figure 3.12 shows these centroid wavelengths as individual points on the plot.

From these values corresponding Doppler velocities can be calculated using Equations 2.2 and 2.1. By doing so the following plot in Figure 3.13 is produced and error values have also been added, calculated using the method described in Section 3.5. Similar observations can be made from this figure as were made with Figure 3.5. This

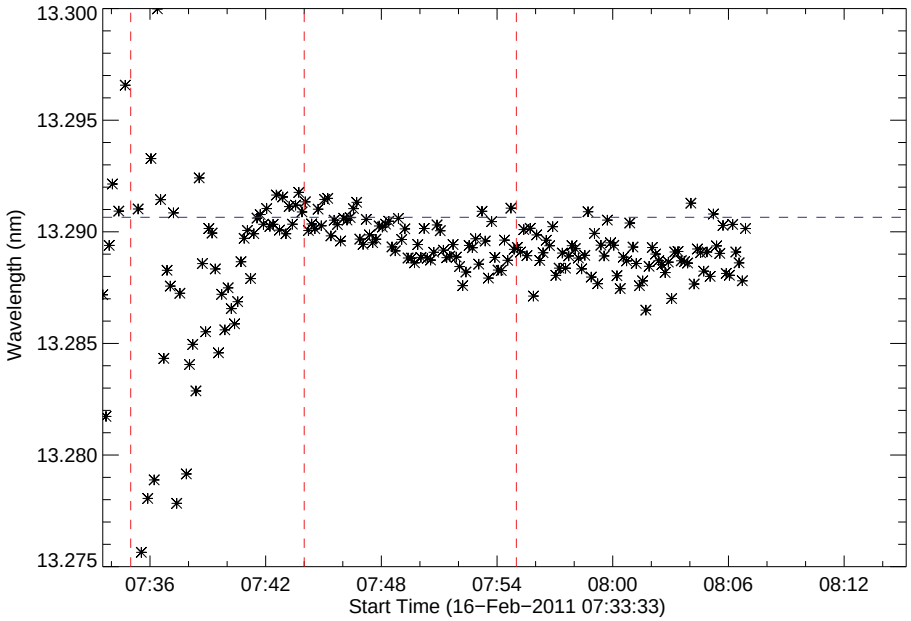

Figure 3.12: A plot of the centroid wavelength of Fe XXIII 132.9Å as it changes with respect to time during the flare SOL-2011-02-16T07:35. The dashed red vertical lines represent the GOES start, peak and end times for the flare.

includes a blueshifted component during the impulsive phase and a stationary component during the beginning of the gradual phase. In comparison with Figure 3.6, Figure 3.13 is a little more complex in its structure and does not have such a clearly defined blueshift. This is primarily due to the strength of this flare as it is only a C class and also due to it having two peaks, where there is a second outburst of energy from the flaring region. This phenomenon can also be seen in Figure 3.12 as the Doppler velocity becomes slightly redshifted during the gradual phase before leveling off again to a stationary component. However, the initial blueshift approximates to a maximum velocity of 87km/s ± 5km/s.

3.7.3 SOL2011-07-30T02:12

The event of SOL2011-07-30T02:12 was an M9.3 class flare which occurred on the eastern side of the Sun at a location of x = -519″, y = 184″. The GOES start, peak

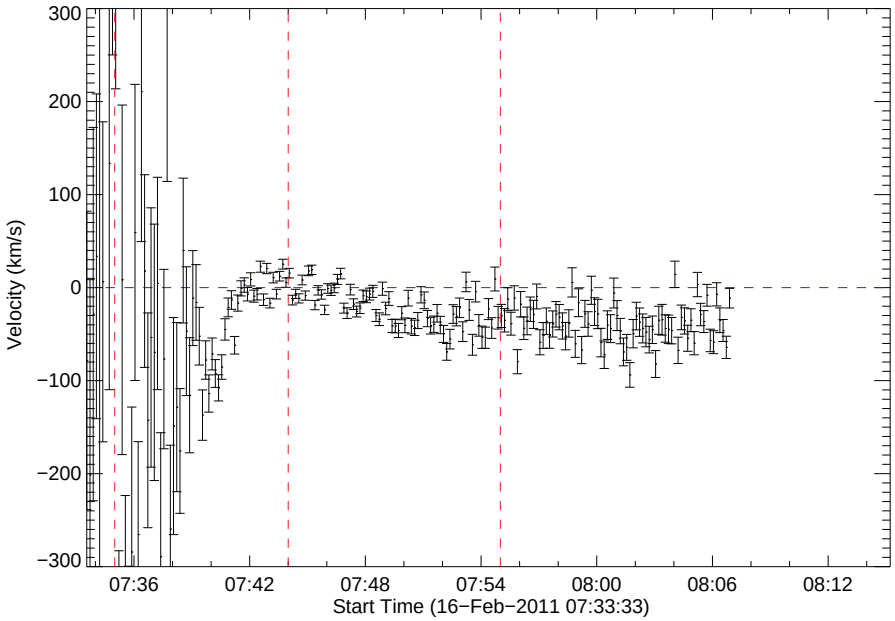

Figure 3.13: A plot of the Doppler velocities of Fe XXIII 132.9Å as they change with respect to time during the flare SOL-2011-02-16T07:35. These Doppler velocities along with corresponding errors were calculated using the centroid wavelengths obtained from the Gaussian fits. The dashed blue horizontal line represents zero velocity signifying a stationary component and the dashed red vertical lines represent the GOES start, peak and end times for the flare.

and end times of this flare are 02:04, 02:09 and 02:12 respectively. This flare was investigated as MEGS-B data was taken during the flare allowing analysis of other cooler emission lines. These other emission lines were examined with the hope of being used to compare to some EIS data. However, this particular flare was not observed by EIS and so this comparison could not be made. Despite this it was a useful exercise to examine these cooler lines.

3.7.3.1 O VI 1032Å

The methods mentioned in previous Sections (3.7.1.2 and 3.7.2.1) were used to calculate centroid wavelengths of the line profiles and in turn their corresponding Doppler velocities. O VI 1032Å contains no blends and is a relatively isolated line in the

selected wavelength window, 1029.9Å and 1033.1Å, with only two other S II lines present. The MEGS-B instrument has a slightly different design to the MEGS-A and so a position-dependent wavelength correction is not needed. Figure 3.14 shows these Doppler velocities and how they vary as a function of time during the flare of 30th July 2007.

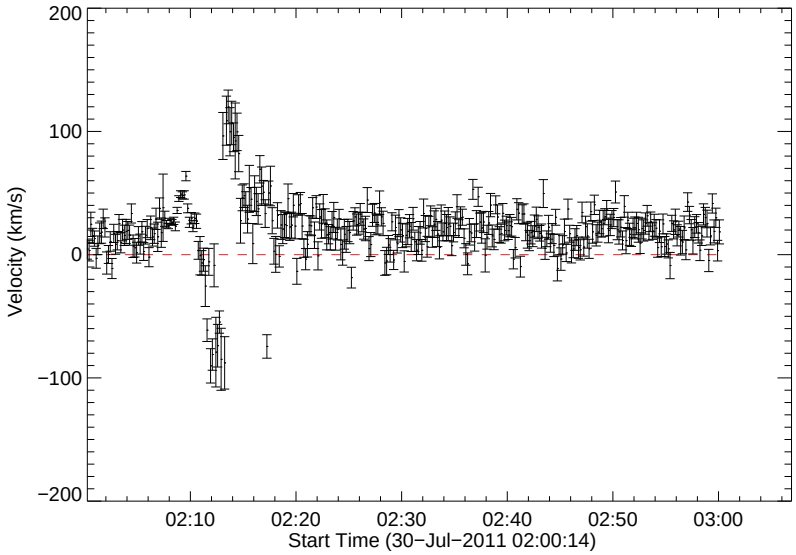

Figure 3.14: The Doppler velocity of O VI 1032Å is plotted with respect to time showing a blueshifted component during the impulsive phase and a stationary component during the gradual phase. Error values are also represented as error bars on this plot.

From the plot one can see a clear blueshift during the impulse phase of the flare, followed closely by a similarly stray redshift and then a stationary component during the gradual phase. This blueshift corresponds to a maximum Doppler velocity of -90.23km/s ± 13.94km/s. Before the flare the velocity of the O VI emission is not zero and this continues as the gradual phase progresses and the active region settles. This could be due to the two S II lines present in the fitting window which form at lower temperature of around 32,000K. This could plausibly be seen during the pre-flare stage

of the flare. There is also a strong redshift present after the peak of the flare. This could be a result of the O VI emitting plasma cooling and falling down to the surface of the Sun. However, as it possesses a similar magnitude to that of the blueshift it is more likely to be caused by mass downflows along the loop structure at the active region.

3.7.3.2 Mg X 609.7Å

Similarly this process was repeated for Mg X 609.7Å line as measured by MEGS-B giving the plot of Doppler velocity as it varies with time, with a trend akin to the one of Figure 3.14.

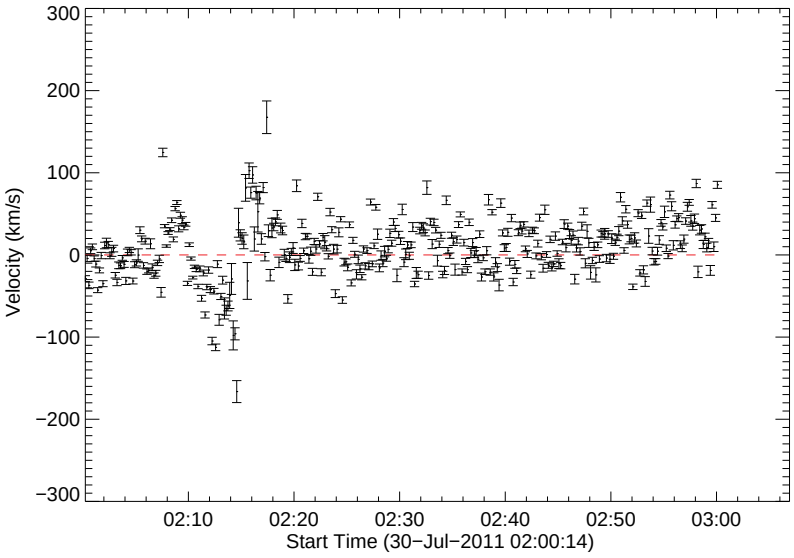

Figure 3.15: The Doppler velocity of Mg X 609.7Å is plotted here with respect to time, showing how it varies during the flare of SOL2011-07-30T02:12. Error values have also been displayed.

From the plot one can see a clear blueshift during the impulsive phase which corresponds to a Doppler velocity of -97.95km/s ± 17.67km/s. This is followed by a rapid redshift and then a stationary component during the gradual phase which is constant

throughout the rest of the emission.

3.8 Conclusion

This chapter has taken a close look at Doppler velocities in several EVE emission lines. Plots of Doppler velocity against time were produced for a few emission lines including Fe XXIII. These showed strong evidence for a large blueshifted component before the peak of the flare, followed by a stationary component during the gradual phase. This is in agreement with what is expected behaviour for hot plasma flows during a particularly large event, especially in a hot flaring line such as Fe XXIII. Both events exhibited this behaviour in Fe XXIII and in other lines such as He II and O VI. A number of other EVE lines were studied in the hope of finding some that could be used in a direct comparison with EIS observations, however, due to the difficulties of unresolved blends and low flare irradiance, in the end Fe XXIII was the only suitable common line in these two flares. The plots from Fe XIII will be used in a direct comparison with EIS data in Chapter 4.

Chapter 4

Comparing the Data

4.1 Introduction

One of the key aims of this research project was to combine and compare results obtained with data sets from two instruments Hinode/EIS and SDO/EVE. This has proven to be challenging due to the way in which both of these instruments make their observations because EIS takes high-resolution spatially resolved EUV measurements whereas, EVE takes observations of EUV irradiance with high temporal cadence. EVE, a normal incidence spectrograph, takes its measurements of the whole disk of the Sun all day everyday but, flare enhancements can be hard to detect in lines with formation temperatures of approximately 1MK. Unresolved blends at these temperatures make velocity measurements hard to perform in these cooler lines where enhancements are seen. Until May 2014 MEGS-A was always looking at the Sun taking measurements constantly and MEGS-B was set to observe three hours each day and five minutes each hour, however, now MEGS-A is out of commission and MEGS-B is always taking measurements. EIS is a slit rastering spectrometer that only makes observations of small areas of the Sun's disk decided upon by a team of scientists and engineers. It is not guaranteed if EIS will be observing an area in which a flare will happen, however, a lot of the observations are made in or around active regions increasing the chances of these events being captured. With this information in mind it is no wonder the

challenge of comparing these instruments is a great one, nonetheless two methods of doing so were implemented and are discussed in great detail here.

4.2 Synthetic Velocity and Intensity Maps

EIS rasters, taken every few minutes, provide a view of a flare in which spatial and temporal evolution are only intermittently sampled. This is difficult to compare with EVE observations which provide a spatially averaged view, every 10 seconds. To make EIS and EVE data more comparable we will generate synthetic velocity maps, by interpolating EIS data in time, pixel by pixel.

4.2.1 Polynomial Fitting

Firstly, the high intensity flaring pixels from EIS rasters were extracted through the poly_val function in IDL. This function allowed a polygon to be drawn around the desired area and all values contained within to be extracted into one long array (Figure 4.1).

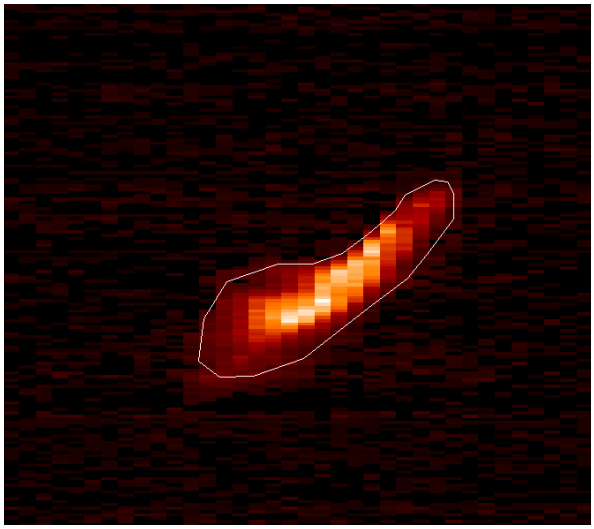

Figure 4.1: An image showing the area selected by the poly_val function for the 07:50:14 raster from the SOL2011-02-16T07:35 event.

This was used because the high intensity flaring pixels could be isolated and extracted leaving behind the pixels which showed little or no emission and contained mainly noise. This function was used for all EIS rasters in both velocity and intensity where the area selected depended on where the high intensity pixels were in the raster.

After poly_val has been used it stores information of the polygon such as the position of the values in the original array and the x and y coordinates of the polygon itself. This then allows the same polygon to extract the same area of information from all the rasters and also to obtain the time at which all measurements were taken. The end result is separate long arrays of time, intensity and velocity for each raster. Once all of this data has been obtained it can be used to monitor the changing intensity and velocity of each pixel with respect to time. The aim for plotting the data in this way is to interpolate by fitting polynomial curves to the data, effectively providing intensity and velocity values for the selected pixels at any time in the course of the EIS rasters.

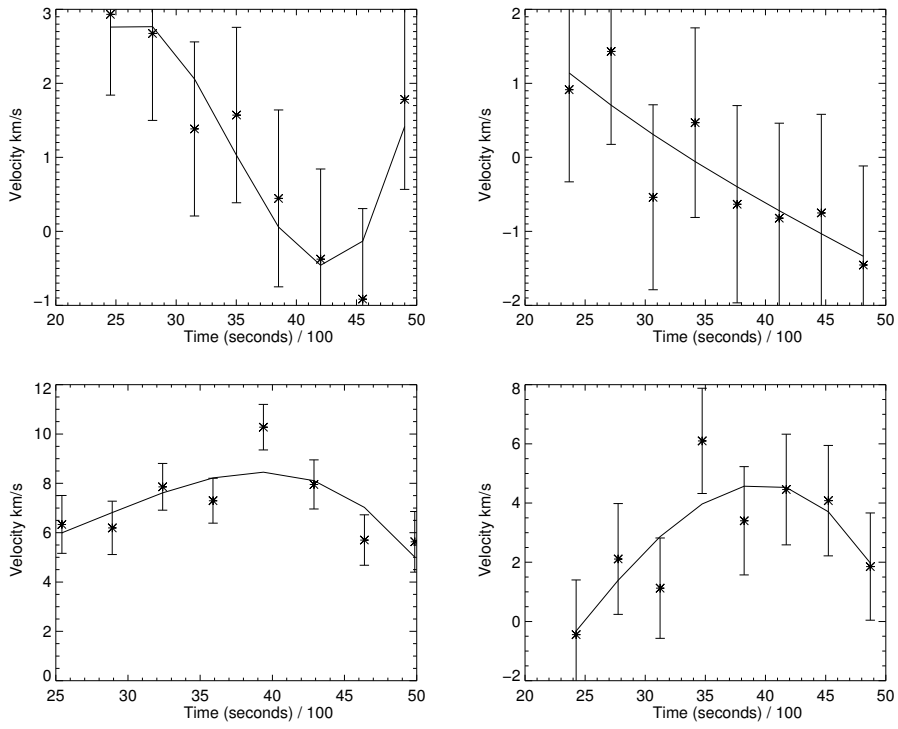

Figure 4.2: These four velocity-time plots show the polynomial fits obtained for four different pixels from one of the EIS rasters.

To prepare the EIS data for interpolation the function anytim was used to convert the timestamp for each slit position into seconds, subtracting the number of seconds elapsed since the start of the observations to bring them into a range that can be managed by the interpolating polynomial fit function. A simple program can be written and used to reverse this process if particular times need to be known.

Now, a plot of velocity against time for each individual pixel can be made and a corresponding polynomial fit applied to each case. Several degree polynomials were tested and a 3rd degree polynomial was selected as having the best fit trend to the data intersecting the majority of the error bars. Examples of this can be seen in Figure 4.2 where a 3rd degree polynomial was fitted to the data. This can be repeated fitting polynomials to every pixel then building up a plot of up to 800 different polynomials fits. From this it is possible to calculate 'synthetic' interpolated velocity values for each pixel under the assumption the velocity evolution is smooth, creating an image of what the velocity map would look like at any given time. This can also be repeated for the intensity values as well. Figures 4.3 and 4.4 show all of the smoothed polynomial curves fitted for 830 different pixels in EIS rasters for the SOL2014-03-29T17:48 event for velocity and intensity values of Fe XVII. In these figures each line represents an individual interpolated polynomial fit for intensity, in Figure 4.3, and velocity, in Figure 4.4. In Figure 4.3 negative values can be seen which are unphysical for an intensity. These values occur as a result of the polynomial fit not being valid outwidth the EIS observation times. This is the same case for velocities in Figure 4.4 which extend outwidth -200km/s $\leq v \geq$ 200km/s. These plots were provided as they show the range of values for intensity and velocity in the EIS rasters during the flare.

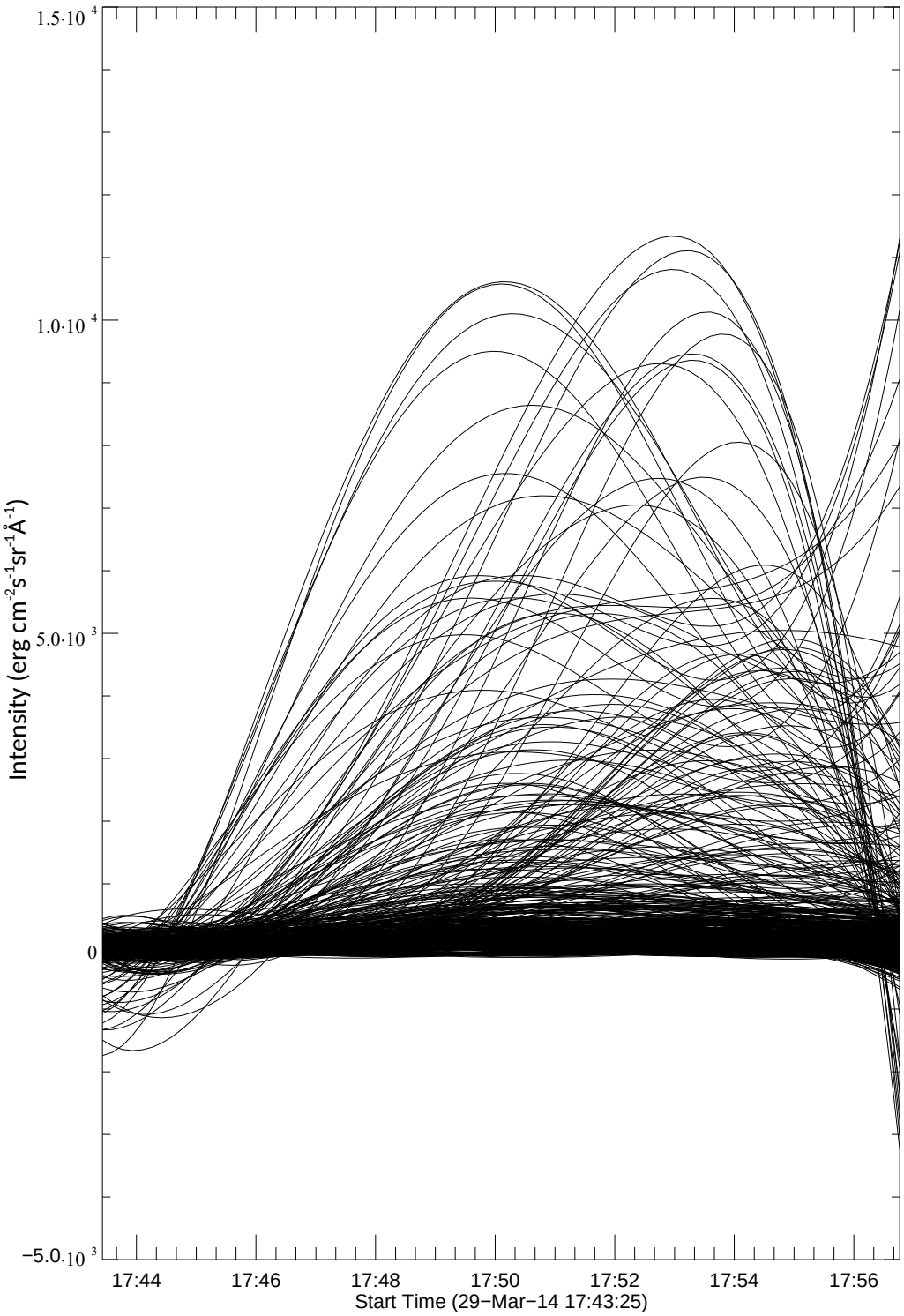

Figure 4.3: This is a plot of all polynomial fits of intensity acquired for Fe XVII data from the 2014-03-29T17:48 event.

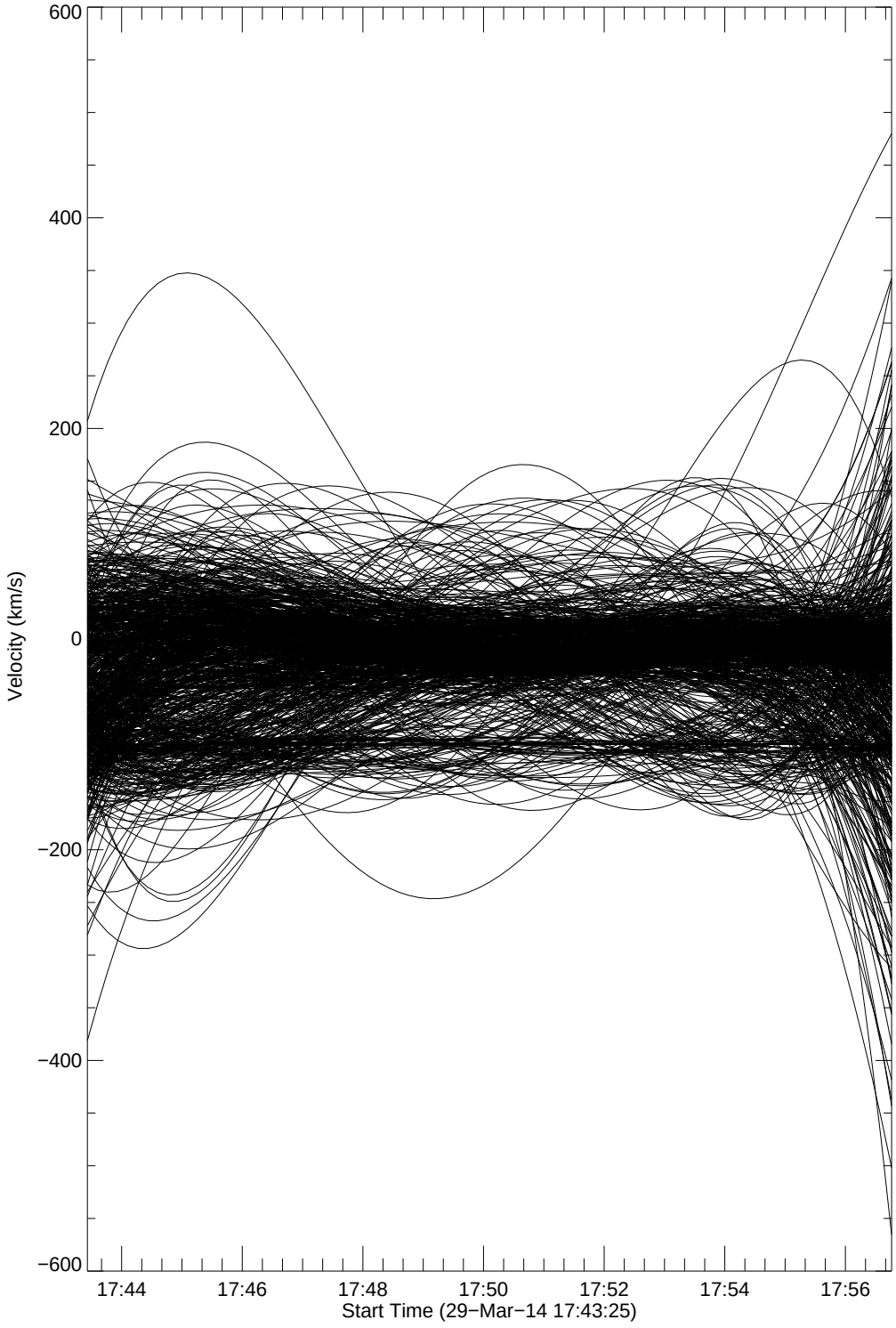

Figure 4.4: This is a plot of all polynomial fits of velocity acquired for Fe XVII data from the 2014-03-29T17:48 event.

4.2.2 Creating Synthetic Maps

Using Figures 4.3 and 4.4, values for velocity and intensity of every pixel at any given time during 17:41:14 and 17:55:09 can be obtained. When extracting the pixels from the original rasters using poly_val they are placed into long arrays losing their positional information with respect to the original EIS raster. However, this is stored inside a new array and is needed now when placing the pixels back into the EIS raster this process requires several steps. The first step is to identify the x and y coordinates of each point in the long arrays, achieved by using array_indices which uses the positional array obtained from poly_val. The coordinates are stored in a separate array and used by a series of FOR loops to populate a new array with the intensity and velocity values. This in turn produces two new maps made up from intensity and velocity values generated through an interpolation method. Examples of the synthetic maps can be seen in Section 4.2.3 where they are compared to the real EIS rasters.

4.2.3 Results

This section presents the 'synthetic' interpolated velocity maps for several different emission lines of varying temperatures. Various times were selected and 'synthetic' maps were created, showing how they compare to the original EIS rasters. The 'synthetic' rasters created were chosen as they fall between when the real rasters were taken by EIS. This gives an indication into what is happening at the active region during these times. It is clear in the 'synthetic' intensity maps that the emission of the lines Fe XII, Fe XVII and Fe XXIII in comparison with the real maps have the same progression during the flare. The movement of the plasma in the 'synthetic' intensity maps, matches up with what can be seen in the real maps. As for the velocities they also show the same result. This is very positive as it means the polynomial fitting method is reliable in filling the gaps when EIS is not observing, providing 'synthetic' data to compare with EVE.

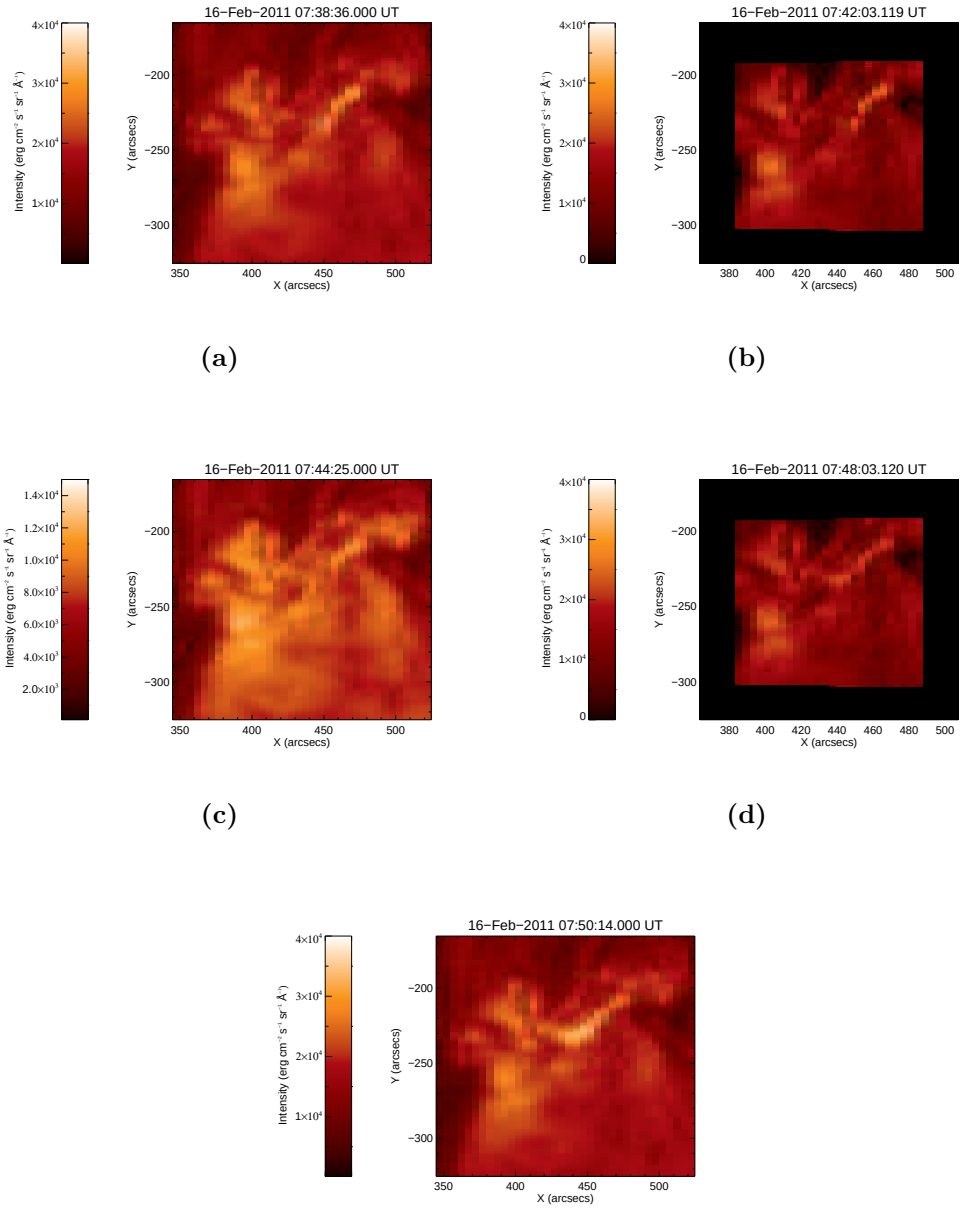

Figure 4.5: Intensity Maps (a) - (e) show the changing intensity of Fe XII 195.12Å at the observed active region during the SOL2011-02-16T07:35 event, as seen by EIS with respect to time. Maps (b) and (d) are synthetic intensity maps produced by the method discussed in Section 4.2, all other maps are from real EIS data.

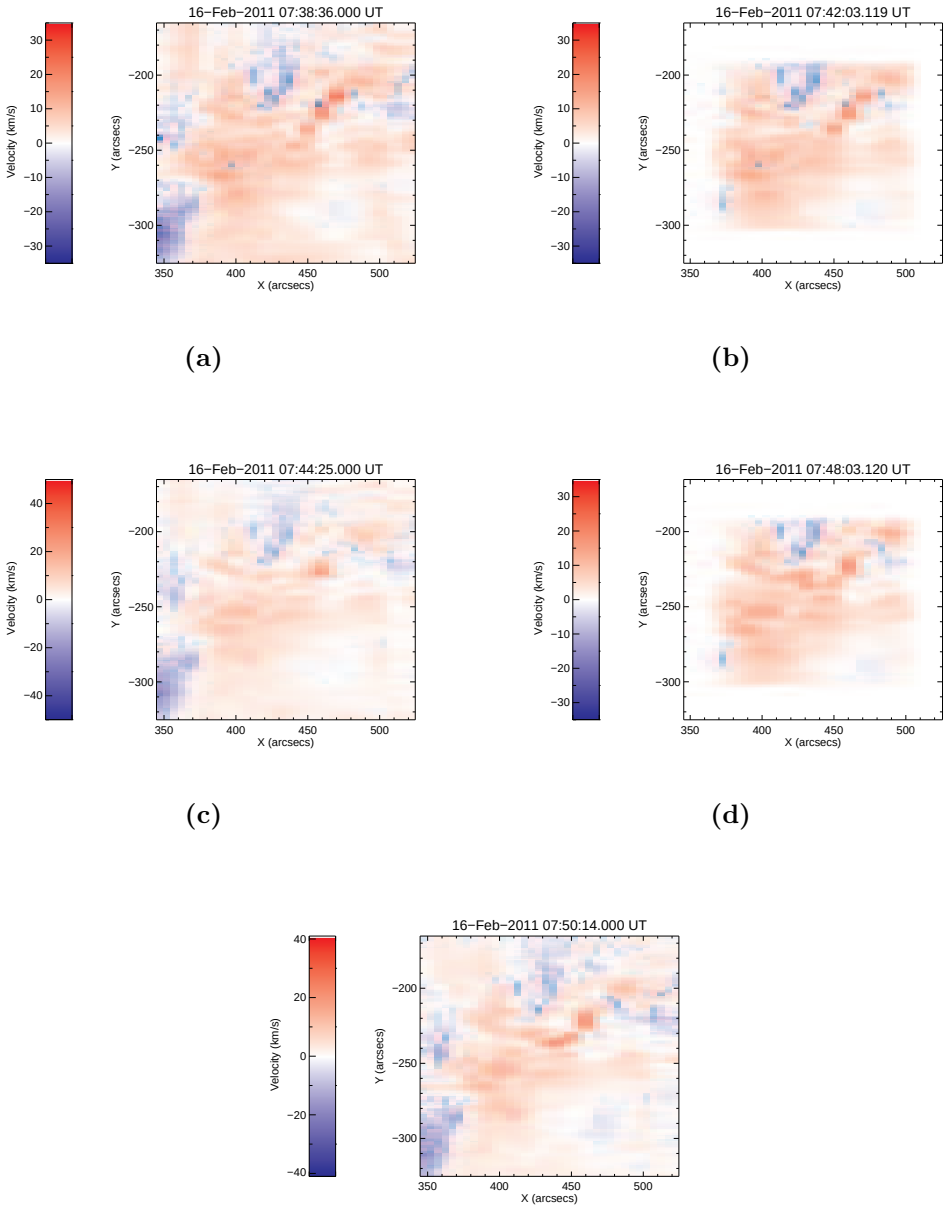

Figure 4.6: Velocity Maps (a) - (e) show the changing Doppler velocity of Fe XII 195.12Å at the observed active region during the SOL2011-02-16T07:35 event, as seen by EIS with respect to time. Maps (b) and (d) are synthetic velocity maps produced by the method discussed in Section 4.2, all other maps are from real EIS data.

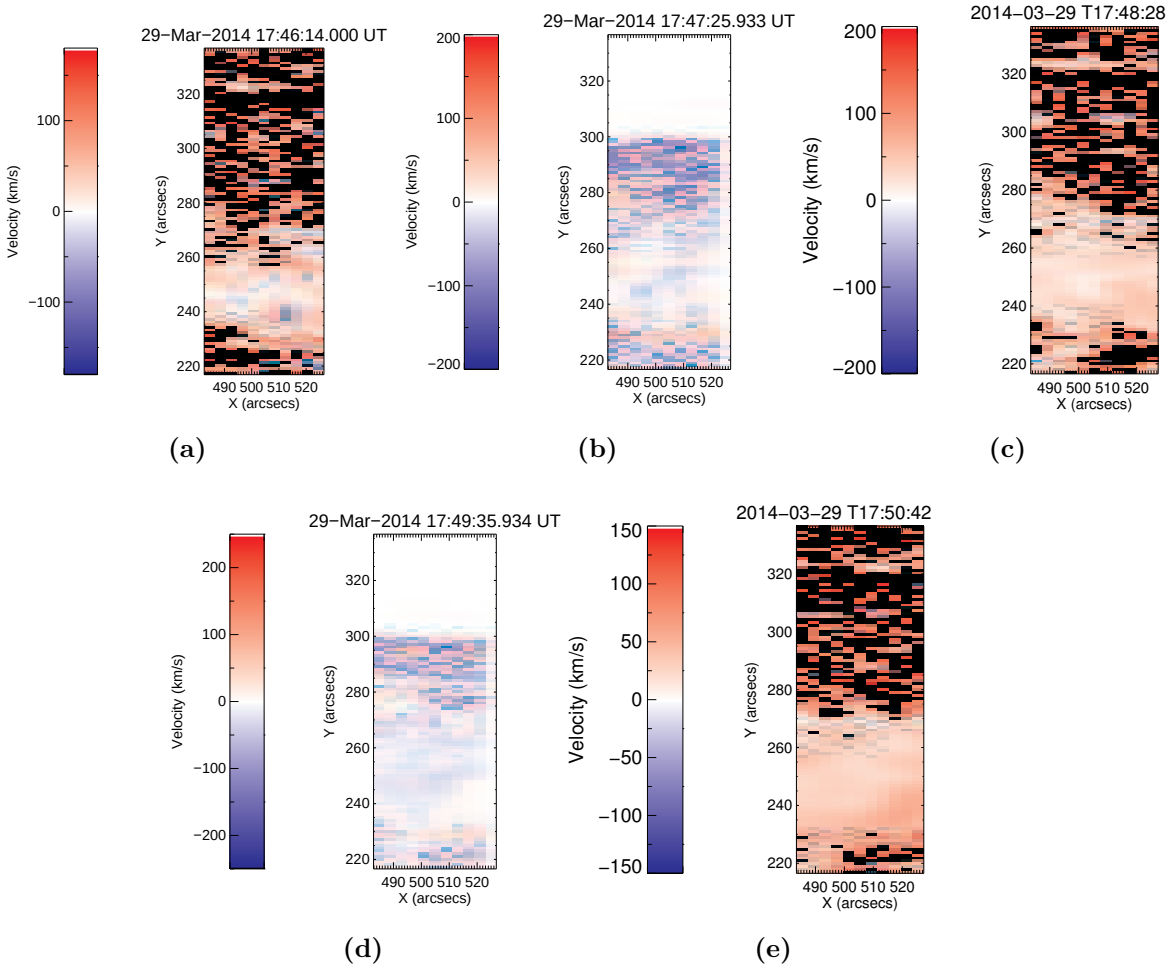

Figure 4.7: Velocity Maps (a) - (e) show the changing intensity of Fe XVII 269.42Å at the observed active region during the SOL2014-03-29T17:48 event, as seen by EIS with respect to time. Maps (b) and (d) are synthetic Doppler velocity maps produced by the method discussed in Section 4.2, all other maps are from real EIS data.

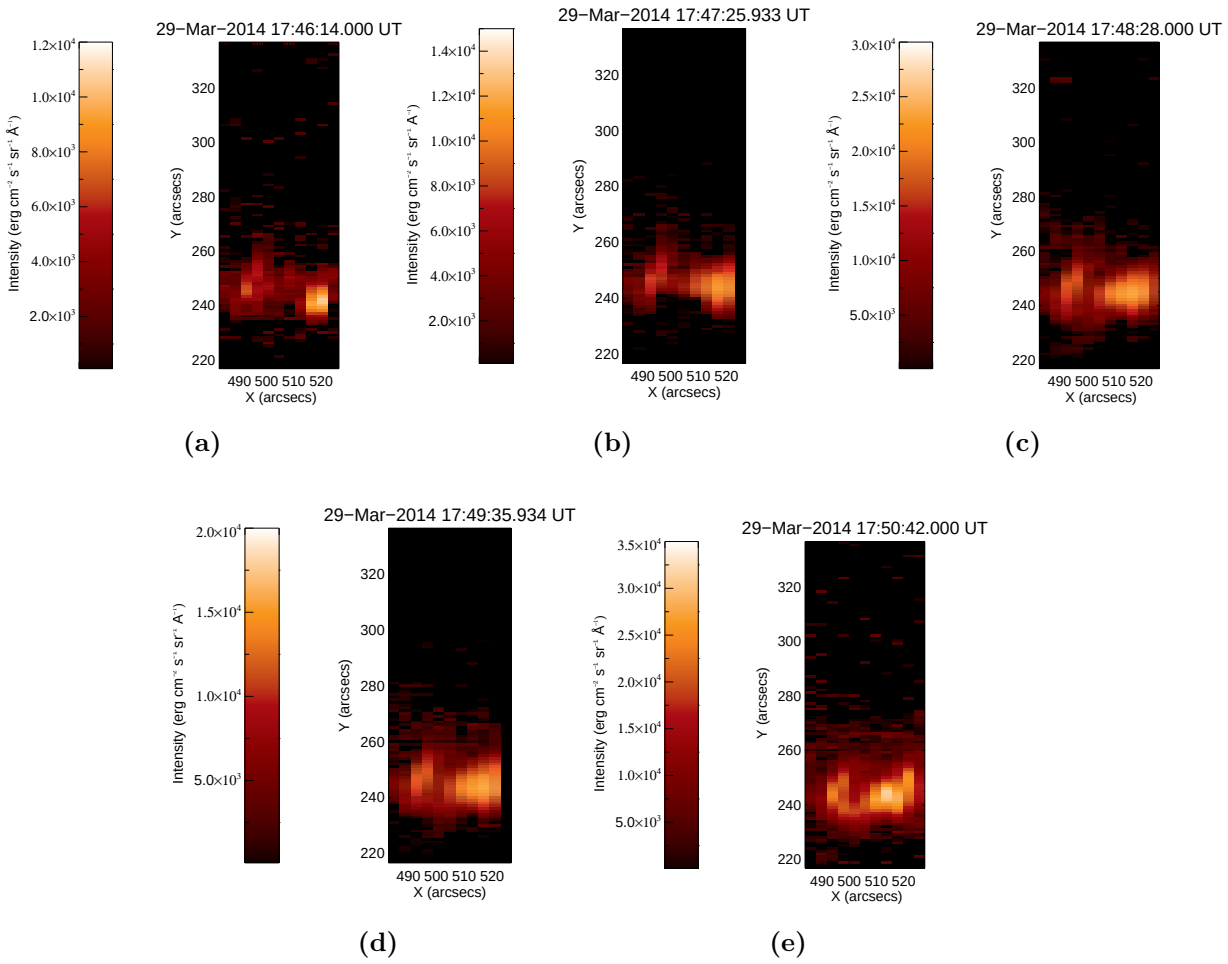

Figure 4.8: Intensity Maps (a) - (e) show the changing intensity of Fe XVII 269.42Å at the observed active region during the SOL2014-03-29T17:48 event, as seen by EIS with respect to time. Maps (b) and (d) are synthetic intensity maps produced by the method discussed in Section 4.2, all other maps are from real EIS data.

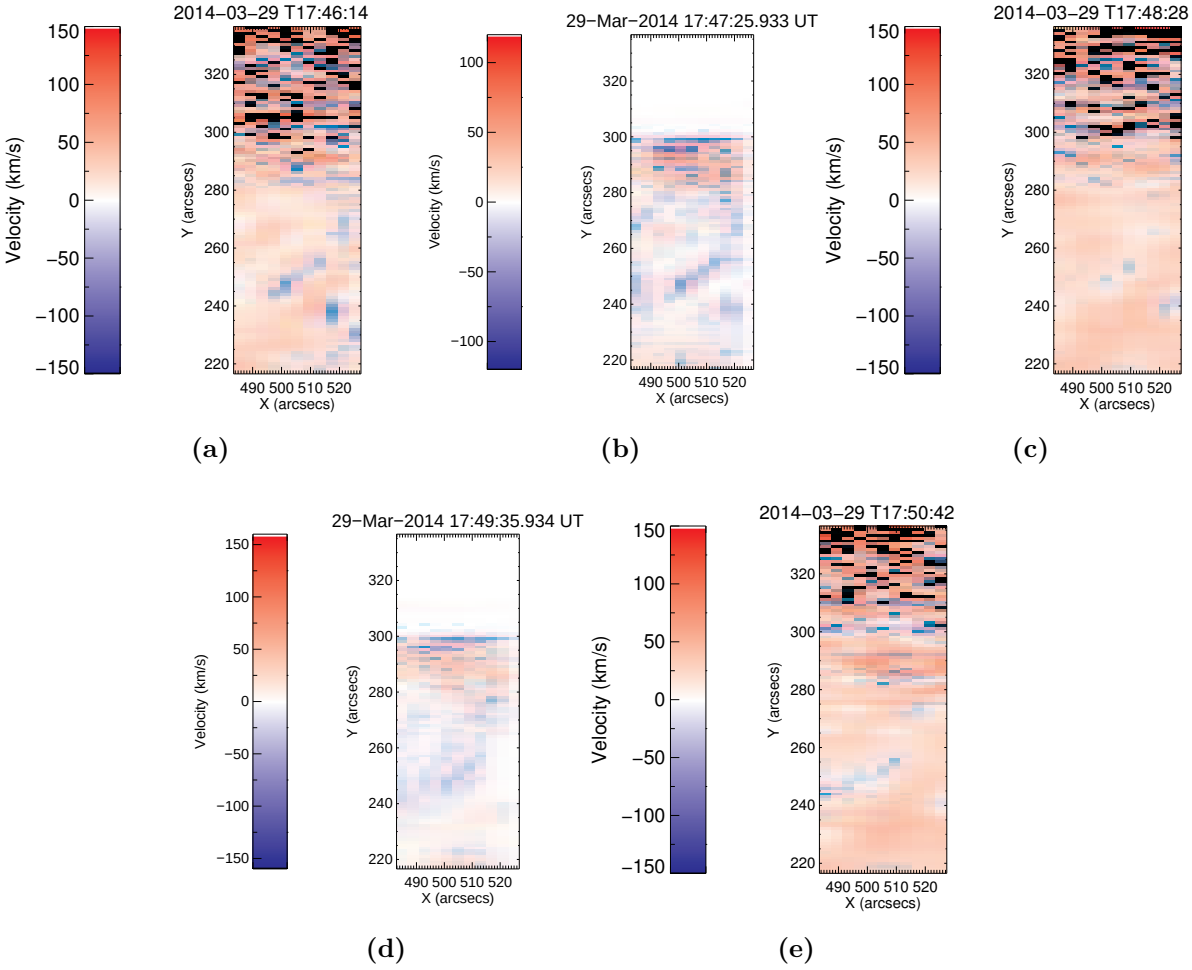

Figure 4.9: Velocity Maps (a) - (e) show the changing intensity of Fe XXIII 263.76Å at the observed active region during the SOL2014-03-29T17:48 event, as seen by EIS with respect to time. Maps (b) and (d) are synthetic Doppler velocity maps produced by the method discussed in Section 4.2, all other maps are from real EIS data.

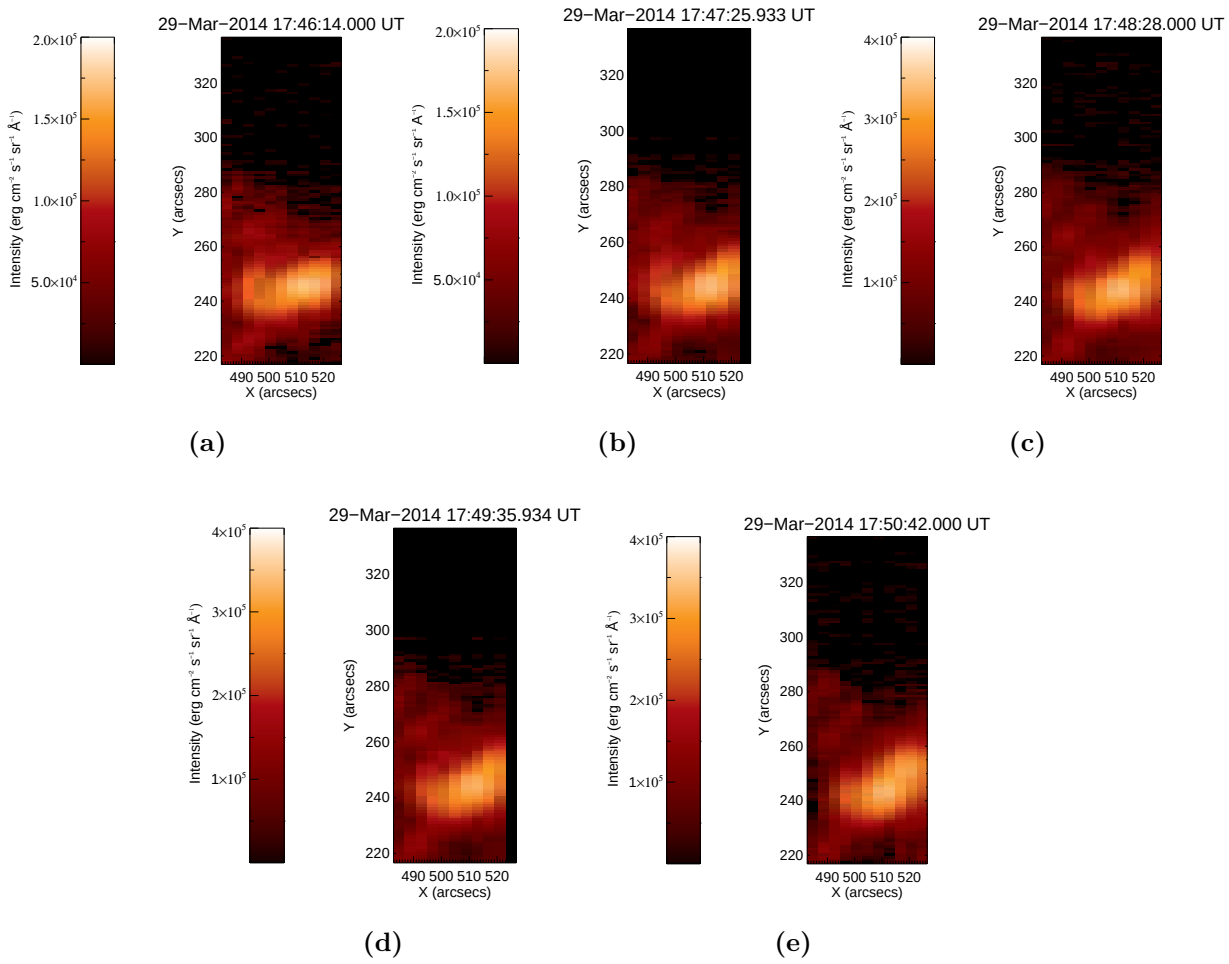

Figure 4.10: Intensity Maps (a) - (e) show the changing intensity of Fe XXIII 263.76Å at the observed active region during the SOL2014-03-29T17:48 event, as seen by EIS with respect to time. Maps (b) and (d) are synthetic intensity maps produced by the method discussed in Section 4.2, all other maps are from real EIS data.

4.3 Intensity-Weighted Average

Synthetic maps are produced at 10 second intervals at times that match exactly to the EVE measurements. In order to compare the EIS and EVE velocities, the synthetic EIS velocity maps must be averaged to give one value for every ten seconds. To do this an intensity-weighted average velocity was introduced since the brighter sources will dominate the velocity signal seen by EIS. Equation 4.1 was the formula used to achieve this result.

$$< v >= \frac{\sum_{i=0}^{n} I_i v_i}{\sum_{i=0}^{n} I_i} \tag{4.1}$$

Where I_i and v_i are the intensity and velocity, respectively, at specific pixel locations and $< v >$ is the calculated average velocity. Now that velocities have been calculated for every ten seconds during the flare for EIS, these values can be compared directly to EVE measurements. Plots of Doppler velocity against time can be created showing the measurements from EIS and EVE simultaneously. This allows a direct comparison of the data to be made and similarities or differences in trends to be noticed clearly. All of the comparisons made can be seen in Section 4.4 where they are discussed in great detail.

4.4 Results

Many EVE and EIS lines were investigated throughout the course of the project, however, few proved to be suitable for a comparison. There are many reasons why this is the case, along with the challenges of the instruments themselves. Firstly, many of the cooler temperature lines, such as Fe XII, were measured successfully with EIS but not with EVE. As mentioned previously EVE measures the Sun-as-a-star and so, Fe XII is a cooler line emitted across the whole disk causing difficulties when pinpointing flares. He II was measured very cleanly by EVE but contained a very strong and complex blend in EIS, thus making it unusable. Despite these setbacks data for three lines was

successfully obtained making comparisons for both flares possible.

4.4.1 SOL2014-03-29T17:48

4.4.1.1 Fe XXIII

Fe XXIII presented some difficulties during the process and methods described above. From the intensity maps shown in Section 2.4.2.3 one can see Fe XXIII emission is very limited in the first two rasters. This is because early in the flare during the times of 17:41:46 and 17:44:00 there is little to no emission of Fe XXIII as it is a high temperature flaring line. In the third EIS raster at 17:46:14, Fe XXIII emission can clearly be seen as this is during the impulsive phase of the flare. From this point onwards, Fe XXIII emission appears in all subsequent rasters following the typical pattern of blueshifts you would expect during a flare. The lack of Fe XXIII emission in the first two rasters caused serious large fluctuations in the intensity-weighted velocity. Due to large errors in fitting what were essentially background fluctuations in the Fe XXIII window. Consequently, these rasters were removed for the process of calculating polynomial fits and hence intensity-weighted velocities. Consequently, this would mean no useful EIS data is present until 17:46:14. However, this was done to achieve a more stable polynomial interpolation in the other rasters, and a better comparison to the corresponding EVE velocities.

In addition to removing two rasters, a blue wing component in the Fe XXIII line profile was also noticed. This blue wing component appears very strongly in the third EIS raster at a time of 17:46:14, during the impulsive phase of the flare. It is subsequently noticed in all other rasters but only slightly as the 17:48:28 raster shows the GOES peak of the flare. During the GOES peak and the gradual phase the line profile resembles more of a single Gaussian with the blue wing being weakly present. This would mean a triple Gaussian would have to be fitted to the EIS wavelength window, one to the neighbouring Fe XVI line and two to the Fe XXIII line itself. This phenomenon has been noticed before in a C - class flare which occurred on the 14th December 2007. Milligan and Dennis also used EIS to measure Doppler velocities of

15 emission lines during the flare. They noticed a dominant stationary component and blue-wing component in the two hottest lines, Fe XXIII λ263.76 and Fe XXIV λ192.03 (Milligan & Dennis, 2009). Fitting a double Gaussian to the Fe XXIII line produces two components of velocity. These correspond to a fast-moving blueshifted component and a stationary component. As both of these components originate from one single ion and emission line it is necessary to represent both in the intensity weighted average velocity. This was done using the formula in Equation 4.2 modified from the original Equation 4.1.

$$< v >= \frac{\sum_{i=0}^{n} I_i^m v_i^m}{\sum_{i=0}^{n} I_i^m} + \frac{\sum_{i=0}^{n} I_i^s v_i^s}{\sum_{i=0}^{n} I_i^s} \tag{4.2}$$

where I_i is the intensity, v_i is the velocity and m and s represent the blue-shifted and stationary components respectively. The output of this is an array of velocities calculated at 10 second intervals according to EVE measurement times. These can then be directly compared to the EVE velocities calculated in Section 3.5 and shown in Figure 3.5. The result is a plot of both EVE and EIS velocities showing the similarities and differences in their trends.

Only data from 17:46:14 onwards was available for EIS as the previous two rasters showed none of this emission line in the active region. However, despite this a relatively comprehensive comparison can still be made. From Figure 4.11 it is clear both instruments Doppler velocity measurements agree during the gradual phase of the flare. They both exhibit the same slight blueshift towards the end of the gradual phase, signifying the presence of the Fe XX line. Between 17:46 and 17:48 both sets of velocities are also in agreement with each other. The EIS velocities do not possess a trend as steep as the EVE points, however, they are similar to each other and we must recall that the EVE value is affected by the presence of the Fe XX line which becomes stronger in the late phase. Another feature to notice is that the EIS trend also lies within the error bars calculated on the EVE velocities. It is unfortunate the Fe XXIII emission is not present in the first rasters as it would have been beneficial to have a complete picture.

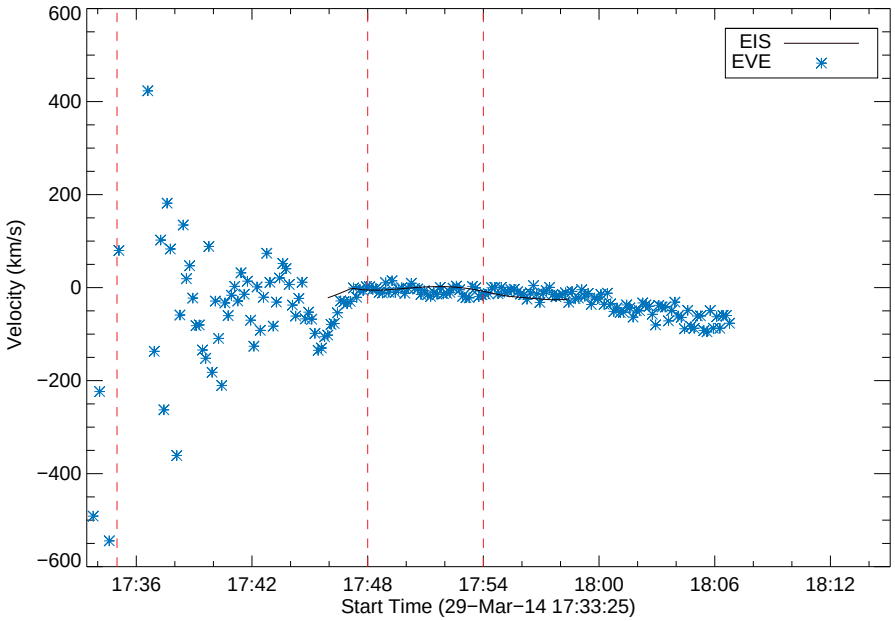

Figure 4.11: This plot shows the velocity values of both EIS and EVE data with respect to time and how they compare. The blue points are the EVE data, the black line is the EIS "synthetic flare" data and the dashed red vertical lines represent the GOES start, peak and end times of the flare.

4.4.2 SOL2011-02-16T07:35

4.4.2.1 Fe XII

Fe XII is a cooler line with a temperature of around 1.2 million K. As it is a cooler line it is emitted across the whole of the Sun's disk making it difficult for EVE to notice differences in it's emission during a flare. However, as EIS only views a small section of the flaring region the structure of it can be seen in Fe XII. When looking at EIS intensity maps in Section 2.4.1.2 of Fe XII coronal loops can easily be seen along with the movement of plasma. Due to this the majority of the EIS raster was used when extracting the high intensity pixels through the use of poly_val. The same procedure, described in Section 4.2.1, of fitting polynomials to every pixels velocity values as they change with respect to time was still used. The calculation of the intensity weighted average velocity was also used as described in Section 4.3. The result is a plot of

changing velocity with respect to the EVE measurement times at 10 second intervals. Figure 4.12 shows what this looks like for Fe XII emission during the SOL2011-02-16T07:35 event.

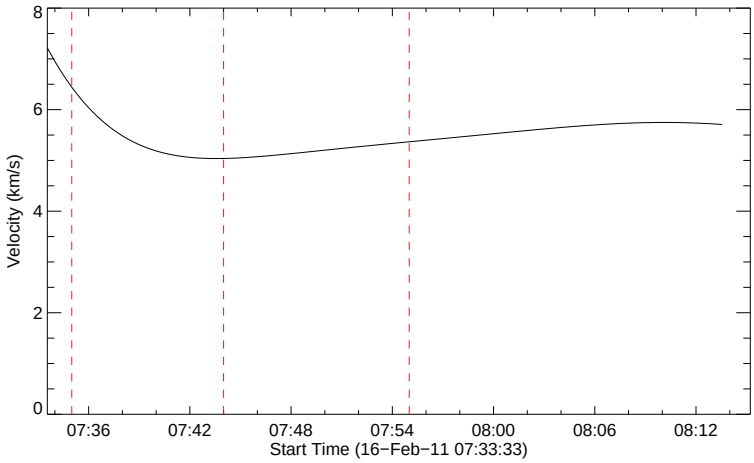

Figure 4.12: This plot shows the velocity values of EIS data with respect to time as calculated using the process described in Section 4.3. The dashed red vertical lines represent the GOES times of the flare.

Unfortunately, there was no suitable line in the EVE spectra at a similar temperature to compare to the Fe XII data gathered from the 2011-02-16T07:35 event. This is mainly due to the nature of the EVE instrument considering it takes whole disk measurements of all wavelengths. As a result, this makes it difficult to measure a significant increase in irradiance of cooler temperature lines. Despite this the light curve of Fe XII can be used to make an approximate comparison of the EIS velocities gathered.

The comparison of Fe XXIII in Figure 4.11 shows that both EIS and EVE are in agreement and exhibit the same trend during the gradual phase. It is then a statement can be made regarding the Doppler velocity values obtained with EIS in Fe XII. These Doppler velocities, in Figure 4.12, show fluctuations in the range of a few kilometers per second in accordance with dimmings noticed in the Fe XII lightcurve (Figure 4.13). It is also clear from Figure 4.12 that velocities are in the range of 4-8km/s which is extremely small when compared to the velocity of -135km/s measured in EVE. This

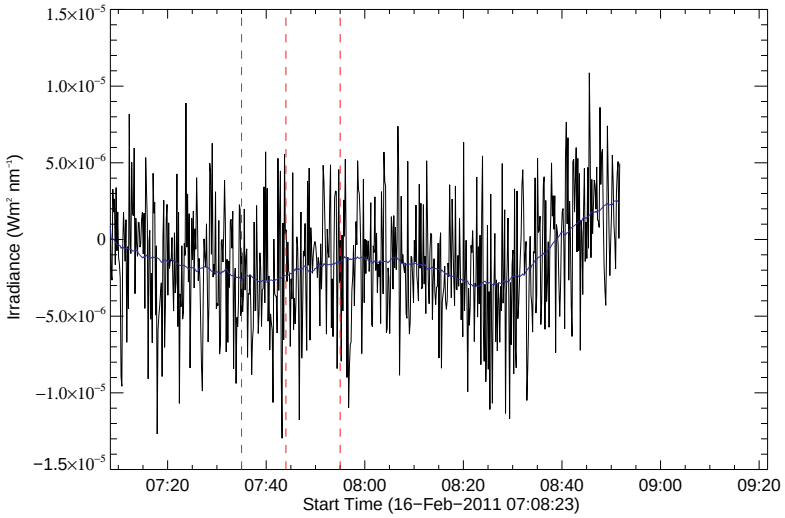

Figure 4.13: This is the EVE lightcurve showing the changing irradiance with repect to time of Fe XII during the SOL2011-02-16T07:35 event. The dashed red vertical lines represent the GOES start, peak and end times of the flare and the blue line is the smoothed irradiance to make the fluctuations clearer.

would then explain why EVE did not measure and Doppler shift in Fe XII as any changes in wavelength would have been small and and difficult to discern from the EVE spectra. That being said, if an instrument was to be designed for measuring Doppler velocities in Fe XII it would have to have a large precision both temporal and spatial and be able to distinguish velocities of a few kilometers per second.

4.5 Conclusion

In this chapter synthetic velocity and intensity maps were produced of EIS data corresponding to EVE observation times. The polynomial fits used to achieve this were successful as a means to calculate the synthetic maps. These maps were then converted into single velocity values for each EVE time producing a plot of velocity against time for EIS data. This lead to a comparison of Fe XXIII Doppler velocities in EIS and EVE data for the SOL2014-03-29T17:48 to be made successfully. The result was an agree-

ment between the instruments showing similar trends in velocity in the gradual phase. A second comparison was made of Fe XII Doppler velocities in EIS for SOL2011-02-16T07:35 to the lightcurve of Fe XII in EVE. Despite not having EVE velocities for this line a competent comparison was still made using the data available. The results of these comparisons show that it is possible to compare Doppler velocities from two extremely different instruments. The significance of this is the ability to use both the maps obtained by EIS and the Doppler velocities from EVE to determine the plasma flows during the flare at the active region. This has great implications as it shows both EIS and EVE are producing data which is in agreement with each other in terms of the Doppler velocities. It also opens doors for more of this type of work to be carried out with the possibility of including other instruments in the comparison.

Chapter 5

Conclusions

5.1 Outcomes

In this thesis both EIS and EVE data have been analysed, calculating Doppler velocities for several emission lines of varying temperatures in two arcade flares. The initial aim was to make comparisons for EIS and EVE Doppler velocity calculations aiding in the understanding of plasma flows in flares.

In Chapters 2 and 3 details of data analysis methods used on both EIS and EVE were given. The chapters gave detailed descriptions of emission lines investigated and explained how Doppler velocities were calculated, presenting results obtained. These chapters provided the framework required to enable comparisons of the Doppler velocities to be made.

Chapter 4 then details the methods used to compare data from both instruments and presents results obtained in accordance with the initial aim. The Fe XXIII emission line produced a very nice comparison of Doppler velocities in the SOL2014-03-29T17:48 event. The trends of both were extremely close to each other; especially during the gradual phase were they were very similar. It was unfortunate that EIS data earlier than 17:46 could not be used in the velocity analysis resulting in a comparison during the impulsive phase only. However, very little strong Fe XXIII emission was present in these rasters, providing Doppler

EVE velocities could not be calculated using Fe XII because of the nature of the observations made by the EVE instrument. EVE measures the Sun as a star, which causes Fe XII emission during the flare to be 'washed out' in background emission from the entire disk of the Sun. This then makes it difficult to pinpoint the flaring emission and so Gaussians cannot be fitted to calculate the Doppler shift in wavelength. However, a statement was made using the synthetic interpolated velocities obtained from Fe XII in the SOL2011-02-16T07:35 event. The statement was that if a spectrometer was to be designed for measuring Doppler velocities in Fe XII it would have to have a large precision both temporal and spatial and be able to distinguish velocities of a few kilometers per second. This statement arose for several reasons; (i) the interpolated velocities had values of between 4-8km/s which was very small when compared to the EVE Fe XXIII velocities in the range of 135-150km/s and (ii) The comparison made in Fe XXIII during the gradual phase of the flare provided confidence in the methods used and result obtained.

The successful comparison between EIS and EVE in Fe XXIII has shown it is possible to take data from two very different instruments and use them to obtain similar Doppler velocity results. The advantage gained through the comparison is the knowledge gathered from both sets of data combining to produce a fuller picture of plasma flows during flares. In order to gain a comparison the EIS data was used in a complicated interpolation process where polynomial fits were used to extrapolate the known data covering a wider time domain. Although this seems complicated it was an essential process in the analysis as it set up the EIS data to mimic the measurement technique used by EVE making the comparison possible. It is for this reason I would recommend this technique to anyone else carrying out this type of work. However, I would suggest great consideration be taken into how it may be improved such as the possibility of having a larger array of EIS measurements or even which emission lines would be best for a comparison. It is from this research that a conclusion has been made on how different instruments observe and measure the same event. For example, the large blueshift seen in Fe XXIII in EVE data is not picked up as strongly in EIS. However, the comparison of Fe XXIII Doppler velocities shows that the instruments do

agree with each other in terms of the gradual phase of the flare. The principles of this method could be applied to other instruments which also viewed these events giving a greater insight into the plasma flows of flares.

5.2 Problems Encountered

The first issue in carrying out this analysis was finding flares which had been observed by EIS and which also had a strong enough signal in EVE to allow good velocity measurements. Due to EIS being a slit-rastering image spectrometer it only observes small areas of the Sun's disk and is not always looking in the right location. However, through the reading of literature and consulting the flare lists on the EVE and EIS websites this was swiftly resolved and two flares were found; SOL2011-02-16T07:35 and SOL2014-03-29T17:48.

A second and more complicated problem was identifying low temperature emission lines for analysis. At first He II was selected which provided good Doppler velocity measurements in EVE but the problem lay with EIS data. The He II line in EIS was extremely badly blended and required a lot of time to extract and de-blend individual lines. It was then decided to abandon the He II line due to time constraints on the project, however, EVE results were still presented. The next line used was O VI which was present in the 2011 flare and provided nice EIS rasters with good Doppler velocity measurements. However, this time the problems lay with EVE data with either; (i) the line profiles being too noisy or (ii) MEGS-B data not being present for the flare. This then left Fe XII to investigate which yet again provided its own problems. As mentioned earlier Fe XII is emitted across the whole disk of the Sun providing problems in EVE data. Due to this, no Fe XII lines or other similar temperature lines such as Fe XIII could be used due to noisy line profiles providing problems isolating the correct line for Gaussian fit. This problem was not overcome, however, a comparison of Fe XII was still made using the EVE lightcurve and EIS Doppler velocities. Despite all problems encountered the aim of the project was still met and a very successful comparison in Fe XXIII was made.

5.3 Future Work and Improvements

Potential improvements to this project include the investigation of more flares to see if they also have a correlation in EIS and EVE data, especially in Fe XXIII. We have presented synthetic interpolated velocity values and would have liked to calculate error estimates on these. This could be done using a Monte Carlo approach; where velocity values would have been varied at each time, refer to Figure 4.2, and multiple polynomial fits applied to calculate errors on the coefficients. This would therefore, provide errors on interpolated velocity values using further calculations.

Another improvement includes the de-blending of the He II line which would be useful as a comparison to the EVE data at cool temperatures. It also would have been of great benefit to look at other hot lines such as Fe XXIV to see if they exhibit the same behaviour as Fe XXIII. In turn, investigating other lines and flares would also be a great benefit, however, restrictions would have been based on measurements obtained by EIS. Future work in this project could involve the use of density diagnostics on lines giving more information on plasma flows. Another possibility involves the synthetic velocity maps approach, using this on other EIS lines could give an idea of what the velocities would be in other lines which might at some point be observed in Sun-like stars.

Bibliography

Aschwanden, M. J. 2015, The Astrophysical Journal Letters, 804, L20

Asplund, M., Grevesse, N., Sauval, A. J., & Scott, P. 2009, Annual Review of Astronomy and Astrophysics, 47, 481

Bray, R. J., Loughhead, R. E., & Durrant, C. J. 1984, The solar granulation, Vol. 270 (Cambridge University Press Cambridge)

Brosius, J. W. & Holman, G. D. 2007, The Astrophysical Journal Letters, 659, L73

Carrington, R. C. 1859, Monthly Notices of the Royal Astronomical Society, 20, 13

Carroll, B. W. & Ostlie, D. A. 2006, An introduction to modern astrophysics and cosmology, Vol. 1

Cox, A. N., Livingston, W. C., & Matthews, M. S. 1991, Solar interior and atmosphere (University of Arizona Press)

Crotser, D., Woods, T., Eparvier, F., Triplett, M., & Woodraska, D. 2007, in Proc. SPIE, Vol. 6689, 66890M

Culhane, J., Harra, L., James, A., et al. 2007, Solar Physics, 243, 19

Czaykowska, A., De Pontieu, B., Alexander, D., & Rank, G. 1999, The Astrophysical Journal Letters, 521, L75

Del Zanna, G. & Woods, T. 2013, Astronomy & Astrophysics, 555, A59

Fletcher, L., Dennis, B. R., Hudson, H. S., et al. 2011, Space science reviews, 159, 19

Hall, L. 1971, Solar Physics, 21, 167

Hall, L. & Hinteregger, H. 1969, in Solar Flares and Space Research, Vol. 1, 81

Hall, L. & Hinteregger, H. 1970, Journal of Geophysical Research, 75, 6959

Haugan, S. 1999, Solar Physics, 185, 275

Hudson, H., Woods, T., Chamberlin, P., et al. 2011, Solar Physics, 273, 69

Hudson, H. S. 2016, private communication

Janvier, M., Savcheva, A., Pariat, E., et al. 2016, Astronomy & Astrophysics, 591, A141

Kane, S. 1983, Recent advances in the understanding of solar flares: proceedings of the U.S.-Japan seminar held at Komaba, Tokyo, 5-8 October 1982, Solar physics (D. Reidel)

Korendyke, C. M., Brown, C. M., Thomas, R. J., et al. 2006, Applied optics, 45, 8674

Kosugi, T., Matsuzaki, K., Sakao, T., et al. 2007, Solar Physics, 243, 3

Landi, E., Del Zanna, G., Young, P., Dere, K., & Mason, H. 2011, The Astrophysical Journal, 744, 99

Leighton, R. B., Noyes, R. W., & Simon, G. W. 1962, The Astrophysical Journal, 135, 474

Li, Y., Ding, M., Qiu, J., & Cheng, J. 2015, The Astrophysical Journal, 811, 7

Longcope, D. 2014, The Astrophysical Journal, 795, 10

Mason, J. P., Woods, T. N., Caspi, A., Thompson, B. J., & Hock, R. A. 2014, The Astrophysical Journal, 789, 61

Milligan, R. O. 2015, Solar Physics, 290, 3399

Milligan, R. O. 2016, in IAU Symposium, Vol. 320, Solar and Stellar Flares and their Effects in Planets, 41–50

Milligan, R. O. & Dennis, B. R. 2009, The Astrophysical Journal, 699, 968

Müller, D., Marsden, R. G., Cyr, O. S., Gilbert, H. R., et al. 2013, Solar Physics, 285, 25

Neupert, W. M. 1968, The Astrophysical Journal, 153, L59

Pesnell, W. D., Thompson, B. J., & Chamberlin, P. C. 2012, Solar Physics, 275, 3

Phillips, K. J. 1995, Guide to the Sun (Cambridge University Press)

Piddington, J. 1983, Astrophysics and Space Science, 90, 217

Richardson, J. D. 2010, in Heliophysical Processes (Springer), 83–98

Roy, A. E. & Clarke, D. 1982, Bristol: A. Hilger, 1982. 2nd ed., 1

Simoes, P. J. 2015, private communication

Turck-Chièze, S., Schmutz, W., Thuillier, G., et al. 2006, in SOHO-17. 10 Years of SOHO and Beyond, Vol. 617, 165

UK, G. 2015, National Risk Register for Civil Emergencies

Woods, T., Eparvier, F., Hock, R., et al. 2012, Solar Physics, 275, 115

Young, P. 2010, EIS Software Note No. 1

Young, P., O'Dwyer, B., & Mason, H. 2011, The Astrophysical Journal, 744, 14

Young, P. R., Tian, H., & Jaeggli, S. 2015, The Astrophysical Journal, 799, 218

Young, P. R., Zanna, D. G., Mason, H. E., et al. 2007, Publications of the Astronomical Society of Japan, 59, S857